

CHARACTERIZATION OF GOLD BLACK AND ITS APPLICATION IN UN-
COOLED INFRARED DETECTORS

by

DEEP R. PANJWANI

M.Sc. M.S. University of Baroda, India, 2008

M.S. University of Central Florida, 2011

A dissertation submitted in partial fulfillment of the requirements
for the degree of Doctor of Philosophy
in the Department of Physics
in the College of Sciences
at the University of Central Florida
Orlando, Florida

Spring Term
2015

Major Professor: Robert E Peale

© 2015 Deep R. Panjwani

ABSTRACT

Gold black porous coatings were thermally evaporated in the chamber backfilled with inert gas pressure and their optical properties were studied in near-far-IR wavelengths. The porosities of coatings were found to be extremely high around ~ 99%. Different approaches of effective medium theories such as Maxwell-Garnett, Bruggeman, Landau-Lifshitz-Looyenga and Bergman Formalism were utilized to calculate refractive index (n) and extinction coefficient (k). The aging induced changes on electrical and optical properties were studied in regular laboratory conditions using transmission electron microscopy, Fourier transform infrared spectroscopy, and fore-probe electrical measurements. A significant decrease in electrical resistance in as deposited coating was found to be consistent with changes in the granular structure with aging at room temperature. Electrical relaxation model was applied to calculate structural relaxation time in the coatings prepared with different porosities. Interestingly, with aging, absorptance of the coatings improved, which is explained using conductivity form of Bergman Formulism.

Underlying aim of this work was to utilize gold blacks to improve sensitivity in un-cooled IR sensors consist of pixel arrays. To achieve this, fragile gold blacks were patterned on sub-mm length scale areas using both stenciling and conventional photolithography. Infrared spectral imaging with sub-micron spatial resolution revealed the spatial distribution of absorption across the gold black patterns produced with both the methods. Initial experiments on VO_x-Au bolometers showed that, gold black improved the responsivity by 42%. This work successfully establishes promising role of gold black coatings in commercial un-cooled infrared detectors.

I dedicate this work to my family and all of my friends in United States.

ACKNOWLEDGMENTS

First of all, I would like to convey my sincere thanks to my advisor Dr. Robert Peale for his efforts for my constant improvement. Even if I made mistakes in the beginning of my PhD, he never judged me harshly but continued to provide me with guidance and ample of time to let me learn to be an independent researcher. I will continue to follow work ethics and leadership qualities that I've learnt from him in my future efforts.

For pursuing PhD, it is also extremely important to have helpful colleagues. Fortunately, my lab mates were not only great colleagues but also great friends. Here, I would like to mention Janardan Nath, Mehmet Yesiltas, Evan Smith, Farnood Rezaie, Nima Nader, Imen Rezadad, Javanah Boroumand, Pedro Figueiredo and Monas Shahzad for being awesome lab pals. Especially all those critical discussions with Janardan have been a great source of new ideas for my research. Without his help, I could not have finished this work. I also miss the Geoffrey's coffee discussions with Monas. He actually made my belief even stronger that people in Pakistan are as welcoming and friendly as people in India. I am thankful to Mehmet. Without him it would have been extremely difficult to get reflectance spectra from gold black patterns. I really appreciate Evan for providing me with infrared detectors and characterize them with gold black. I am thankful to Siqi Sun, Chatdanai Lumdee, Binfeng Yun, and Dr. Pieter G. Kik for helping me to perform Dark Field Microscopy and Raman Spectroscopy experiments.

Chris Fredricksen, Guy Zummo, Doug Maukonen, Isaiah Oladeji and Tatiana Brusentsova provided me their constant source of support. I had a great time working under Chris. Tatiana invited us for awesome Russian food and it's not easy to beat those out of the world cocktails she made.

I must also mention Lin Yuqin and Yuheni Rudzewich. I will definitely miss the RIC (Russia India China) summit that we used to have almost every day during lunchtime. I consider myself to be extremely lucky to have met people like Swaran Nandini, Aniruddha Dutta, Shameek Bhattacharya, Ashish Khare, Siddhartha Banarjee, Rahul Higeste and Aditya Reddy. You have been my family here and never let me feel homesick even eight thousand miles away from my home. It is my sincere wish that our friendship is not forgotten in post-UCF era. Swaran, I am learning to take your critical views in more positive light. You have been such a great inspiration and kept me on my toes all the time.

Finally, I want to say that I cannot thank my family enough, especially my awesome parents. I would also use this opportunity to mention my two-year-old Nephew Krishna. With the passion he walks on musical keyboard and play ‘harmonious’ music, it makes me feel that he will be a rock star when he grows up. Of course if he chooses to be. On the lighter note, doing research is ‘almost’ similar as being a rock star, but the difference is that even though you produce value for the society, your victories are hardly public.

TABLE OF CONTENTS

LIST OF FIGURES	x
LIST OF TABLES	xiv
CHAPTER ONE: INTRODUCTION.....	1
CHAPTER TWO: OPTICAL PROPERTIES.....	8
2.1 Theoretical Considerations	8
2.1.1 Drude-Lorentz Model	9
2.1.2 Effective medium Theory	14
2.1.3 Maxwell Garnett approach.....	15
2.1.4 Bruggeman approach	17
2.1.5 Landau-Lifshitz-Looyenga (LLL) Formula.....	18
2.1.6 Bergman Formalism.....	19
2.1.7 Fresnel's Equations	22
2.2 Method for Gold Black Deposition.....	27
2.3 Methods for Characterization of Gold Black.....	29
2.3.1 Scanning Electron Microscopy (SEM)	29
2.3.2 Transmission Electron Microscopy (TEM)	30
2.3.3 Sheet Resistance Measurements	32
2.3.4 Fourier Transform Infrared Spectroscopy (FTIR)	33
2.4 Characterization Results	35
2.4.1 Formation of Porous Structure.....	35
2.4.2 Optical Properties.....	41
2.4.3 Discussion on Spectral Density Function	49
2.5 Conclusion	54
CHAPTER THREE: AGING STUDIES	56
3.1 Background.....	56

3.2 Isothermal Grain Growth Kinetics.....	57
3.3 Results.....	59
3.3.1 Structural Relaxation	59
3.3.2 Electrical Property	61
3.3.3 Optical Property.....	66
3.4 Discussion & Conclusion.....	68
3.5 Appendix: Polymer Infusion.....	70
CHAPTER FOUR: STENCIL LITHOGRAPHY OF GOLD BLACK.....	73
4.1 Background.....	73
4.2 Patterning with Stencil Shadow Mask	74
4.3 Sub-Micron Spatial Imaging.....	76
4.4 Results & Discussion	78
4.5 Conclusion	85
CHAPTER FIVE: PHOTOLITHOGRAPHY OF GOLD BLACK.....	87
5.1 Background.....	87
5.2 Patterning with Photolithography	88
5.3 Results & Discussion	90
5.4 Conclusion	103
CHAPTER SIX: DETECTOR WITH GOLD BLACK COATED PIXELS	105
6.1 Background.....	105
6.2 Design & Processing.....	108
6.3 Initial Results	110
6.4 Calculations & Discussion.....	111
6.5 Future Work	115
APPENDIX A: PUBLICATIONS.....	117
APPENDIX B: COPYRIGHT PERMISSION LETTER	119

REFERENCES 121

LIST OF FIGURES

Figure 1 Infrared transmission through Earth's atmosphere. Source: U.S. Navy, http://en.wikipedia.org/wiki/Infrared .	1
Figure 2 Transmission Electron Microscope image of gold black	5
Figure 3 Real (red) and imaginary (blue) part of permittivity of bulk gold calculated from Drude model	11
Figure 4 In Maxwell Garnett approach, medium consists of isolated particles embedded in dielectric host	15
Figure 5 Bruggeman theory is applied to nano/micro geometry of a composite system made of material A & B	17
Figure 6 Electro-magnetic vectors with light polarized with electric field parallel to the plane of the surface (s-polarized).	24
Figure 7 Electro-magnetic vectors with light polarized with electric field perpendicular to the plane of the surface (p-polarized).	25
Figure 8 Thermal evaporation chamber for deposition of gold black coatings	28
Figure 9 Joule breakdown region on gold black (left). The closer view of the breakdown region shows the existence of micron size pores (right).	33
Figure 10 Bright-field TEM image of isolated gold black feature (left). SAD pattern on isolated gold black feature.	36
Figure 11 HR-TEM image of an isolated gold black chain.	37
Figure 12 Cross-section SEM image of gold black coating on Si substrate	38
Figure 13 SEM top-view of gold black coatings prepared at N ₂ pressure of 0.3 (a) 1.5 (b) & 3.0 Torr (c). SEM cross-sectional view of respective coatings are shown in (d), (e) & (f).	39
Figure 14 (a) reflectance (b) transmittance (c) absorptance (1-R-T) spectra of coatings prepared with similar deposition parameters shown in Table 1. The absorptance is smoothed using Binomial algorithm.	42
Figure 15 An attempt to reproduce absorptance of gold black coatings using Maxwell-Garnett (top) and Bruggeman formulas (bottom). The volume fractions are shown in Table 1.	44
Figure 16 The experimental absorptance is fitted to Landau-Lifshitz-Looyenga (top) & Bergman Formalism (bottom) for calculation of effective permittivity. The fitting parameters are shown in Table 2. Solid lines: measured values, markers: calculated values.	46
Figure 17 Refractive index (n) and extinction coefficient (k) of all Types of coating calculated using LLL(left) and Bergman Formalism (right).	49

Figure 18 Bergman spectral densities of all the coatings from Table 1 are calculated using interpretation in [55].	50
Figure 19 Wavenumber dependence of permittivity constant (ϵ) for $\epsilon_m = 1$ and substituting bulk gold Drude model as ϵ_p .	52
Figure 20 Percolation strength of Bruggeman and LLL effective medium theories.	54
Figure 21 TEM image of gold black feature before (a,b) & after (c,d) aging of 90 days	61
Figure 22 Sheet resistance aging in ninety days at room temperature. Extended arrows and dot at the center suggest the scale of standard deviation and mean value respectively.	62
Figure 23 SEM Cross-section view of exact same spot before (a) and after (b) aging.	63
Figure 24 Sheet Resistance plotted against time at different temperatures for coating Type2 (a) & Type 3 (b) from Table 1. The dots are experimental data and lines are fitted with Eq (3.9)	64
Figure 25 SEM Cross-section view of exact same spot before (a,c,d) and after (b,d,f) aging at respective temperatures for two hours	65
Figure 26. Relaxation time is plotted against initial sheet resistance of porous gold coatings.	66
Figure 27. Reflectance spectra measured before (solid black) and after (dashed red) aging for 90 days of period. Calculated reflectance spectra (dots) at different conductivities using Eq. (3.9).	67
Figure 28 Reflectance spectra measured at two hours of interval at different elevated temperatures.	68
Figure 29 Gold black film cross section before (a) and after (b) 2 minutes of fuming. Similarly, (c) & (d) shows cross section before and after 20 minutes of fuming respectively.	71
Figure 30 Spectral aging in fumed samples for 90 days at room temperature.	72
Figure 31 Schematic diagram of stencil lithography method. Alignment of shadow mask (top) is followed by deposition of gold black (middle). Then the mask is lifted leaving the gold black pattern (bottom).	75
Figure 32 Signal comparison of global and synchrotron source. Image re-printed with permission from Mehmet Yesiltas' PhD Dissertation [100].	77
Figure 33. FTIR imaging with a multibeam synchrotron source. Reprinted with permission from Macmillan Publishers Ltd: Nature Communications [101].	78
Figure 34. Optical microscope images of gold black patterns produced with shadow mask. The mask-substrate separation was twice larger for the circular pattern.	79
Figure 35. SEM image of thin circular gold black patterns similar to shown in Figure 27 (b). The magnified image clearly show presence of edge effect.	80
Figure 36. SEM cross-section image of pattern produced with 0.3 mm of mask-substrate height.	80

Figure 37. SEM image of gold black produced (a) without and (b) with shadow mask at height of 0.3 mm.	81
Figure 38. (a) Optical microscope image of gold black pattern. (b) Color online. Spectrally-integrated IR reflectance microscope image of the same sample. Numbered dots indicate where spectra are sampled. The color scale indicates reflectance, which is integrated over the range 970 – 3700 cm ⁻¹ .	83
Figure 39. Reflectance spectra extracted from six different pixels numbered as in the infrared image Figure 38.	84
Figure 40. Infrared image of gold-black pattern at indicated wavelengths.	85
Figure 41 Schematic of processing sequence patterned gold black/SiO ₂ composites	89
Figure 42 SEM images of photo-lithographically produced goldblack patterns over-coated with 150 nm SiO ₂ on Si substrate.(a) Gratings with close to 20 micron width (b) Square lattice with sub-10 micron features.	91
Figure 43 SEM top-view images of gold black coating before (left) and after (right) SiO ₂ deposition.	92
Figure 44 Cross-sectional side view SEM images of gold black coating before (left) and after (right) SiO ₂ deposition.	92
Figure 45 Cross-sectional SEM images of unprotected gold black before (a) and after (b) wetting in Acetone. Oxide over-coated gold black before (c) and after (d) wetting in acetone.	93
Figure 46 SEM top-view image of oxide over-coated gold black coating after lift-off treatment in acetone solvent for 10 seconds.	94
Figure 47 Angle dependent scattering from similar coating shown in Figure 46	95
Figure 48 Absorptance spectra for gold black with 150 nm of SiO ₂ over-coating (left) vis-NIR (right) mid- to long-wave IR.	97
Figure 49 Calculated real (ϵ_1) and imaginary permittivity (ϵ_2) of SiO ₂ (a,b) & gold black (c,d) before and after collapsing of the structure respectively. SiO ₂ and gold black (ϵ_1 , ϵ_2) value are generated using Bruggeman and Bergman Formalism to fit the experimentally deposited gold black-SiO ₂ composite. Bulk layer of SiO ₂ is reproduced using dielectric function model proposed by W.Theiss in SCOUT Program.	98
Figure 50 Bergman spectral densities of gold black from Table 3 are calculated using interpretation in [55].	99
Figure 51 (left) Optical image of photo lithographically patterned gold black with 150 nm of SiO ₂ thick protection layer (dark) on gold substrate (bright). (Right) Integrated infrared reflectance of gold black pattern (900 to 3700 cm ⁻¹). The infrared image is a mosaic formed by stitching 4 × 3 hyper-spectral tiles	100
Figure 52 Reflectance spectra extracted from six different pixels shown in Figure 51 (right).	101

Figure 53. Reflectance line profile across a nominally 20 micron wide oxide-protected gold-black pattern showing decreased absorption at its edges. The dots represent the actual data points and the grey line is obtained from smoothing the data using Savitzky-Golay algorithm as a guide to the eye to calculate FWHM.	102
Figure 54 (a) optical image of gold black pattern and (b) Integrated infrared image (900-3700 cm^{-1}) of the region shown in the optical image. (c) Scanned reflectance profile and infrared mapping (inset) at 3,5,8 & 9.4 μm wavelengths	103
Figure 55 Cross-sectional design of gold black coated resistive bolometer pixel with optical resonant cavity. Re-drawn from information based on reference [106].	109
Figure 56 SEM (a) & optical (b) images of linear array of gold black coated bolometer pixels .	109
Figure 57 SEM image of gold black coated free standing pixels after ashing in plasma.	110
Figure 58 Calculated reflectance of the reference pixel (top) and gold black-SiO ₂ coated pixel (bottom).	113
Figure 59 Noise equivalent power of reference and gold black-coated devices plotted against the source temperature. Mean square power fluctuations are calculated using equation	114

LIST OF TABLES

Table 1 Volume fraction, nano-chain diameter and conductivity of coatings prepared with different N ₂ pressure inside the chamber.....	40
Table 2 Parameter d_{meas} is measured thickness, α is fitted loss factor in Eq (2.10) neglecting inter-band transition term, g_0 is fitted percolation strength in Bergman Formalism, (LLL) is the fitted volume fraction LLL formula to match the experimentally measured absorptance as shown in Figure 16 (top), and f (Bergman) is the volume fraction obtained experimentally (From Table 1).....	47
Table 3 Fitting parameters for calculating absorptance spectra of oxide over coated gold black in Figure 48. Here, d is the thickness, f is the volume fraction, g_0 is the percolation strength and α is the loss factor in Bergman Formalism.	98
Table 4 Measured output signal and noise of pixels with/without goldblack-SiO ₂	111
Table 5 Calculated output signal and noise in 3-5 μm and 8-14 μm wavelength range for reference and goldblack-SiO ₂ coated devices. Absorptance for reference devices: 13% in 3-5 μm and 27% 8-14 μm . Absorptance for gold-black devices: 92% in 3-5 μm and 74 % in 8-14 μm	115

CHAPTER ONE: INTRODUCTION

Infrared (IR) radiations known as ‘heat rays’ are part of electromagnetic spectrum from 0.75 to 1000 μm wavelengths. Sun is a broadband source of IR radiations, however Earth’s thick atmosphere contains rain, fog particles, aerosols which are large enough to block a large part of the spectrum but transmit 3-5 μm and 8-14 μm wavelengths. Both of these ranges fall in mid wave infrared (MWIR) and long wave infrared (LWIR) spectrum respectively. Figure 1 shows the absorption band of water, carbon dioxide, ozone and nitrous oxide molecules.

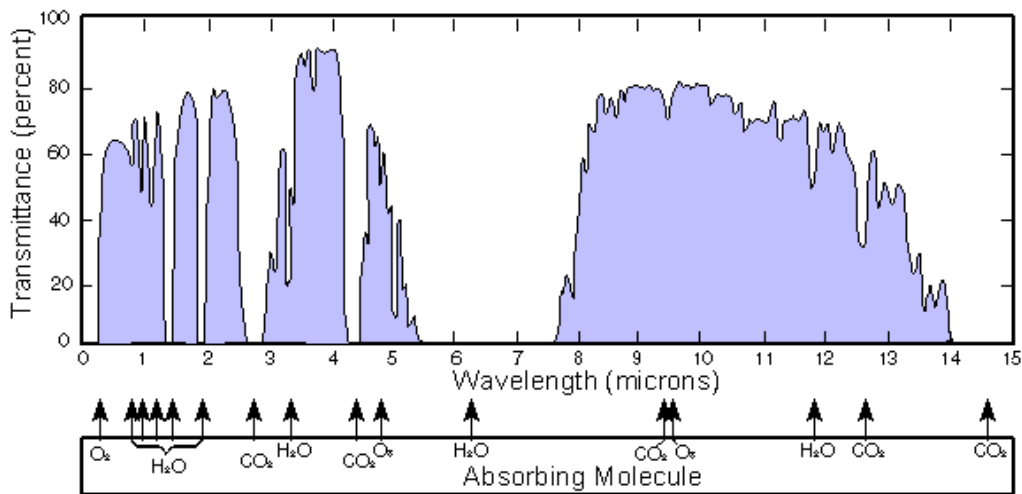


Figure 1 Infrared transmission through Earth’s atmosphere. Source: U.S. Navy, <http://en.wikipedia.org/wiki/Infrared>.

All the oscillating charged particles including atoms emit electromagnetic waves.

Vibrational frequencies of the atoms inside the object depend on the temperature of the body. According to Wien’s displacement law, a black body at 300 K has peak emission at 10- μm wavelength. Hence human (~ 310 K) and other mammals with body temperature close to that value show high emissivity in 8-12 μm wavelengths. On the other hand, objects with much higher temperatures such as hot engines and missiles show high

emissivity 3-5 μm wavelengths. Radiation received from any object is the total sum of emission, transmittance and reflectance. High contrast is achieved only if the reflectance of IR radiations from the background is much lower compared to emission from the object of interest. For e.g. reflected solar light has much higher intensity at 300 K in MWIR. On the other hand if the object is behind the dense fog, then scattering in MWIR can be an issue. Although the emitted power in LWIR is much lower, high contrast can be achieved since reflected sun rays from the background and scattering from the fog has minimum effect in this band of wavelengths.

IR detection is very old technique [1-4], but its applications were limited to military, security, academic purposes such as astronomy and meteorology for a long period of time. Although quantum detectors are highly efficient in mid-long wave IR range, they require cooling for suppression of intrinsic thermal noise, which made this type of detectors to be large, bulky, expensive and inconvenient to use (e.g. HgCdTe, InGaAs, InSb) [5]. This was one of the major obstacles in bringing the IR technology to regular consumer market. As photolithography became available in 1960's, the fabrication of thermopile, pyro-electric and resistive un-cooled focal plan array (FPA) technology [6-8] became possible and IR imaging penetrated in the area of applications such as firefighting, building inspection, automobiles, nondestructive testing, medical thermography and communications etc.

Un-cooled FPA in micro-bolometers consist of pixels with high density along with electronic line-filling scheme to generate high-resolution infrared image. Specifically speaking of resistive bolometers, each pixel consists of a membrane, made of high temperature coefficient of resistance (TCR) material such as vanadium oxide (VO_x) [9,

10] or amorphous silicon (a-Si) [11]. Membrane with high TCR material experiences the change in resistivity with detectable magnitude while exposed to even low incident power from the source. It is extremely important to retain maximum heat on the membrane, which requires high absorptance of IR radiation. Membrane alone with Fabry Perot cavity cannot absorb entire incident IR flux, for that purpose IR absorptive coatings are applied on top of the detector membrane. The heat captured by the coating should be efficiently transferred to the membrane, which converts the heat in to electric signal through Read Out Integrated Circuit (ROIC). Image is generated through the electric signal acquired from the FPA and image processing algorithms. For this purpose, many different absorber materials have been investigated, including thin metals [12, 13] and SiN_x films[14]. However, it is important to note that these IR absorbing bulk films suffer from high specific heat and their absorption is limited to a narrow range of wavelengths. High sensitivity and frame rate in resistive bolometer are achieved only if maximum deflection (voltage) in minimum time (mille-seconds) is produced. Specifically high frame rate cannot be achieved if specific heat of the absorptive coating is large. In order to minimize the specific heat, it is extremely important to reduce the thermal mass of the absorptive coating to the minimum and yet retain the maximum absorption. There are no bulk thin films in our knowledge that satisfy such conditions.

Pfund in 1930 found out that when bismuth is evaporated from a tungsten boat in high vacuum, the metal is deposited as a regular metallic layer, which was obvious result. However, if the pressure inside the chamber is raised to about 250 mTorr using an inert gas, the bismuth film becomes intensely black and fluffy. This film was quite opaque to visible light. Interestingly while testing the film for infrared measurements with rock-salt

spectrometer it was observed that the film did not exhibit any transmission or reflection. This film was highly absorbing in a broad range of 0.3 – 15 μm wavelengths, behaving very close to an ideal ‘black body’. Hence, the first ‘metal black’ was discovered [15]. Pfund suggested that, in the high vacuum evaporated bismuth particles aligned themselves to already present particles on the substrate to form a continuous lattice structure, resulting in very high electrical conductivity. When the inert gas pressure is introduced in the chamber during the evaporation, the particles cannot align in a regular lattice structure. They become loosely bound, and far less electrically conducting films.

In the further advancement very soon the metal blacks of other materials such as gold, copper, zinc, silver, lead, cadmium, nickel, antimony, tellurium and selenium were prepared with the similar method [16]. Gold black obviously generated more interest amongst the researcher due to its chemical inertness. It was shown that the morphology of gold black could be characterized by particle size and aggregation, which were controlled by evaporation rate, inert gas pressure and purity of inert gas [17].

Harris et al. in 1950’s investigated the gold black extensively [18-21]. Much of the efforts of Harris et al. were concentrated to relate optical properties with conductivity of the film. He showed that coatings produced with oxygen presence in the chamber showed degradation of absorptance after 3- μm wavelength. On the other hand, coatings produced with high purity of inert gas showed excellent absorptance up to 15- μm wavelengths. The drop in the absorptance was directly correlated with reduced conductivities due to formation of molybdenum or tungsten oxides around the gold nano particles during the evaporation.

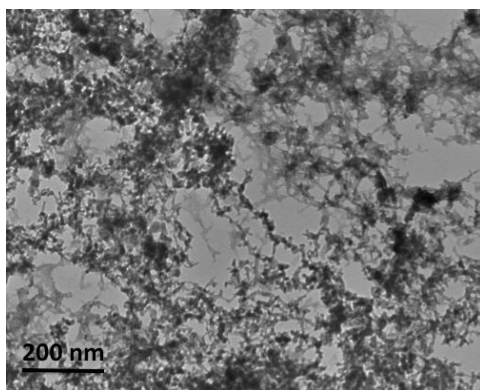


Figure 2 Transmission Electron Microscope image of gold black

Minimum amount of gold black mass ($\sim 5 \mu\text{g}$) was required to form conducting paths. The density of gold black was found to be $1/500$ compared to bulk gold, which suggested that fraction of gold was merely $\sim 0.2\%$. Interestingly gold black was still percolating and exhibited semi-metallic properties [18, 19]. Nevertheless Harris successfully explained that it is possible to explain reflectance and transmittance of the coating based on wavelength dependent conductivity. He also suggested that at resonant frequencies in visible-NIR spectrum, maximum conductivity is observed due to high optical absorptivity. However, beyond NIR, the conductivity is reduced drastically due to “condenser effect”, while in far-IR “relaxation effect” becomes more dominant resulting in increased conductivity. The relaxation times were found to be much lower at $500 \mu\text{m}$ compared to $100 \mu\text{m}$ wavelengths. Hence conductivity has an asymptotically increasing profile from mid-IR to far-IR wavelengths. Subsequently, absorptance of gold black reduced at higher wavelengths, possibly due to high reflectance from the interface [20, 21]. However, W. Becker et al. showed that increased conductivity not necessarily means reduced absorption. Using *spectral density independent* Bergman Formalism in the far IR, he proved that optimum value of conductivity is required for maximum absorptance at specific wavelengths [22, 23].

Chapter 2 explains the ‘blackness’ of gold black in infrared spectrum. The absorption in near to far-IR is explained by fitting the experimental results with different effective medium theories.

Chapter 3 includes the report on aging of these coatings in laboratory conditions. Harris et al. had briefly mentioned the issues regarding the fragility of these coatings [19]. Nonetheless in early 90’s Advena et al. suggested that in far-IR (at 50 μm), the reflectance is increased after aging at room temperature due to the partial collapse of the structure [24]. We present Transmission Electron Microscopy (TEM) results on sparse coatings for the interval of ninety days. For greater understanding, we monitored thickness, sheet resistance and reflectance before and after aging for ninety days in laboratory conditions. Accelerated aging process of coatings with different porosities is also studied by annealing the coatings for a few hours. Relaxation times of different types of coatings are also calculated. We also performed polymer infusion to explore if it could act as a dispersant and provide aging resistance to gold black. Study of aging is particularly important for the device carrying such fragile coatings for a long-term usage, specifically when large temperature fluctuations could be present.

In order to retain the heat from IR signal, resistivity-based bolometers include high temperature membranes have to be thermally isolated from the substrate through the cavity [25]. It is also extremely important to un-bridge the gap between the pixels for removal of thermal cross talks, otherwise membrane won’t be able to retain the heat, which can result in deterioration of the Signal to Noise Ratio and thermal time constant of the detector. *Chapter 4 & 5* include the results and discussion of sub-mm scale patterning of gold black. We present the technique to produce pattern with

photolithography and stencil lithography. A special technique of infrared spectral imaging with sub-micron spatial resolution is utilized to characterize the distribution of absorption across the patterns.

Chapter 6 includes the initial results on performance of the resistive bolometer after patterning gold black on the VO_x-Au membrane. The thermal time constant is calculated after adding a goldblack-SiO₂ composite coating on the membrane. Other parameters such as signal and noise are experimentally measured.

CHAPTER TWO: OPTICAL PROPERTIES

2.1 Theoretical Considerations

The constituents of gold black are air and gold. Gold is a noble metal with atomic number 79. It has Face Centered Cubic (FCC) structure with lattice constant 0.407 nm [26]. Gold is an excellent conductor of electricity and heat due to high free electron concentration of 5.9×10^{22} [26]. Free electrons with 42 nm of mean free path absorb incident energies and re-radiate, which makes bulk gold very shiny. Gold has been considered a precious metal throughout the human history because unlike other base metals, it is highly resistant to corrosion in atmosphere and it is also rarely available in Earth's crust.

Interestingly, when the physical size of the metal structure is equivalent or smaller than the mean free path of electrons, bulk behavior is no longer present, and whole new set of properties immerge. For example optically thick gold film looks 'yellowish' colored in visible spectrum, but when film is thin enough to be made of isolated nano particles, the color of the film appears to have several purple and red tones. This is due to localized surface plasmon resonances [27]. Different colors of nano particles are due to resonance at a particular wavelength depending on size, shape and dielectric environment [28]. On the resonant frequency scattering, absorption and near fields are enhanced by many folds, which have been utilized in improving photovoltaics [29, 30] and enhancing Raman signal for chemical sensing [31].

Gold black infrared absorbing film is also a product of nano particles adjoined together in a percolating network. Due to high porosity and sheer small size of particles, gold black turns out to be efficient light absorber. In order to understand the light trapping

mechanism in gold black, it is necessary to understand the optical properties of nano structures through effective medium theories.

2.1.1 Drude-Lorentz Model

When electron magnetic (EM) wave is incident on the metal, electrons are accelerated by external electric field caused by EM wave. The equation of motion of electrons under external field is given by;

$$e\vec{E}(t) = m\ddot{\vec{r}}(t) + m\tau^{-1}\dot{\vec{r}}(t) \quad (2.1)$$

Where, $\vec{E}(t)$ is external electric field, m is mass of the electron, \vec{r} is electron displacement and τ is the average time interval between the successive collisions in bulk metal. Here, we neglect the forces by magnetic field. The second term on right hand side is the damping factor. Assuming electric field $\vec{E}(t)$ and $\vec{r}(t)$ of oscillatory form, i. e.

$\vec{E}(t) = E(\omega)e^{-i\omega t}$ and $\vec{r}(t) = r(\omega)e^{-i\omega t}$, then Eq. (2.1) can be re-written as;

$$\vec{r}(\omega) = \frac{e\vec{E}(\omega)}{m(\omega^2 + i\omega\tau^{-1})} \quad (2.2)$$

Polarization P is correlated with susceptibility χ with following relation;

$$\vec{P}(\omega) = \epsilon_0\chi(\omega)\vec{E}(\omega) \quad (2.3)$$

Susceptibility is a measure of how much material is capable of being polarized. When material is placed in an external electric field, the electrons in the materials are displaced creating positive/negative dipoles. Electrons in more susceptible materials experience higher displacement in an external field.

Polarization is defined as dipole moment per specified volume, which is also dipole moment of one-charge times the number of charges (n) present in the specified volume.

$$\vec{P}(\omega) = -e\vec{r}(\omega) \cdot n \quad (2.4)$$

From Eq (2.2), (2.3) & (2.4) we can find the Drude susceptibility;

$$\chi(\omega) = -\frac{e^2 n}{m\epsilon_0(\omega^2 + i\omega\tau^{-1})} = -\frac{\omega_p^2}{(\omega^2 + i\omega\tau^{-1})} \quad (2.5)$$

$$\Rightarrow \omega_p = \sqrt{\frac{e^2 n}{m\epsilon_0}} \quad (2.6)$$

Here, ω_p is plasma frequency. Plasma frequency in metals represents the *collective* oscillation frequency of electrons within the material. Here, e & m are the charge and mass of the electron respectively. That said, plasma frequency of any material could be calculated for which the density of the electron (n) is known. At this frequency, both ϵ_r , $\epsilon_i \approx 0$, i.e., minimum damping is present at this frequency. The amplitude of the collective oscillation is maximum at this frequency. Below plasma frequency metals are highly reflective. However above plasma frequency metals are transparent. Relation between susceptibility and permittivity is $\epsilon(\omega) = 1 + \chi(\omega)$. Frequency dependent Drude permittivity is given by;

$$\epsilon(\omega) = 1 - \frac{\omega_p^2}{\omega^2 + i\Gamma\omega} \quad (2.7)$$

Equation (2.7) is Drude's model for calculating frequency dependent permittivity. Here, ω_p is plasma frequency and $\Gamma = 1/\tau$ is damping factor. Figure 3 shows the plot of wavelength dependent real and imaginary part of permittivity of bulk gold calculated from Eq (2.7). Imaginary of permittivity (ϵ_i) continues to be large positive value with, which signifies increased polarization with wavelengths.

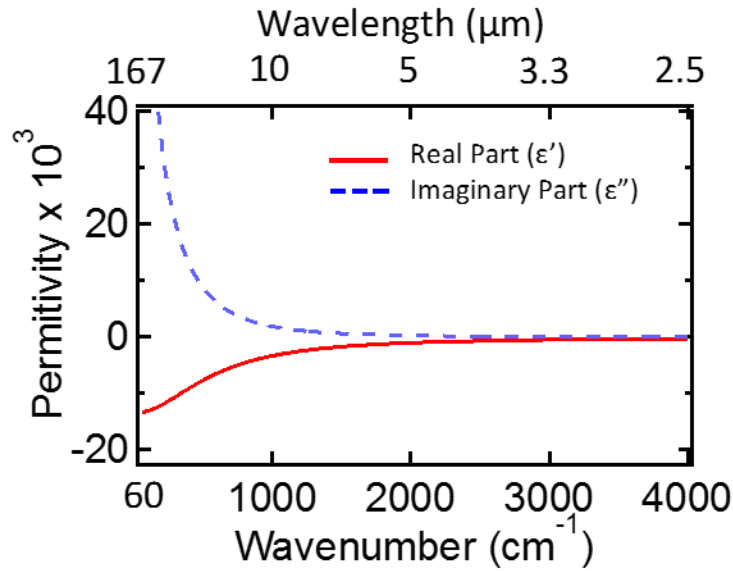


Figure 3 Real (red) and imaginary (blue) part of permittivity of bulk gold calculated from Drude model

There are a few assumptions and limitations to this model. 1) This model considers metal to be made of positively charged ions and sea of negatively charged free electrons, which are detached from positive ions. However, even ‘free electrons’ are attached to the far heavier nucleus with spring Force. Drude model completely neglects the spring force. In Lorentz model the spring force is included. 2) Similar to gas molecules in kinetic theory, electrons are considered to be moving in a straight line between the collisions, i.e. electron-electron interactions be completely ignored. The mean free path of electrons is considered as independent of position or velocity. 3) The relaxation times in Drude model are also considered to be frequency independent. 4) Importantly, Drude model does not take into the account of interband transitions.

Considering the simplicity of Drude Model, it still surprisingly predicts the bulk metal permittivity accurately above UV wavelengths. In order to predict permittivity in interband transition region (below ~ 500 nm wavelength), it requires certain

modifications. The modified Drude Model expressed here is known as Drude-Lorentz model;

$$\varepsilon = 1 - \frac{\omega_p^2}{\omega^2 + i\alpha\Gamma\omega} + \sum_i \frac{f_i\omega_i^2}{\omega_i^2 - \omega^2 - i\Gamma_L\omega} \quad (2.8)$$

The first term on right hand side represent the Drude term for free electrons. The second term, which is summation over Lorentz terms, represents the interband transitions. Here, f_i is oscillator strength, ω_i is transition frequency for conduction electrons and Γ_L is Lorentz damping term. Eq. (2.8) comprehensively predicts permittivity of bulk metal with interband transitions.

For particles with $d \leq$ mean free path, surface scattering of electron plays a major role in increasing the damping factor (i.e. reducing relaxation time). For e.g. in case of micron size gold particles, relaxation time (τ) can be considered same as bulk value (i.e. 9.3×10^{-15} s according to Johnson & Christy), but gold black consists of particle size 5-30 nm. Hence, the corrected value of relaxation time (τ) can be calculated from the following equation;

$$\Gamma = \frac{1}{\tau} = \frac{1}{\tau_b} + \frac{2v_f}{d} \quad (2.9)$$

Here d is the diameter of the particle, v_f is Fermi velocity (for gold $v_f = 1.4 \times 10^6$ ms⁻¹). Thus, according to Eq (2.9), damping factor in free electron model will be much larger due to surface scattering. On the other hand, grain boundary scattering and lattice defects such as twinning, stacking faults also play a significant role in increasing the damping further. For quantifying the damping factor of gold black in comparison with bulk gold, in Eq (2.8), we added a parameter α in Drude term, which we will call loss factor. Plugging the loss factor in Eq (2.8) will allow calculating the permittivity of nano-

crystalline gold particles with $d \leq$ mean free path, also including the interband transitions.

Approach in Eq (2.8) is valid for nanoparticles in general, however if the size shrinks to $\sim d \leq 5$ nm, quantum fluctuations have to be considered. For such particles only certain electronic transitions are allowed, i.e. energy levels in conduction bands are discretized. J.A. Scholl et al. showed that, by re-defining the Lorentzian term in Eq (2.8) quantum mechanically, particle permittivity could be expressed by [32];

$$\varepsilon = 1 - \frac{\omega_p^2}{\omega^2 + i\alpha\Gamma\omega} + \omega_p^2 \sum_i \sum_j \frac{f_{ij}^2}{\omega_{ij}^2 - \omega^2 - i\Gamma_L\omega} \quad (2.10)$$

The oscillator strength f_{ij} corresponds to oscillator strength in each state. Here, ω_{ij} is the transition frequency from occupied state (i) to unoccupied state (j) within the *spherical* Fermi space, which is expressed as;

$$\omega_{ij} = \frac{E_j - E_i}{\hbar} \quad (2.11)$$

$$\text{Where, } E = \frac{\hbar^2 \pi^2}{8mR^2} (2n + l + 2)^2 \quad (2.12)$$

Here n and l are principle and azimuthal quantum numbers respectively, m is effective mass of electron, R is the radius of spherical Fermi space. Standard quantum mechanical harmonic oscillator expresses the oscillator strength;

$$f_{ij} = \frac{2m\omega_{ij}}{\hbar N} |\langle i|z|i \rangle|^2 \quad (2.13)$$

Here, $\langle i|z|i \rangle$ is calculated by allowed wave functions of spherical well, N is the number of conducting electrons. Eq (2.10) provides a comprehensive approach for calculating permittivity of nano-crystalline particles in quantum size regime. It also predicts the

surprising results such as blue shift of bulk plasma frequency in extremely small nano particles. This is also experimentally confirmed on silver nano particles of size ~ 2 nm [32].

2.1.2 Effective medium Theory

Gold black coating constitutes of air (dielectric host medium) and gold (embedded particles in the host), hence permittivity in infrared can be described by effective medium approach, which treats the medium as homogenous and calculates the permittivity over entire volume. *This approach is valid only if the size of inhomogeneity is much smaller than wavelength of incident light, which allows us to neglect the scattering completely.*

Effective permittivity is calculated from non-trivial average of permittivities of individual components in the enclosed volume. In most cases permittivity of the dielectric host is known, which is a constant value usually. While for metals, permittivity is calculated from Drude's model (2.8) and plugged in to effective medium formulas. Depending on volume fraction of metal, medium will behave as dielectric, metallic or semi-metallic. Importantly, morphology of the medium decides which approach to be utilized, for e.g. whether metal particles are in percolating network or isolated. Topological details of nano/micro geometry also plays a significant role in influencing the permittivity of the medium.

Several approaches have been established, and the most prominent ones are from Maxwell Garnett for isolated particles [33], Bruggeman [34] and much less famous

Landau-Lifshitz-Looyenga [35, 36] for percolating networks. All of these simple approaches employ only volume fraction as the parameter to characterize the nano/micro geometry. Due to this gross simplification, many times false outcomes are produced. The most general form of effective medium permittivity is Bergman representation [37], which holds in any possible case. We have reviewed all four approaches to calculate permittivity of gold black coatings. It is important to note that connotation of permittivity of the particle and matrix element is different in for all the theories.

2.1.3 Maxwell Garnett approach

This approach is applicable to very diluted pool of small particles in the host medium, i.e. metal particles are considered far enough from one another that internal electric fields within the particles are unaffected by electric field interactions with neighboring particles. Only dipolar resonances are considered in this approach.

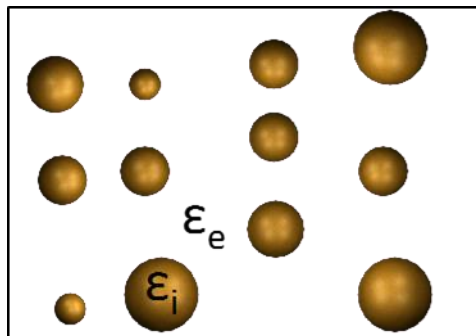


Figure 4 In Maxwell Garnett approach, medium consists of isolated particles embedded in dielectric host

Electric field and displacement are connected by permittivity,

$$\vec{D} = \varepsilon \vec{E} = \varepsilon_0 \vec{E} + \vec{P} \quad (2.14)$$

Similarly, average of displacement and electric field is connected through effective permittivity,

$$\langle \vec{D} \rangle = \varepsilon_{eff} \langle \vec{E} \rangle \quad (2.15)$$

Assumption: Average electric field over entire volume is summation of internal electric fields (E_i) within embedded nano particles with volume fraction f and total external field (E_e) in remaining fraction of host material.

$$\langle E \rangle = f E_i + (1 - f) E_e \quad (2.16)$$

From Equations (2.14), & (2.16), we can write the average displacement as;

$$\langle D \rangle = f \varepsilon_i E_i + (1 - f) \varepsilon_e E_e \quad (2.17)$$

We already know $\langle D \rangle = \varepsilon_{eff} \langle E \rangle$, therefore ratio of Eq (2.17) & (2.16) leads to;

$$\varepsilon_{eff} = \frac{f \varepsilon_i E_i + (1 - f) \varepsilon_e E_e}{f E_i + (1 - f) E_e} = \frac{f \varepsilon_i \frac{E_i}{E_e} + (1 - f) \varepsilon_e}{f \frac{E_i}{E_e} + (1 - f)} \quad (2.18)$$

Considering particles perfectly spherical, the field strength inside the particle calculated with quasi-static electrostatic gives following solution for internal field [38];

$$\left| \frac{E_i}{E_e} \right| = \frac{3 \varepsilon_e}{\varepsilon_i + 2 \varepsilon_e} \quad (2.19)$$

Substituting Eq (2.19) in (2.18) we get the following expression, known as Maxwell Garnett Formula.

$$\varepsilon_{eff} = \varepsilon_e + 3f\varepsilon_e \frac{\varepsilon_i - \varepsilon_e}{\varepsilon_i + 2\varepsilon_e - f(\varepsilon_i - \varepsilon_e)} \quad (2.20)$$

2.1.4 Bruggeman approach

Unlike Maxwell-Garnett, Bruggeman approach (frequently known as Effective Medium Approximation) is also valid for percolating networks. **Assumption:** *The permittivity near a particle it self is a composite property of the medium, i.e. host and particles are treated in equal manner.*

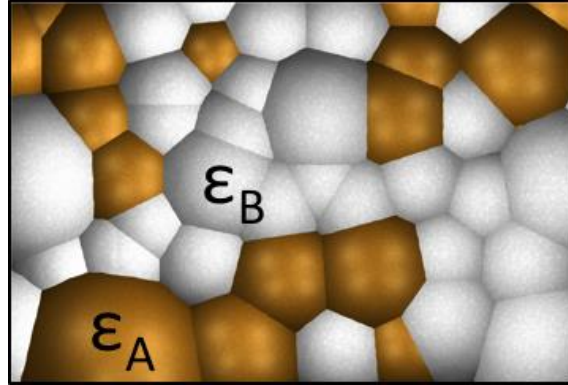


Figure 5 Bruggeman theory is applied to nano/micro geometry of a composite system made of material A & B

The particles consisting material A & B, who's known permittivities are utilized to calculate the effective permittivity of the composite medium. The average dielectric displacement is given by;

$$\langle D \rangle = f_A \varepsilon_A E_A + f_B \varepsilon_B E_B = \varepsilon_{eff} E_0 \quad (2.21)$$

$$\Rightarrow \varepsilon_{eff} = f_A \varepsilon_A \frac{E_A}{E_0} + f_B \varepsilon_B \frac{E_B}{E_0} \quad (2.22)$$

Here, $f_A = 1 - f_B$. Assuming the interconnected particles are spherical, we can write the expressions for internal electric fields [38].

$$\frac{E_A}{E_0} = \frac{3\varepsilon_{eff}}{\varepsilon_A + 2\varepsilon_{eff}} \quad \& \quad \frac{E_B}{E_0} = \frac{3\varepsilon_{eff}}{\varepsilon_B + 2\varepsilon_{eff}} \quad (2.23)$$

By substituting Eq (2.23) in (2.22), and working out some algebra we get following simplified expression, which is known as Bruggeman formula;

$$f_A \frac{\varepsilon_A - \varepsilon_{eff}}{\varepsilon_A + 2\varepsilon_{eff}} + f_B \frac{\varepsilon_B - \varepsilon_{eff}}{\varepsilon_B + 2\varepsilon_{eff}} = 0 \quad (2.24)$$

Where, f_A and f_B are volume fractions of constituents A & B respectively. Considering $f_A = f$, as volume fraction for particle, $f_B = 1 - f$ as volume fraction for host, and solving for quadratic equation, we get the following solutions;

$$\varepsilon_{eff} = \frac{1}{4} \left(2\varepsilon_B - 3f\varepsilon_B - \varepsilon_A + 3f\varepsilon_A \pm \sqrt{8\varepsilon_B\varepsilon_A + (2\varepsilon_B - 3f\varepsilon_B - \varepsilon_A + 3f\varepsilon_A)^2} \right) \quad (2.25)$$

With this formula we can control permittivity by changing volume fraction in a percolating network. Importantly, in the Eq (2.25), the spherical particles are considered to be embedded in a 3D medium. For circular particle embedded in 2D medium, the equation is slightly different, with geometrical factor considered as $\frac{1}{2}$ [39].

2.1.5 Landau-Lifshitz-Looyenga (LLL) Formula

Another example of a simple effective medium theory is from Looyenga [36], which is not as popular as the previous two theories, but performs much better for low volume fraction percolating networks. The final expression was also derived by Landau-Lifshitz in the book much earlier than Looyenga [35]. Therefore some authors also call it LLL formula.

Assumption: *In order to understand the approach, we consider two spheres. The larger sphere is made of material with permittivity $(\epsilon - \Delta\epsilon)$, and smaller sphere inside the larger sphere is made of porous effective medium with permittivity $(\epsilon + \Delta\epsilon)$. Importantly, the smaller sphere is not made of only material A or B, but mixture of it. Obviously, the size of the smaller sphere is considered large enough that particles embedded inside it are of negligible size compare to sphere. By continually adding minute amount of particles the effective permittivity of the medium increases. Volume fraction of particles inside the smaller sphere is correlated with total volume fraction (i.e. smaller and larger sphere) using Taylor's approximation. Nevertheless, Looyenga derives the formula for effective medium using approach discussed in the original manuscript [36];*

$$\epsilon^{1/3}_{eff} = f\epsilon^{1/3}_A + (1 - f)\epsilon^{1/3}_B \quad (2.26)$$

The assumptions make it obvious that this approach is applicable to dilute mediums, i.e. effective medium with low contrast compared to host medium. Interestingly, this formula is applicable to any shape of particles, since the assumptions to derive this formula do not take any resonances into the account. This is purely a averaging process.

2.1.6 Bergman Formalism

Unlike previous two theories, Bergman Formalism is more universal. It explains optical properties of any type of topology, whether percolating or isolated with much higher accuracy [37]. However, Bergman Formalism is also restricted by the size of the micron/nano structures compositing the effective medium, i.e. size should be small enough that medium is considered homogenous to longer wavelengths. The field displacement $D(r)$ inside the structure at position r is given by Maxwell's equation for the local field inside the structure $E(r)$ [38];

$$\vec{D}(\vec{r}) = \epsilon_0 \epsilon_p(\vec{r}) \vec{E}(\vec{r}) \quad (2.27)$$

This approach considers two phase system with sharp boundaries, i.e., permittivity of a nano/microstructure $\epsilon_p(\vec{r})$ at the boundary is equal to permittivity of the host medium ϵ_m .

Assumption: *With the field of view much larger than characteristic length scales of nano/micro structures, energy density within the structure and that of effective medium are considered equal.*

$$\frac{1}{2} \epsilon_0 \epsilon_{eff} \langle \vec{E} \rangle^2 = \frac{1}{2} \epsilon_0 \frac{1}{V} \int_V \epsilon_p(\vec{r}) \vec{E}(\vec{r}) \vec{E}(\vec{r}) d\vec{r} \quad \text{Where } \langle \vec{E} \rangle = \frac{1}{V} \int_V \vec{E}(\vec{r}) d\vec{r} \quad (2.28)$$

Bergman derived the expression of dielectric function of effective medium through Eq (2.27) & (2.28) as a function of sum of simple poles. For system with high number of multipolar resonances, Bergman Formalism is expressed in integral form as;

$$\epsilon_{eff} = \epsilon_m \left(1 - f \int_0^1 \frac{g(N, f)}{t - N} dN \right) \quad \text{Where, } t = \frac{\epsilon_m}{\epsilon_m - \epsilon_p} \quad (2.29)$$

ϵ_m is the host permittivity. ϵ_p is permittivity of embedded metal particles, which is calculated from Drude's model. $g(N, f)$ is spectral density function, it holds the information regarding topological resonances of the medium. This function is real and non-negative and it is normalized between the interval [0,1] for n. For isotropic medium there is a condition for zero-th and first moment the function satisfies following sum rules;

$$\int_0^1 g(N, f) dN = 1 \quad \text{And} \quad \int_0^1 N g(N, f) dN = \frac{1-f}{d} \quad (2.30)$$

Here, d is the system dimensionality. The left term in above equation suggests that average value of all the data points in $g(N, f)$ vs N plot remains unity and according to

right term area of the plot has to be equal to $1-f/d$. With *following the sum rules*, the shape of the spectral density $g(N,f)$ has to be adjusted in a way that calculated n and k value leads to the best match to the experimentally obtained reflectance and/or transmittance. The finalized spectral density shape, provides some information regarding the topology of the system. For e.g. in case of metal black structures if the coating becomes more conductive (or percolating) then a feature close to $N \approx 0$ appears in the plot of $g(N,f)$ vs N . Hence at $N = 0$, value of spectral density is actually percolation strength.

$$g(N, f) = g_0(f)\delta(N) + g_{con}(N, f) \quad (2.31)$$

Here, $g_0(f)$ is percolation strength, i.e. $g(N=0,f)$, $\delta(n)$ is Dirac delta function. In case of less percolating topology, the spectral density function is more weighted towards $N \approx 1$ (or between $N = 0$ and $N = 1$ in most cases). *The flexibility of spectral density function in Bergman Formalism, makes it much superior theory for calculating effective permittivities, however this also leads to inability of finding an analytical expression which could predict the spectral densities each time for different percolation strength and volume fraction[40].*

Permittivity calculated from this Equation is also correlated with the effective conductivity (σ_{eff}) of the porous coating, which is connected with the particle conductivity (σ_p) through volume fraction and percolation strength;

$$\sigma_{eff} = \sigma_p f g_0(f) \quad (2.32)$$

In fact this equation also tells us that with increasing the percolation strength $g_0(f)$, effective conductivity should increase.

2.1.7 Fresnel's Equations

Frequency dependent refractive index is simply square root of relative permittivity, this is a direct outcome from Maxwell's equations.

$$n + ik = \sqrt{\varepsilon} \quad (2.33)$$

$$\Rightarrow \varepsilon_1 + i\varepsilon_2 = (n + ik)^2 \quad (2.34)$$

$$\Rightarrow \varepsilon_1 = n^2 - k^2 \quad (2.35)$$

$$\Rightarrow \varepsilon_2 = 2nk \quad (2.36)$$

Here, ε_1 and ε_2 are real and imaginary parts of permittivity. Real part of refractive index (n) denotes the phase velocity and imaginary part (k) denotes the absorption losses of EM wave as it passes through the material with certain thickness. By solving Eq (2.35) & (2.36) for n & k , we get the following equations;

$$n = \sqrt{\frac{\sqrt{\varepsilon_1^2 + \varepsilon_2^2} + \varepsilon_1}{2}} \quad (2.37)$$

$$k = \sqrt{\frac{\sqrt{\varepsilon_1^2 + \varepsilon_2^2} - \varepsilon_1}{2}} \quad (2.38)$$

k is often called extinction coefficient. In most of the cases $k > 0$, i.e. light is absorbed in the medium. In case of many dielectrics k has a negligible value. Hence light passes through dielectrics without any attenuation (except absorption band at characteristic wavelengths). While in metals k has extremely large value in infrared, which results in low energy radiations penetrating inside the metal and very high reflectance at the

interface. Having $k < 0$, which corresponds to amplification of light, is only possible in fabricated medium such as laser cavity.

Once we have the permittivity of the medium, Fresnel's equations can be used to calculate reflectance and transmittance of the medium. In derivation of the Fresnel's equations for electromagnetic wave hitting the a plane surface at a particular angle, both parallel and normal components to the plane of incident (w.r.t normal to the surface) are calculated separately with different boundary conditions.

These conditions state that, tangential components (i.e. parallel to surface) of \vec{E} and \vec{B}/μ are continuous across the boundary. Here, electric and magnetic fields are perpendicular to each other. The vector $\vec{E} \times \vec{B}$ is along the direction of propagation denoted by \vec{k} . The electric and magnetic field amplitudes are related by $|\vec{E}| = v|\vec{B}|$, here $v = c/n$, which is speed of wave in the medium. As shown in Figure 6, when electric field is parallel to the surface (pointing out of plane of the paper), in that case magnetic field is perpendicular to the plane of surface.

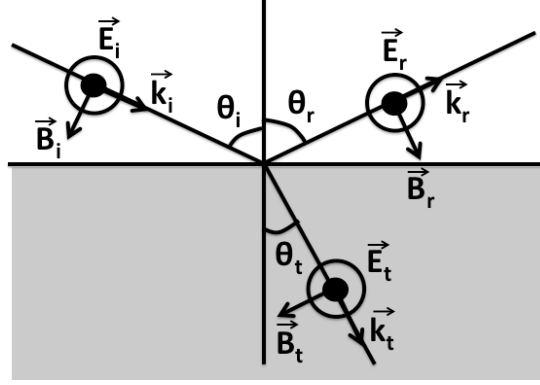


Figure 6 Electro-magnetic vectors with light polarized with electric field parallel to the plane of the surface (s-polarized).

Since electric field is completely tangential, by applying the boundary conditions we get the following expression;

$$\vec{E}_{oi} + \vec{E}_{or} = \vec{E}_{ot} \quad (2.39)$$

Similarly, for amplitude of magnetic field parallel to surface;

$$-\frac{B_{oi}}{\mu_i} \cos \theta_i + \frac{B_{or}}{\mu_r} \cos \theta_r = -\frac{B_{ot}}{\mu_t} \cos \theta_t \quad (2.40)$$

By substituting $E_0/v = B_0$ and $\theta_i = \theta_r$ (law of reflection);

$$\frac{n_i}{\mu_i} (E_{oi} - E_{or}) \cos \theta_i = \frac{n_t}{\mu_t} E_{ot} \cos \theta_t \quad (2.41)$$

By substituting Eq (2.39) in (2.41) to eliminate E_{ot} ;

$$r_{\parallel} = \left(\frac{E_{or}}{E_{oi}} \right)_{\parallel} = \frac{n_i \cos \theta_i - n_t \cos \theta_t}{n_i \cos \theta_i + n_t \cos \theta_t} \quad (2.42)$$

Similarly, by substituting Eq (2.39) in (2.41) to eliminate E_{or} , we get following equation;

$$t_{\parallel} = \left(\frac{E_{ot}}{E_{oi}} \right)_{\parallel} = \frac{2n_i \cos \theta_i}{n_i \cos \theta_i + n_t \cos \theta_t} \quad (2.43)$$

As shown in Figure 7, when electric field is perpendicular to the surface, magnetic field is parallel to the plane of surface.

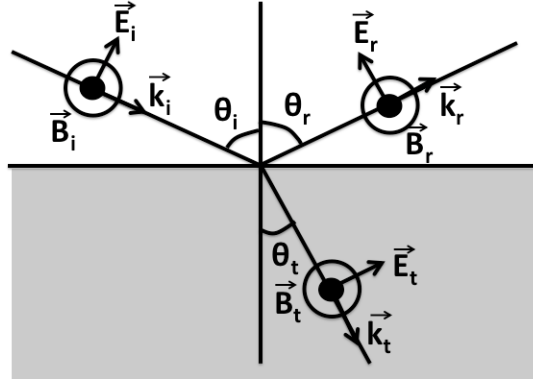


Figure 7 Electro-magnetic vectors with light polarized with electric field perpendicular to the plane of the surface (p-polarized).

Similarly, by applying boundary conditions we can calculate reflection and transmission coefficients of wave with electric field perpendicular to the plane of the surface given by the following equations;

$$r_{\perp} = \left(\frac{E_{or}}{E_{oi}} \right)_{\perp} = \frac{n_i \cos \theta_i - n_t \cos \theta_t}{n_i \cos \theta_i + n_t \cos \theta_t} \quad (2.44)$$

$$t_{\perp} = \left(\frac{E_{ot}}{E_{oi}} \right)_{\perp} = \frac{2n_i \cos \theta_i}{n_i \cos \theta_i + n_t \cos \theta_t} \quad (2.45)$$

In case of normal incidence $\theta_{i,t} = 0$. We can calculate reflectance $R = (E_{or}/E_{oi})^2$ and transmittance $T = (E_{ot}/E_{oi})^2$, which is given by following simple equations;

$$R = \left(\frac{n_i - n_t}{n_i + n_t} \right)^2 \quad (2.46)$$

$$T = \frac{4n_i^2 n_t^2}{(n_i + n_t)^2} \quad (2.47)$$

For two layer system, $i = 1$ and $t = 2$. Importantly, in case of bulk metal or metal porous media, refractive index has both real and imaginary parts, which need to be plugged in both Eq (2.46) & (2.47) to calculate absolute reflectance and transmittance. These equations are valid if the coating is suspended in the air, however in real world, coating is always deposited on a substrate such as bulk. We need to consider layer one (n_1) is air, for layer 2 (n_2+ik_2) is the coating deposited on the substrate (n_3).

For three layer structures, reflectance and transmittance is calculated similarly using Fresnel's equation including phase modulation (β) information [41].

$$R = \frac{r_{12}^2 + r_{23}^2 + 2r_{12}r_{23} \cos 2\beta}{1 + r_{12}^2 r_{23}^2 + 2r_{12}r_{23} \cos 2\beta} \quad (2.48)$$

$$T = \frac{t_{12}^2 t_{23}^2}{1 + r_{12}^2 r_{23}^2 + 2r_{12}r_{23} \cos 2\beta} \frac{n_3 \cos \theta_3}{n_1 \cos \theta_1} \quad (2.49)$$

$$\text{Here, } \beta = \frac{2\pi}{\lambda} n_2 d \cos \theta_2 \quad (2.50)$$

Here, r_{12} , r_{23} , t_{12} and t_{23} are analogues to Eq. (2.46) and (2.47), d is the thickness of the coating and incident angle is considered normal to the surface, hence $\theta_{1,2,3} = 0$.

In case of more than three layers of stacking, more comprehensive transfer matrix method is utilized. This method considers a matrix for translation and change in angle as rays

pass through each stack. Please refer through chapter 1.6.2 in reference [41] for detailed explanation on this method.

2.2 Method for Gold Black Deposition

Thermal evaporation is very common method for thin-film deposition. The material from the hot source evaporates and condenses on the relatively much cooler substrate.

Importantly, the entire process is performed under high vacuum. In the ‘complete’ absence of air molecules, the evaporated sub-nm size particles can travel with mean free path of even several meters. High quality of vacuum can result in extremely smooth and shiny film with sub-nm scale roughness. However, in case of gold black, chamber is back-filled with pure inert gas prior to evaporation of gold. This results in extremely low mean free path of gold particles during the evaporation, resulting in a completely different morphology and optical properties compared to bulk gold.

Figure 8 shows the thermal evaporation system, which consists of a chamber that is evacuated by a rotary backed diffusion pump. Once the pressure falls below 10^{-5} Torr, we back-filled the chamber with ultra-pure N_2 to a controlled pressure of ~ 300 - 3000 mTorr.

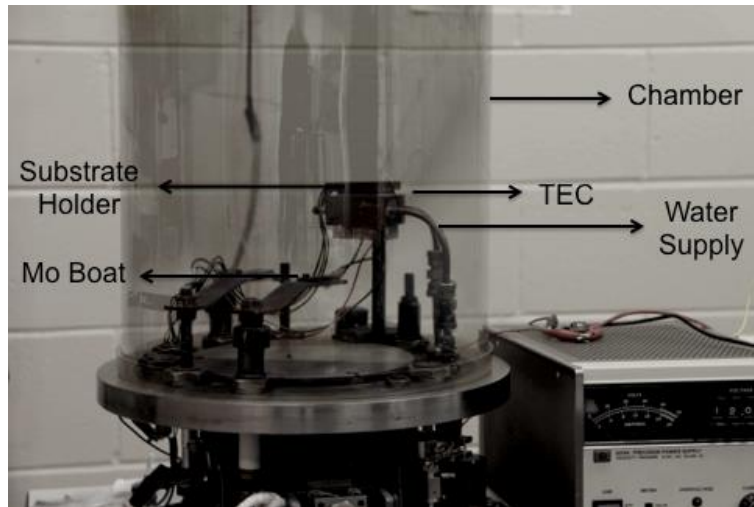


Figure 8 Thermal evaporation chamber for deposition of gold black coatings

Parameters that affect film morphology include deposition rate, N_2 pressure and mass of gold in the boat. A thermoelectric cooler (TEC) maintains the gold-coated substrate at $-13\text{ }^\circ\text{C}$. The cold side of the TEC, monitored with a thermocouple, is in direct contact with the substrate. The hot side of the TEC is attached to a water-cooled copper block using Apiezon N-type vacuum grease. Molybdenum evaporation boats with dimensions of $12\text{ mm} \times 5\text{ mm}$ and 1 mm depth were filled with $100\text{--}200\text{ mg}$ of 99.9% gold.

Substrate and Molybdenum boat are separated horizontally by 10 cm , and both face upward. The temperature in the boat is controlled by amount of current passing through the boat. When the melting temperature is reached, the gold wire takes the form of a sphere and after a few seconds it melts. The evaporation time is monitored from the time when gold melts into a liquid form to the total disappearance of gold from the boat. Evaporation rate is calculated by mass of the gold divided by total evaporation time.

2.3 Methods for Characterization of Gold Black

2.3.1 Scanning Electron Microscopy (SEM)

In SEM, electrons accelerated at several thousand volts hit the sample. Such electrons travel at a considerable fraction of speed of light, hence the de Broglie wavelength (\sim pm) is extremely small compared to the visible wavelengths. This enables us to examine the specimen with far greater resolution (\sim 1 nm).

When the electrons interact with the sample surface, back scattered, secondary electron, or auger electrons are released, which depends on the interaction region of the incident electrons. This interaction region depend on atomic density, topography of specimen and acceleration potential of primary electron beam. The primary electrons with low accelerating potential generally do not go through the specimen and bounce back from the top surface. They are known as back scattered electrons (BSE). This mode is useful to capture the topographical contrast depending on atomic density. For e.g. SiO₂ coating with density \sim 2.65 gm/cm³ will appear much darker compared gold thin film with \sim 19.3 gm/cm³ density in BSE mode. Secondary electrons (SE) are generated when the primary electron knocks out the specimen electron from outer orbit. Such secondary electrons have very low energy, generally a few electron volts. Only electrons close to the specimen surface are captured for detection. Although signal is much weaker in SE mode, shape of the topology is captured with much finer details. On the other hand, when the electrons with high accelerating voltage penetrate deep in to the specimen and knock electrons from inner orbits, which is known as auger electrons. In this case, not only electron but characteristic X-rays are also generated. In Electron Dispersive Spectroscopy

(EDS), these X-rays are utilized in quantifying the amount of specific elements in the specimen.

Scanning electron microscopy was performed using a Zeiss Ultra-55 SEM using in lens and Secondary electron detectors. In order to avoid damaging the coating due to energy transferred from electrons, accelerated voltage of electrons is limited to 5 kV. For determination of thicknesses, coatings were imaged edge-on. Samples were mounted at 90 degree using carbon tape. The uncertainty in this angle was less than 5 degree, so that the uncertainty in thickness measurements was less than 0.4%. To confirm the absence of Carbon and Oxygen from these coatings, EDS was performed at 15 kV accelerating voltage.

2.3.2 Transmission Electron Microscopy (TEM)

Unlike SEM, in transmission electron microscopy beam of electron is allowed to transmit through the thin specimen to form the image on fluorescent screen or CCD. The accelerating voltage of electrons is much higher (more than ~ 100 kV) compared to SEM. This results in even lower de Broglie wavelengths of electrons and much higher resolution, reaching sub-angstrom limit.

This technique is particularly useful for observing atomic arrangements, super lattices, atomic-scale defects, dislocations, stacking faults, grain boundaries etc. In bright field mode in HR- TEM imaging, the area of the sample is irradiated and a magnified image of crystalline structure, is formed by the electron optics below the sample. The fluorescent screen below the sample records the “shadow image” consisting with un-scattered

electrons. The different parts are displayed with different contrast depending on the density and thickness of the sample [42].

Inside TEM, diffraction pattern from selected area (SAD) can also be attained. Since the atomic spacing is sub-nm, as the specimen is exposed to high-energy electrons, atomic planes act as diffraction grating to the electrons. Diffraction patterns are utilized to identify the type of crystal structure, lattice planes and also lattice defects [43].

Importantly, these diffraction patterns are collected in reciprocal space. Diffraction patterns can also be simulated from HR bright field image by performing Fourier transform using image-processing software such as digital micrograph and ImageJ.

Extremely sparse porous gold black film was deposited on a plain Cu-50 TEM grid with diameter of 3.05 mm. The TEM grid is coated with thin amorphous carbon film with low relatively very electron density compared to gold. Hence, it acts as a uniform substrate for imaging. The gold black film was deposited on entire grid with 0.076 mg of gold from the Molybdenum boat in 3 seconds. This is extremely low mass of the gold. Therefore, in order to make sure that gold mass does not pop out of the molybdenum boat during the setting up the experiment, care was taken for avoiding the generation of any mechanical shock when placing the jar back on the stage. The N₂ pressure inside the chamber during evaporation was 300 mTorr. The granular structure was studied from HR-TEM micrographs (TECNAI F30) operating at 300kV and equipped with a tungsten field emission source.

2.3.3 Sheet Resistance Measurements

Sheet resistance is inherent characteristic of the thin film surface to oppose the current flow, which does not depend on the physical dimension of the material. In order to measure film sheet resistance, both two and four-probe methods are used. The total surface resistance between the two points on the thin film with the uniform thickness and infinitely large surface area is a sum of sheet resistance (R_s), contact resistance between probe and the surface (R_c) and parasitic resistance due to current flowing from probe in to the surface (R_{sp}). Although two-probe method can measure the sheet resistance, four-probe method is particularly superior because it uses the additional two outer probes to provide current and measure voltage from inner probes. This eliminates the possibilities of contact or parasitic resistance. Importantly, in sheet resistance, it is inferred that the current flows across the 2D plane parallel to the surface, not perpendicular to it [44]. Here, we assume that all four probes are separated equally.

Porosity and fragility of gold black coating did not allow utilizing the four-probe device for sheet resistance measurements. Hence, non-conducting substrates with evenly spaced four equally spaced gold ribbon electrodes were prepared photo-lithographically. The distance between the electrodes (s) was 500 μm , while the average thickness (t) of all gold-black coatings was less than 30 μm . In this particular case, since the surface area is not infinitely large, current tends to follow within the plane of electrode separation only. Hence, the sheet resistance is given by;

$$R_s = \frac{l}{s} \cdot \frac{V}{I} \quad (2.51)$$

Where, l is the length of the electrode. Importantly, we consider flow of the current across the plane of separation (s) of the electrodes. Porous gold showed constant sheet resistance for different driving current values from 0.3 to 2 mA.

No Joule heating related effects are observed at this lower driving currents. However, when the higher currents caused interesting changes in sheet resistance due to thermal breakdown and transformation of the film. As in Figure 9, *breakdown begins in a specific region and follows a 'zigzag' yet 'continuous' path*. The video recorded through optical microscope shows the breakdown path of $\sim 600 \mu\text{m}$, carved in four seconds [45]. The physical origin of Joule breakdown path must be the particular region experiencing the most resistive heating. Which then initiates the breakdown in adjacent undamaged gold black nano chains and follows a continuous path. The similar breakdown of densely packed Single Wall Carbon Nanotube is reported in literature [46].

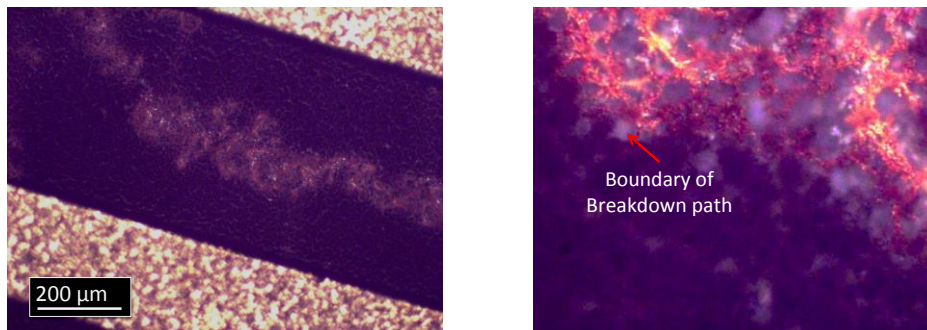


Figure 9 Joule breakdown region on gold black (left). The closer view of the breakdown region shows the existence of micron size pores (right).

2.3.4 Fourier Transform Infrared Spectroscopy (FTIR)

FTIR spectroscopy is utilized to how well a sample absorbs, reflects and transmits at each infrared wavelength. This technique is different from dispersive spectroscopy since it

does not exploit mono-chromator. The beam of light from black body radiator containing large range of frequencies is shined on the sample at once. Computing is utilized to calculate the raw data and extrapolate absorption at different wavelengths. Since the information is collected at all the wavelengths simultaneously, much higher signal to noise ratio is attained in comparison with dispersive spectroscopy. Much higher throughput is also attained since no entrance or exit slits for light dispersion are used. The most important accessory in FTIR is Michelson interferometer. In Michelson interferometer the collimated light from the infrared source is guided to the beam splitter, where ideally 50% of light refracted to a fixed mirror and other half is reflected to a movable mirror. The beam splitter is generally made of thin plastic sheet. Different plastic materials are used for range of wavelengths since a single material does not demonstrate transparency in entire infrared spectrum.

MW-IR, LW-IR and Far-IR absorptance measurements on gold black films were performed with BOMEM FT-IR, equipped with the broadband Globar source. For measurements in 2-15 μm wavelength range, MCT detector with KBr beam splitter was used. For 16-50 & 50-125 μm wavelength ranges DTGS detector was used with 3 & 25 micron Mylar film beam-splitter respectively. The coatings were deposited on double sided polished (DSP) silicon. The bulk gold surface and vacuum was chosen as reference for reflectance and transmittance respectively. The absorptance in such case was assumed to be $1 - \text{reflectance} - \text{transmittance}$.

Some of the coatings, especially for aging effect studies were deposited on a silicon substrate coated with 5 nm of chrome and 200 nm thick gold. The absorptance of the coating was assumed to be $1 - \text{reflectance}$, since the transmittance is null. 15 mm wide

aperture provides the average reflectance from the surface of the sample. The incident IR radiation angle was normal to the sample plane in all the cases.

The roughness of the gold black coatings (\sim nm) is much smaller than the wavelength of incident light (\sim μ m), hence scattering is null. In fact the coating appears completely black from all the direction in visible light, which confirms null or negligible scattering from these coatings.

2.4 Characterization Results

2.4.1 Formation of Porous Structure

A separate gold black feature is shown in Bright Field-TEM image in Figure 10 (left), which appears like a ‘nano-chain’ consisting of different particle sizes. This TEM image gives an insight on formation of this porous coating during the evaporation process. The particles during their passage from melted blob in the Molybdenum boat to the cooled substrate collide with the N_2 molecules present in the chamber. These collisions are inelastic since the N_2 molecules at much lower temperature absorb the partial energy from ‘hot’ gold particles. The gold particles with reduced energy also collide with one another and result in electronically bound particle structure. The atomic arrangement is similar to bulk gold. Selected Area Diffraction patterns at different spots shows perfect resemblance to a typical FCC structure. (1,1,1) And (2,0,0) are dominant planes, which is generally expected in FCC structures. An example is illustrated in Figure 10 (left).

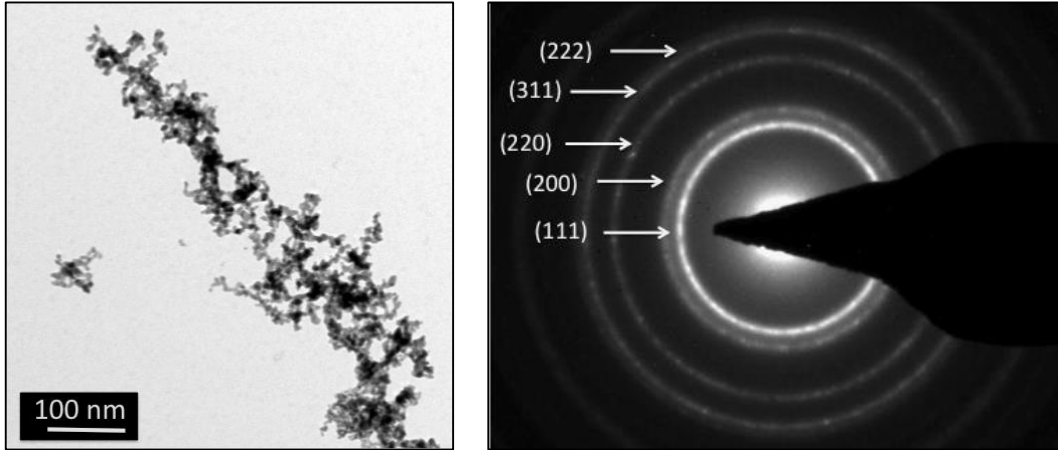


Figure 10 Bright-field TEM image of isolated gold black feature (left). SAD pattern on isolated gold black feature.

Figure 11 shows the isolated gold black chain with higher magnification. An individual chain itself is not a continuous crystallite entity but a split in to many grains with size ranging from 5-30 nm. The darker regions signify the shadowing from overlapping of multiple grains with different orientations.

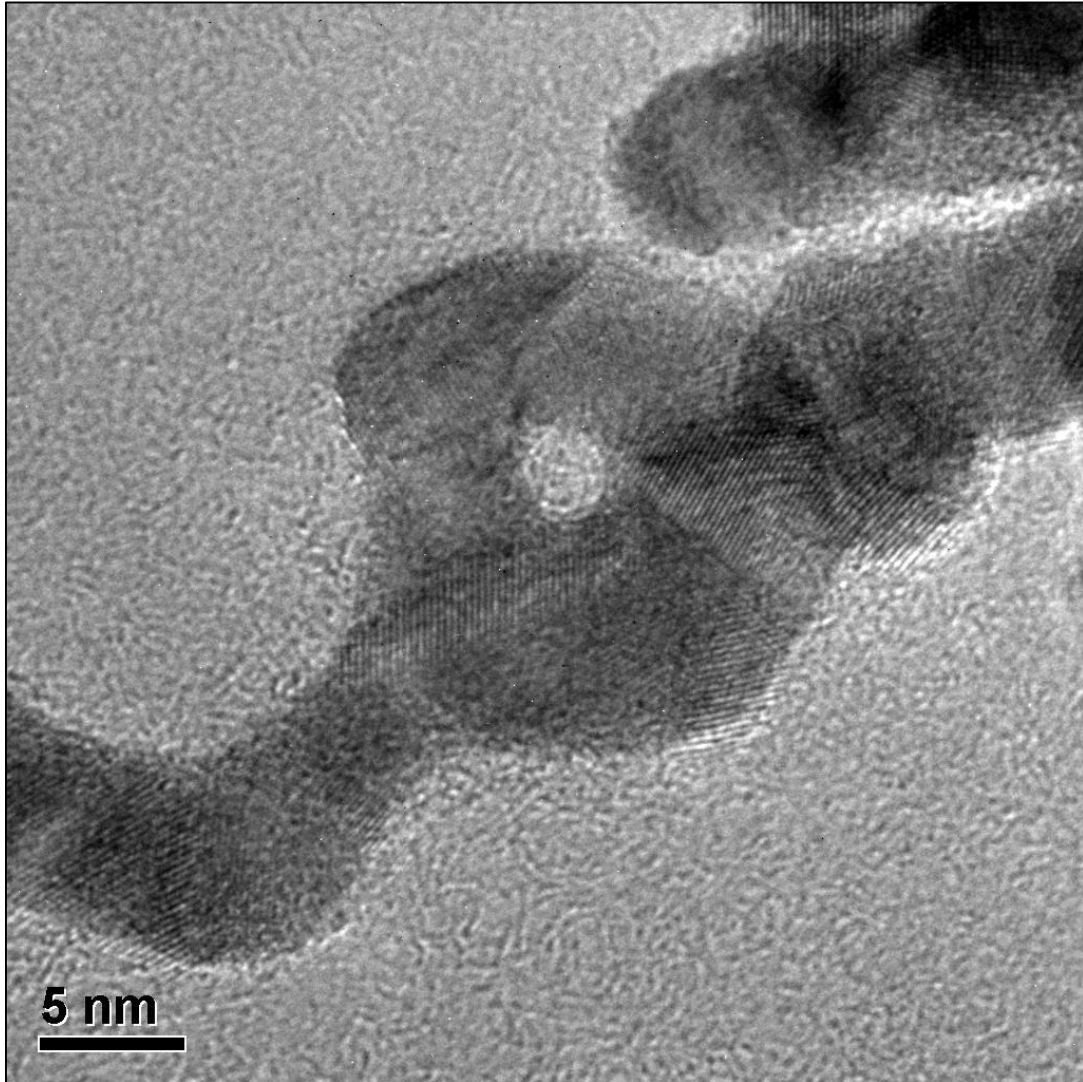


Figure 11 HR-TEM image of an isolated gold black chain.

There is a critical inert gas pressure necessary for percolation. Below the critical pressure, mean free path of gold particle is large enough that isolated nano particles are deposited on the substrate (not shown here). In our case ~ 200 mTorr was found to be the critical pressure for percolation. Importantly, critical pressure depends on evaporation conditions, especially on size of the chamber. Larger chamber will require higher pressure to form ‘chain like’ structure. The nano-chains produced in high-pressure inert gas environment diffuse towards the cooled substrate. These chains overlap on one another, join together very loosely, resulting in a ‘fluffy’ porous structure. Figure 12

shows the example of fluffy porous structure of gold black, which consist of nano chains like one shown in TEM image in Figure 11.

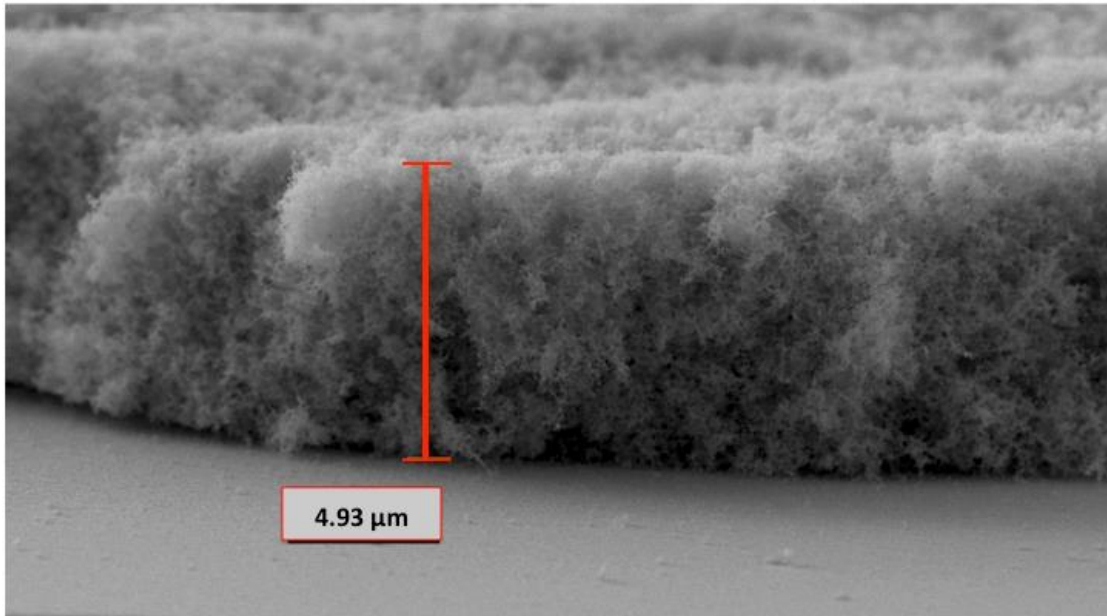


Figure 12 Cross-section SEM image of gold black coating on Si substrate

Figure 13 (a),(b) & (c) shows the top and (d),(e) & (f) shows the cross-section SEM view of the coatings prepared at 0.3, 1.5 & 3.0 Torr N₂ pressure respectively. From Figure 13 (c) & (f) it is evident that at 3 Torr pressure, morphology of the coating is less closely packed and thickness of the coating appeared 6 folds higher compare to coatings prepared at 0.3 Torr ((a) & (d)). This resulted in extremely high porosity, as shown in Table 1.

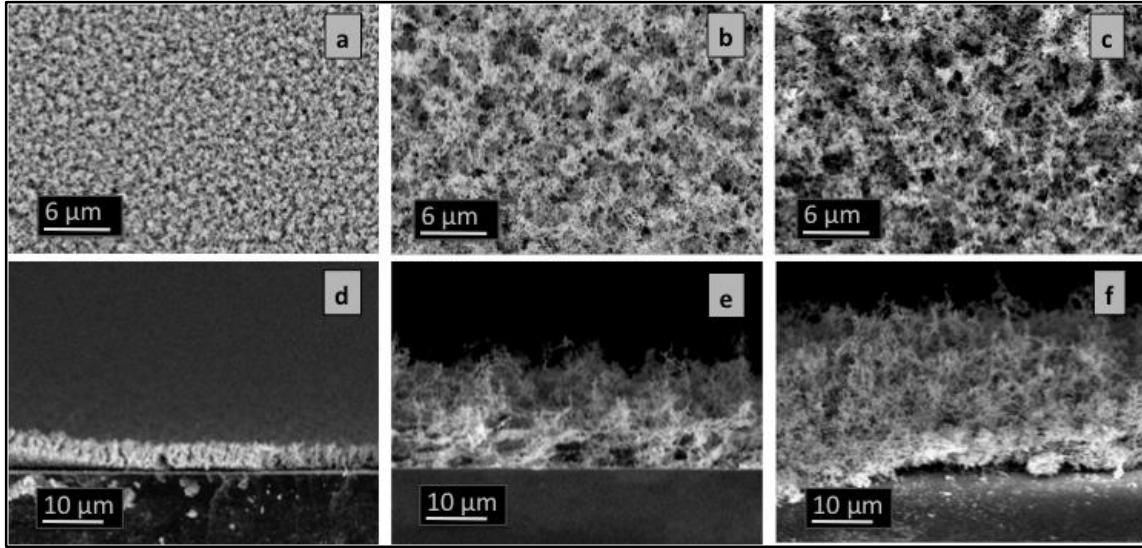


Figure 13 SEM top-view of gold black coatings prepared at N₂ pressure of 0.3 (a) 1.5 (b) & 3.0 Torr (c). SEM cross-sectional view of respective coatings are shown in (d), (e) & (f).

Porosity was calculated by dividing density of gold black with density of bulk gold. In order to calculate density of the gold black, the separate coating was deposited on an extreme lightweight glass slide of known mass and area for mass measurements. SEM was utilized for accurate thickness measurements. Table 1 shows the porosity to be more than 97% in all the coatings. Interestingly, in spite of such high porosity values, we observe 3-D percolating structure in Figure 13.

The electrical conductivity values appear to be 5-7 orders of magnitude lower compared to bulk gold value. As earlier mentioned, the electron transport is more interrupted in smaller nano particles. Therefore coatings produced at higher pressure supposed to be less resistive due to the fact that the particle size increases with pressure [47]. This is not manifested in electrical conductivity measurements shown in Table 1. Coatings Type 3 has two orders of magnitude lower conductivity compared to coating Type 1. *It appears that porosity plays decisive role in characteristic value of electrical conductivity.*

High Resolution SEM revealed increased nano chain diameter at higher inert gas pressure. This can be intuitively explained as following: With more presence of N₂ molecules, average mean free path of gold particles is further reduced, i.e. collision rate increase. The ‘clusters’ made of extremely small particles (~ 1-2 nm scale) are generated. Particles in the clusters would eventually coalesce together to form a larger grain size. Subsequently, average particle chain diameter in coating type 3 is much larger compared to chains in coating type 1.

Table 1 Volume fraction, nano-chain diameter and conductivity of coatings prepared with different N₂ pressure inside the chamber

Coating Type	N₂ Pressure (Torr)	Gold (mg)	Deposition Rate (mg/s)	Volume Fraction	Nano-chain Diameter (nm)	σ_{meas} ($\Omega\cdot\text{m}$)⁻¹
1	0.3	121	1.59	0.025	< 10	1090
2	1.5	121	0.97	0.012	10-20	53.8
3	3.0	121	1.47	0.004	15-30	4.04

Nano-chains of gold black cannot be considered as a tunnel for 1D electron transport. Electrons do not travel in one direction. Their paths have numerous turns and zigzag motion, which leads to collision with the surface. In literature it is shown that in nanoporous gold (NPG) films, this random motion makes electron-surface scattering a major contributor for increased resistivity [48, 49]. Nevertheless, a single nano-wire in NPG is comparatively smoother unit due to much lesser defect density. Therefore, in NPG reduced conductivity compared to bulk gold is mainly due to electron-surface scattering and porosity. In case of gold black, we observed the presence of high density of defects, mainly grain boundaries (i.e. why we chose mention it as ‘nano-chain’ not ‘nano-wire’). In fact, in nano scale systems, grain boundaries are shown to be more responsible for scattering of electron in comparison with surface scattering [26, 50-52]. Apart from grain

boundaries defects, high density of stacking faults and planer defects also increase the resistivity [53, 54]. As previously shown in gold black TEM images, nano-chains are arranged randomly. In some regions these chains are isolated. Particularly in these regions, surface scattering of electrons must be far more dominant. On the other hand, in some regions nano-chains connect together to form clusters, in this case the grain boundaries act as a potential barrier for electrons.

2.4.2 Optical Properties

Figure 14 shows reflectance (a), transmittance (b) and absorptance (1-R-T) (c) of Type 1, 2 & 3 coatings in 2 – 125 μm window of infrared spectrum. The coatings are deposited on a double-sided polished Si substrate. Gold is reference for reflectance and vacuum is reference for transmittance. The coatings are prepared with the pressure and deposition rate that are similar to that of shown in Table 1, with only difference that mass of gold utilized is 230 mg.

Type 1 coating prepared at significantly lower pressure (300 mTorr) is more reflecting at longer wavelengths. The transmittance continues to remain low (< 10%) throughout the spectrum. The volume fraction (1- porosity) of the coating is order of magnitude higher compared to other coating types (Table 1), which explains its tendency to behave relatively closer to bulk gold at longer wavelengths. Absorptance of the coating degrades significantly in LWIR mainly due to increasing reflectance at longer wavelengths.

Conventionally it is believed that metal black coatings with low volume fraction and high thickness have more broadband absorptance. Interestingly, Type 3 coating with lowest volume fraction and highest thickness showed lower absorptance compared to Type 2

coating. In this case, absorptance degrades mainly due to high transmittance observed at longer wavelengths. In Type 2 coating both reflectance and transmittance remained low throughout the spectrum, *therefore there is an optimized porosity required for high absorptance. Extremely higher porosity with high thickness not necessarily results in high absorptance.*

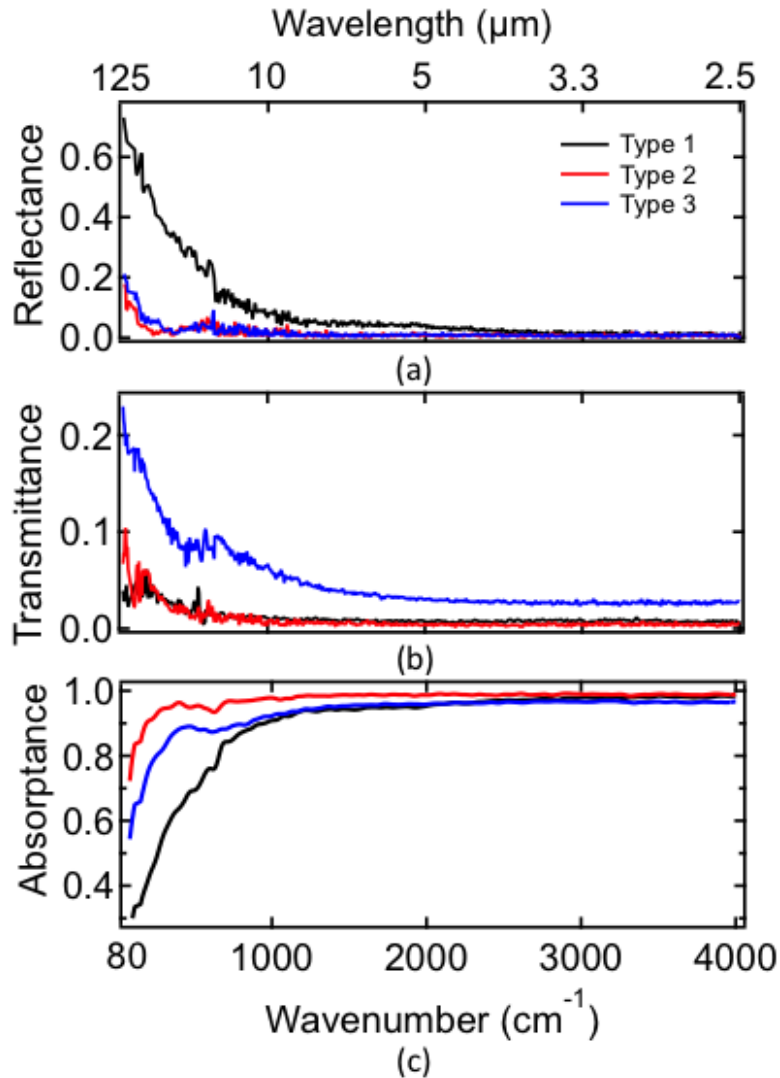


Figure 14 (a) reflectance (b) transmittance (c) absorptance (1-R-T) spectra of coatings prepared with similar deposition parameters shown in Table 1. The absorptance is smoothed using Binomial algorithm.

Ellipsometry is very popular method to calculate the permittivity of the materials, but high absorptance of gold black makes it impractical (especially for coatings thicker than a

few microns). We utilized effective medium theories to model the permittivity to match with the experimental absorptance spectra. Layers of gold black effective medium on silicon substrate is calculated for $A = 1 - R - T$, where R and T are given by three-layer Fresnel's equations ((2.44) & (2.45)). Assuming the Si substrate to be completely transparent in infrared, the (n,k) values are chosen as (3.42, 0). The thicknesses of Type 1, 2 & 3 gold black coatings are measured by cross sectional imaging using SEM.

From Figure 15, it is clearly evident that Maxwell-Garnett and Bruggeman formulas are not in agreement with the measured absorptance values. Reproduced gold black with Maxwell-Garnett formula (Using Eq (2.20)) is completely transparent at this porosity. This result was expected since Maxwell-Garnett formula includes only 'famous' dipolar resonance in isolated particles. In higher volume fractions or percolating networks, multipolar resonances (electric field interactions) are bound to occur which are neglected. For low volume fraction metal blacks, Maxwell-Garnett formula is definitely not the right approach. Bruggeman formula (Eq (2.24)) does allow imitation of the effective medium with percolating networks. Unfortunately due to extremely low volume fractions of gold blacks, Bruggeman formula assumes the gold particles to be isolated in the air medium. In fact Bruggeman is producing exact the same result as Maxwell-Garnett.

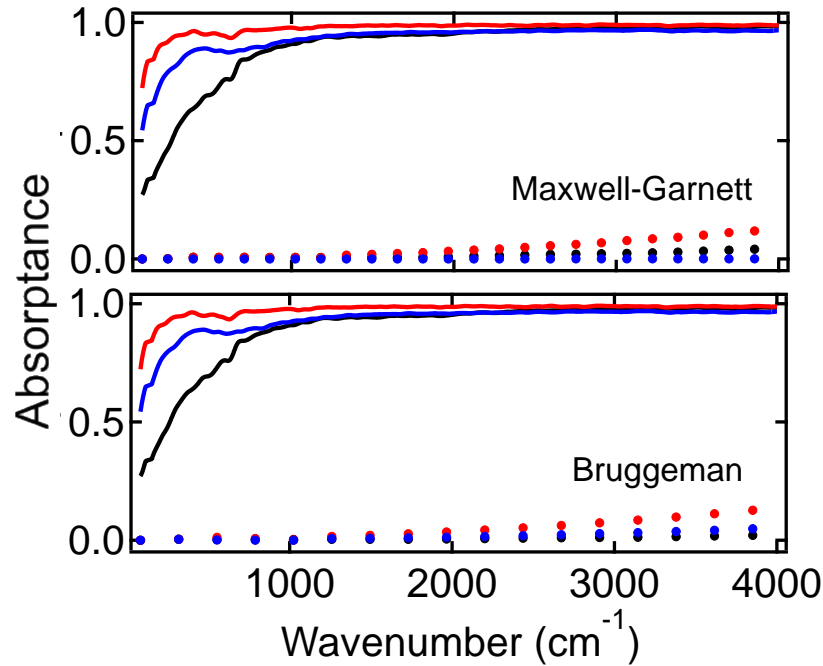


Figure 15 An attempt to reproduce absorbance of gold black coatings using Maxwell-Garnett (top) and Bruggeman formulas (bottom). The volume fractions are shown in Table 1.

Figure 16 (top) shows the fitting of Landau-Lifshitz-Looyenga (LLL) formula (Equation (2.25)) to the experimentally measured absorbance of Type 1,2 & 3 coatings. Similar to Maxwell-Garnett and Bruggeman, LLL formula considers only volume fraction as fitting parameter. Though, fitting is surprisingly accurate in far-IR. Even though, one can easily spot the mismatch at higher wavenumbers. The fitting volume fractions are shown in Table 2.

Using only volume fraction, as a parameter is not enough to reproduce the absorbance of metal blacks for a broad range of spectrum. The information on topology becomes extremely important for higher wavenumbers, which is included in Bergman Formalism in terms of spectral density function $g(N,f)$. In Figure 16 (bottom), the measured absorbance is fitted to Bergman Formalism (Eq. 2.27) and one can observe that fitting is more appropriate even for higher wavenumbers.

Volume fractions of the coatings are inputted for all the types of coating from measurements as shown in Table 1. Mainly the two fitting parameters are loss factor α and percolation strength g_0 . The loss factor is fitted in Drude model (Eq 2.10) to calculate the permittivity of the particle (ϵ_p). Since we are in infrared region, we neglect the interband transition term in Eq (2.10). The loss factor quantifies the difference between the damping constant in bulk gold and our gold black coatings. High density of grain boundary defects and surface scattering in gold black nano-chains increase the damping significantly compared to bulk gold. The higher damping constant results in significantly different permittivity for gold black particles as well. Parameter (g_0) is percolation strength at $N \approx 0$, which is fitted in (2.27) to match both reflectance and transmittance with the experiment.

Thicknesses of Type 3 coatings were not constant throughout the sample. Even with naked eyes, one could easily spot the gradient nature of the thickness, i.e. Si substrate was slightly visible on one side of the sample while the coating appeared far more opaque on the other side. SEM showed 10 μm thickness variation from one end to the other. Hence, we chose to input 25 μm thickness for calculation of effective permittivity of Type 3 coating.

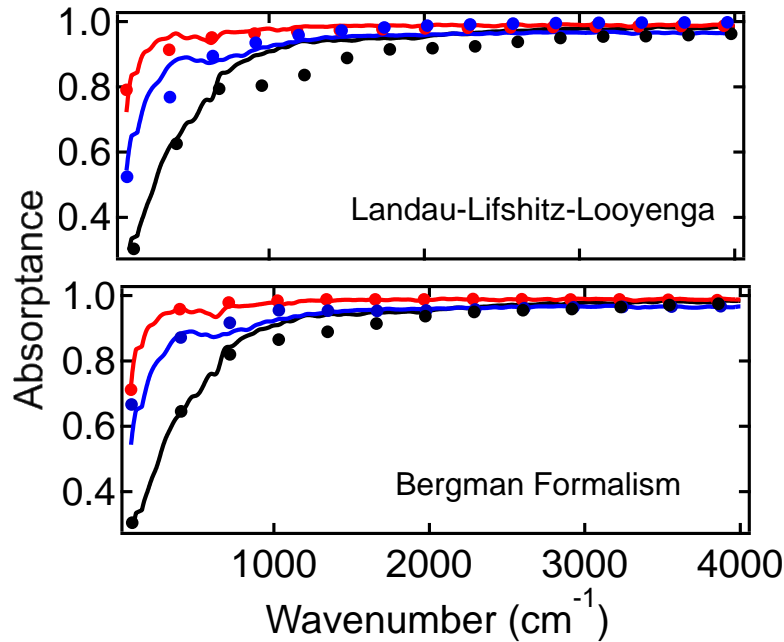


Figure 16 The experimental absorbance is fitted to Landau-Lifshitz-Looyenga (top) & Bergman Formalism (bottom) for calculation of effective permittivity. The fitting parameters are shown in Table 2. Solid lines: measured values, markers: calculated values.

In Bergman Formalism, there is always a trade between two fitting parameters g_0 & α . hence either the value of loss factor or percolation strength cannot be considered as full proof. However, certain trend is followed, i.e. in Type 1 coating the loss factor tends to remain on higher side. If one tries to fit a low loss factor for Type 1 coating, the calculated spectrum does not match the actual result for fitting of any percolation strength. *The loss factor reduces with the increasing pressure of the coating. Interestingly the nano-chain size increases with the pressure [18]. One can imagine less surface scattering in larger particles, leading to lower loss factor.*

Table 2 Parameter d_{meas} is measured thickness, α is fitted loss factor in Eq (2.10) neglecting inter-band transition term, g_0 is fitted percolation strength in Bergman Formalism, (LLL) is the fitted volume fraction LLL formula to match the experimentally measured absorptance as shown in Figure 16 (top), and f (Bergman) is the volume fraction obtained experimentally (From Table 1).

Coating Type	d_{meas} (μm)	α Looyenga	α Bergman	g_0	f Looyenga	f Bergman
1	3.3	1	24.4	0.221	0.05	0.025
2	22	1	17.7	0.058	0.015	0.012
3	20-30	1	10.5	0.038	0.004	0.004

The solutions of LLL and Bergman Formalism are wavenumber dependent real and imaginary permittivities. The complex refractive index can be calculated by Maxwell's relation $n = \epsilon^{1/2}$. Figure 17 shows the sets of refractive (n) and absorptive (k) parts of the indices calculated using LLL and Bergman Formalism. One can observe that both the theories generate n & k with 'almost' similar type of response. However, one tends to 'trust' outcome from Bergman Formalism more due to more accurate fitting throughout the spectrum.

The negative dispersion of refractive part (n) is a typical metallic behavior. Interestingly, for gold black n stays constant at unity for most part of the spectrum, and exhibits 'negative' dispersion at longer wavelengths. For bulk metals the 'negative' dispersion of n begins right below the plasma frequency. Values of the imaginary part are also much lower to that of bulk value. Thus, extremely low volume fractions and percolation causes gold black to behave almost as if 'metallic vacuum'

For metals both n & k are governed by how easily electrons can 'travel' (or polarize) within the space inside the material. The free electrons in bulk metals absorb the incident EM radiations and respond to re-emit EM radiations by oscillating back around the origin (oscillating charge produce radiations!). *In case of gold black the average particle size is*

much smaller than the mean free path of electrons in bulk gold. External electric field (through incident light) causes the electrons to absorb the energy and accelerate, however electrons encounter the surface or grain boundary defects more often in gold black and they transfer the energy to generate phonon vibrations and 'heat up' the coating. Therefore inability of electrons to travel freely in gold black structure makes it much less susceptible to the polarization. This leads to lower real and imaginary part of refractive index compare to bulk gold.

Reflectance of gold black at longer wavelength is increasing as shown in Figure 14. This is easily explained increasing n and k value at longer wavelengths (Fresnel's equations). Also the Type 3 coating is behaving more transparent at longer wavelengths, which is also explained by low absorption coefficient ($\alpha = 4\pi k/\lambda$) at longer wavelengths. *In brief, the gold black has n value close to unity and also low k value, this results in minimum reflectance from the air-gold black interface and low k value provides enough extinction of infrared radiations passing through the gold black with proper high thickness.*

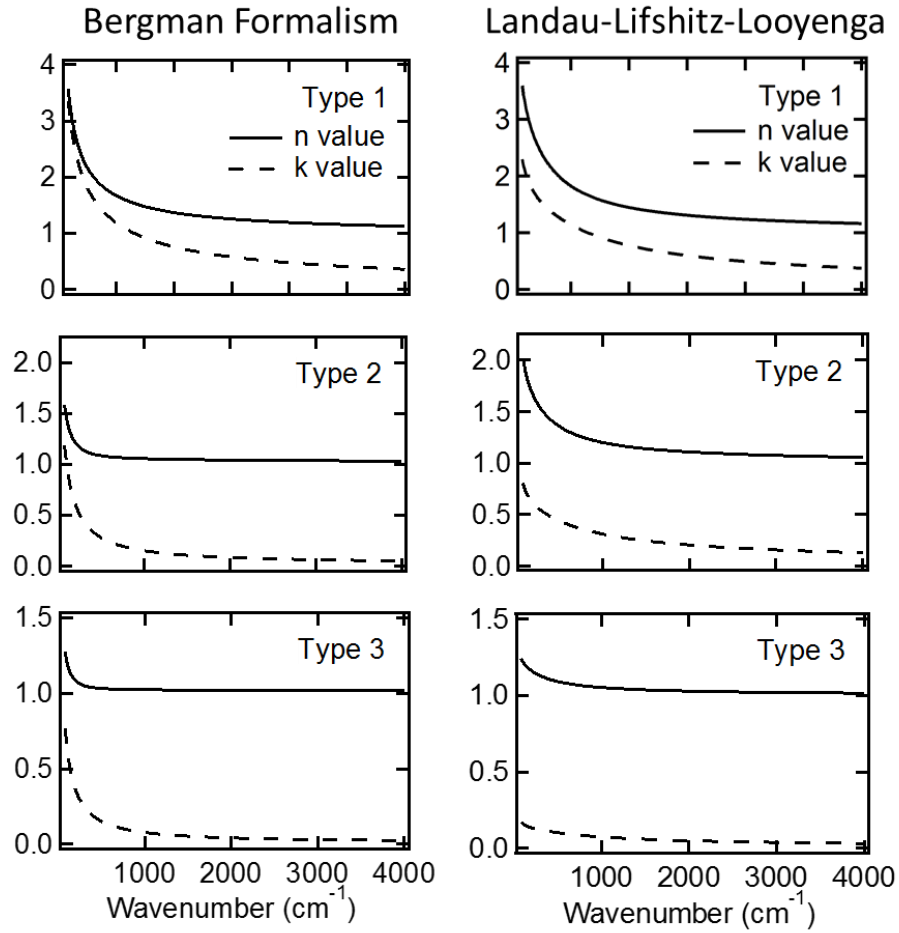


Figure 17 Refractive index (n) and extinction coefficient (k) of all Types of coating calculated using LLL(left) and Bergman Formalism (right).

2.4.3 Discussion on Spectral Density Function

The spectral densities $g(N,f)$ obtained from fitting Bergman Formalism to the measured absorptance is plotted in Figure 18. We utilized SCOUT software and ‘massaged’ spectral density shape to fit the calculated Reflectance & Transmittance to the measured spectra with the accuracy. The flexibility of manually changing the shape of the spectral density to match the optical spectra makes Bergman Formalism more universal compared to other effective medium theories [55, 56]. In this section we will also briefly review literature for better understanding on spectral density.

Spectral density of Type 1 coating is weighted more $\sim N = 0$, since the topology is more 'connected'. In fact from Eq (2.31), one can see that spectral density at $N = 0$ represent the percolation strength. The broad but weak peak observed at $N = 0.8$ represent isolated particle in Type 1 coating. In Type 2 & 3 coatings it can be observed that spectral density components at $N = 0$ are significantly reduced due to low percolation strength (Table 2) in these coatings. The strong peak observed at $\sim N = 0.2$ suggests there is more isolation of particles in these coatings. The broadening of the peak generally represents the large irregularity in the shape. These interpretations are considered based on the SEM top-view images shown in Figure 13. Nevertheless, low percolation strength leads to low conductivity, which is again in line with measurements shown in Table 1.

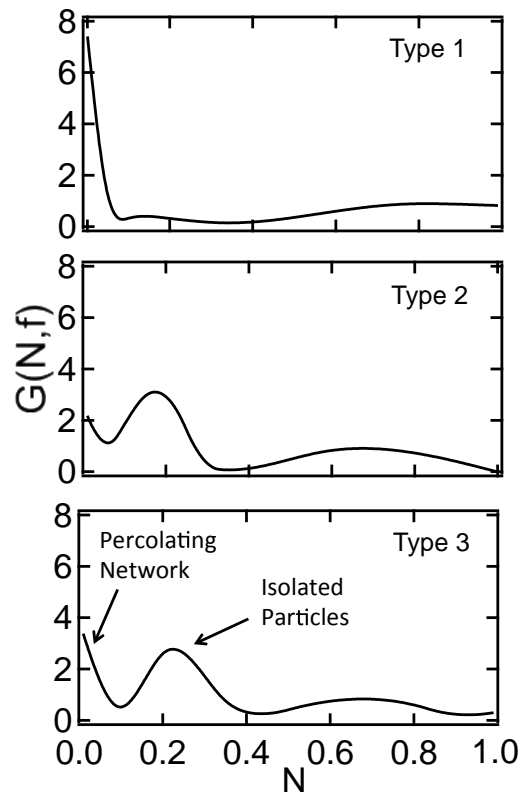


Figure 18 Bergman spectral densities of all the coatings from Table 1 are calculated using interpretation in [55].

In far infrared spectrum the percolation strength g_0 ($n \approx 0$) is far more dominant, and fitted spectrum is almost independent of shape of the spectral density $g(N,f)$ [57]. In fact at a given percolation strength, when we changed the spectral density shape, the effect in fitted spectra from $1000 - 4000 \text{ cm}^{-1}$ was clearly visible, but fitted spectra in far infrared remained unchanged altogether. One can conclude that, at lower wavelengths topological information is more crucial for obtaining better fit. This is also mathematically explained by calculating frequency dependent permittivity constant (t) in Bergman Formalism [23]. Substituting $\epsilon_m=1$ and replacing ϵ_p with Drude's model for bulk gold in (2.29), one can calculate real (t_1) and imaginary (t_2) permittivity constants. It is clearly evident that for wavenumbers lower than 1000 cm^{-1} , both t_1 and t_2 are order of magnitude smaller compared to values of same in mid-IR. Hence, $t \sim 0$ in for wavenumbers lower than 1000 cm^{-1} , which leaves Bergman permittivity independent of spectral density in this spectral region (far-IR). This explains even though Landau-Lifshitz-Looyenga theory lacks the capability to include topological resonances, it still provides decent fit for lower wavenumbers.

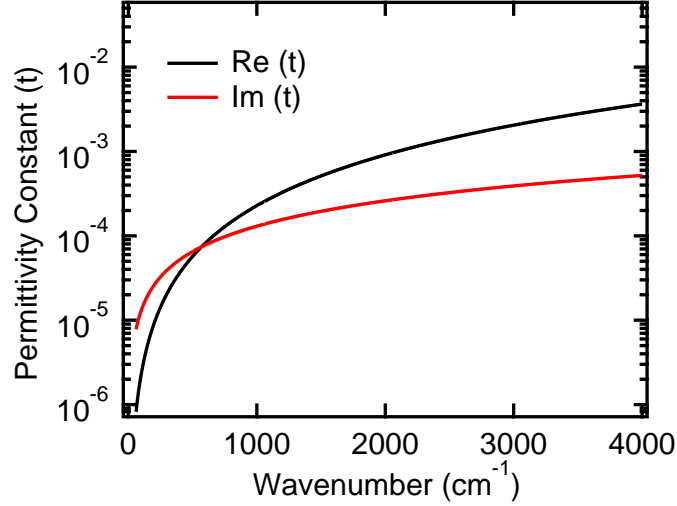


Figure 19 Wavenumber dependence of permittivity constant (t) for $\epsilon_m = 1$ and substituting bulk gold Drude model as ϵ_p .

As observed in previous figure, spectral density holds crucial information on topological resonances of the geometry, but in case of Bergman Formalism it is generally not known, i.e. why one needs a computer power to be able to change the shape manually to fit with the experiment. For other simple effective medium theories, analytical expression for spectral density can be calculated using following formula [40];

$$g(N, f) = \lim_{\beta \rightarrow 0} \frac{-1}{\pi i f} \left(\epsilon_{eff}(N + i\beta) \right) \quad (2.52)$$

For Maxwell-Garnett formula, the spectral density ends up being a delta function, with the peak at $N \approx 1/3$ for low volume fraction.

$$g(N, f) = \delta \left(N - \frac{1-f}{3} \right) \quad (2.53)$$

Sharp peak at $N \approx 1/3$ represent the dipolar resonance. With increasing volume fractions, weightage on of spectral density function shifts towards $N \approx 0$ [58]. Even for very high volume fractions percolation is neglected, leaving Maxwell-Garnett spectral density with very limited topological response. Similarly spectral density for Bruggeman formula has

a following analytical expression [59];

$$g(N, f) = \frac{3f-1}{2f} \delta(N) \theta(3f-1) + \frac{3}{4\pi f u} \sqrt{(N-x)(y-N)} \theta(N-x) \theta(y-N) \quad (2.54)$$

Where, $x, y = \frac{(1+f \pm 2\sqrt{2f-2f^2})}{3}$ and θ is the Heaviside function. The first term in

the right hand side corresponds to the percolation strength. Similarly for LLL formula

one can calculate the spectral density function [60];

$$g(N, f) = f^2 \delta(N) + \frac{3\sqrt{3}}{2\pi} \left((1-f)^2 \left| \frac{N-1}{N} \right|^{1/3} + f(1-f) \left| \frac{N-1}{N} \right|^{2/3} \right) (1 - \delta_{0,N}) \quad (2.55)$$

Again, the first term on right hand side is percolation strength. From Figure 20, one can easily observe that, for Bruggeman, percolation strength is null for $f \leq 1/3$. Therefore in case of metal blacks, Bruggeman formula would ‘assume’ all the particles to be isolated, which is obviously not true. On the other hand for LLL formula, even at extremely low volume fractions, percolation strength is non-zero. This explains why LLL formula provides much better fit for gold black compared to previous two theories. Nevertheless, volume fraction is the only parameter to play with during the fitting of the spectra, which limits the accuracy. LLL can still be utilized for performing quick calculations on metal black coatings.

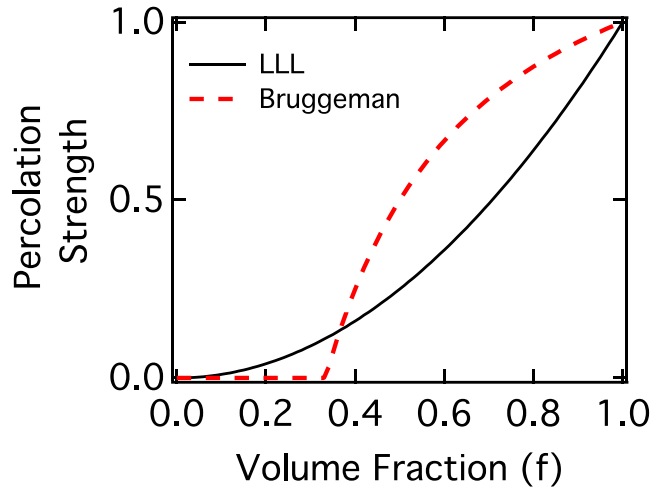


Figure 20 Percolation strength of Bruggeman and LLL effective medium theories.

Coming back to Bergman Formalism, Theiss et al. has done substantive work [61-66] to parameterize the spectral density of Bergman Formalism, using porosity, percolation strength *and broadening parameter of more or less isolated particles* [67].

2.5 Conclusion

Gold black coatings are thermally evaporated at 0.3, 1.5 & 3.0 Torr N₂ pressure. Volume fractions and conductivities are found to be inversely proportional to ambient pressure. Coating prepared at 1.5 Torr maintains high absorptance for a broad spectrum from 2-125 μm. While coating produced at 0.3 and 3.0 Torr, respectively exhibited high reflectance and transmittance respectively at longer wavelengths. There is an optimized volume to gold fraction ratio for high absorptance, which in our case is achieved at 1.5 Torr pressure.

Experimentally measured absorptance spectra are fitted using different effective medium theories, such as Maxwell-Garnett, Bruggeman, Landau-Lifshitz-Looyenga and Bergman. Unlike all the other theories mentioned, Bergman Formalism includes the necessary information regarding topological resonances in the form of spectral density

function. The coating prepared at lower ambient pressure are more percolating, which is considered in the spectral density plot in the form of a peak at $N \approx 0$. Spectral density function also explains the failure of Maxwell-Garnett and Bruggeman to reproduce gold black effective medium. Even though volume fraction is the only parameter included Landau-Lifshitz-Looyenga formula, due to non-zero percolation strength at all volume fractions there is a reasonable agreement with the experimental data, especially in far-IR region.

The refractive indices calculated using Landau-Lifshitz-Looyenga & Bergman Formalism suggest that extremely low value of refractive index (n) and extinction coefficient (k) with high thickness results in absorption of infrared. Becker et al. have rightly called gold black as 'diluted metal'.

CHAPTER THREE: AGING STUDIES

3.1 Background

Gold black is extremely fragile, and long term stability of its absorbance is a significant practical concern. [68]. Therefore, in order to study the effects of aging, we fabricated gold-black coatings with different porosities and characterized the changes in electrical resistance, thickness, and reflectance over time, both at room- and elevated-temperatures. Though gold-black films have been reported to shrink with age [24], our observations challenge the universality of this effect because in contrast we observe a swelling. We did observe a drop in electrical resistance over time at all temperatures which hence seems to be a universal effect. Based on our results, resistance and thickness can change independently and oppositely, and hence they are uncorrelated. Thus, the decrease in resistance is not due to macroscopic changes in morphology.

We used High Resolution Transmission Electron Microscopy (HR-TEM) to study grain boundaries and twinning defects in gold black nanoparticles, had been done for gold nanoparticles fabricated differently [69-72]. Porous gold-black is a nanoparticle aggregate with large numbers of such features. Individual nano-crystallites are as small as ~ 2 nm, and for these we observe that room temperature thermal energy suffices to grow the grains by annealing out the defects at the boundaries [73, 74]. The smaller the crystallite size, the more unstable they are to growth. Similar coalescing of silver nanoparticles at room temperatures when surfactant is evaporated has been reported [75, 76]. These studies also reported a large drop in resistivity correlated with coalescing process. We suggest that such room temperature grain growth, without loss of porosity

explains the drop in electrical resistance observed over time in gold-black films. These effects are correlated with an increase in far-IR absorptance, so that aging of gold-black coatings is not necessarily detrimental to their infrared applications.

3.2 Isothermal Grain Growth Kinetics

Grain growth kinetics explains the thermal stability of the granular structure through grain growth mechanism. In poly-crystalline materials, the main driving force for the grain growth is to minimize the free energy, stored in grain boundaries and lattice strains [77]. The atoms with poor packing, at adjacent grain boundaries have higher energy compared to atoms within the lattice frame. Due to this energy mismatch, atoms within the lattice frame (close to the surface) gain enough energy to diffuse from one crystal lattice to the other at the elevated temperatures. This process pushes the grain boundary in the certain direction until energy equilibrium between the different grains is reached. During this process, larger grains consume smaller grains, leaving the system with as minimum energy as possible. Importantly, total number of atoms in the system still remains the same.

Since the surface energy for smaller particle is higher, the rate of grain growth is inversely proportional to size of the particle [78, 79].

$$\frac{dD(t)}{dt} \propto c_1 \frac{m_{gb}}{D(t)} \quad (3.1)$$

Here, curvature is equivalent to size using a proportionality constant c_1 , and m_{gb} is grain boundary mobility. Solution to this equation is given by;

$$D(t)^2 - D_0^2 = K_T t \quad (3.2)$$

Here, $D(t)$ is grain size at a particular annealing time t , d_0 is the initial grain size. K_T is rate constant (dependent on Temperature (T)), which is expressed by Arrhenius type equation;

$$K_T = \frac{1}{\tau} \propto \exp\left(\frac{-E_A}{K_B T}\right) \quad (3.3)$$

Here, K_B is Boltzmann's constant, E_A is the activation energy and τ is the structural relaxation time. Eq (3.2) is valid for only poly-crystalline grain growth. For nano-crystalline material, generalized parabolic model is utilized, which is also known as grain growth kinetic equation [80].

$$D(t)^n - D_0^n = K_T t \quad (3.4)$$

Here, n is grain growth exponent. This equation is doesn't properly explain grain growth in nano-crystalline materials, because it does not consider the pinning mechanism.

Pinning opposes the grain growth driving pressure generated by energy stored in grain boundaries and other defects. When both, pinning and driving pressure are equal, grain ceases to grow beyond certain size, hence there is a limiting grain size (D_∞) at certain temperature. By subtracting the pinning constant from (3.1), we exclude the possibility grain size increasing infinitely. By integrating for time limit of 0 to t , we receive following expression from Burke [81];

$$\frac{D_0 - D(t)}{D_\infty} + \ln\left[\frac{D_\infty - D_0}{D_\infty - D(t)}\right] = K_T t \quad (3.5)$$

Since this equation considers the limiting term to be independent of grain size, it does a give better but not the complete picture of grain growth in nano-crystals. Here, we utilized slightly modified approach suggested by Mazurin, in which, the limiting term is

directly proportional instantaneous grain size [82]. This approach explains the isothermal grain growth in nano-crystalline by relaxation from an excited to an alleviated state through following structural relaxation expression;

$$D(t) = D_{\infty} + (D_0 - D_{\infty}) \exp\left(-\left(\frac{t}{\tau}\right)^z\right) \quad (3.6)$$

Here, the exponent z is relaxation order, which is assumed to be 0.5 [80]. In nano-crystalline materials, electrical relaxation model provides the information on resistivity connected to grain growth, lattice strain relaxation & structural relaxation [82, 83]. Electrical relaxation model grain size parameter is replaced by resistivity;

$$\rho_s(t) = \rho_{s\infty} + (\rho_{s0} - \rho_{s\infty}) \exp\left(-\left(\frac{t}{\tau}\right)^z\right) \quad (3.7)$$

Where ρ_{s0} and $\rho_{s\infty}$ are normalized sheet resistance values time $t = 0$ and is $t = \infty$ respectively.

3.3 Results

3.3.1 Structural Relaxation

Figure 21 shows the nano-structural changes due to aging at room temperature. The TEM electron dose was 4.13×10^5 electrons/nm²-sec for Figure 21 (a) and (b), while for Figure 21 (c) and (d) it was 3.75×10^6 electrons/nm²-sec. In Figure 21 (a) the grain boundaries between the loosely adjoining particles are clearly visible within the highlighted circle. Figure 21 (b) presents the same region after ninety days at room temperature, and grain boundaries are no longer clearly distinguishable within highlighted circle, though the aggregates structure still consists of multiple and overlapping grains. After aging, there are fewer very dark regions, indicating that the

vertical stacking of overlapping grains is reduced by lateral necking between grains, which is a known behavior coalescing of particles during annealing[84].

Figure 21 (c) shows a different region of the sample, which has a high density of twin defects, where one part of the crystal is a mirror image of the other. The example of a defect is highlighted in the image with rotated (111) planes merging at a twin boundary (red line). Figure 21 (c) also shows that the characteristic size of single crystal regions within gold black can also be small as ~ 2 nm due to these defects. Figure 21 (d) presents a TEM image of the exactly same region after 90 days at room temperature aging. Single crystal regions near the edges of grains A and B have moved towards each other and formed a neck, which operated as an atomic diffusion path for further coalescence, the process known as aggregation [85]. In region B, after aging, twinning defects are solved partially, but a Moire pattern appears due to overlapping of (111) and (200) planes, the most dominant planes in FCC. The dark regions, which represent overlapping of multiple grains, appear more crystalline after aging. This is due to unification of overlapping grains, assisted by both grain rotation and surface diffusion [86]. (111) planes are more dominant after aging which forms a more stable structure at room temperature in FCC crystals.

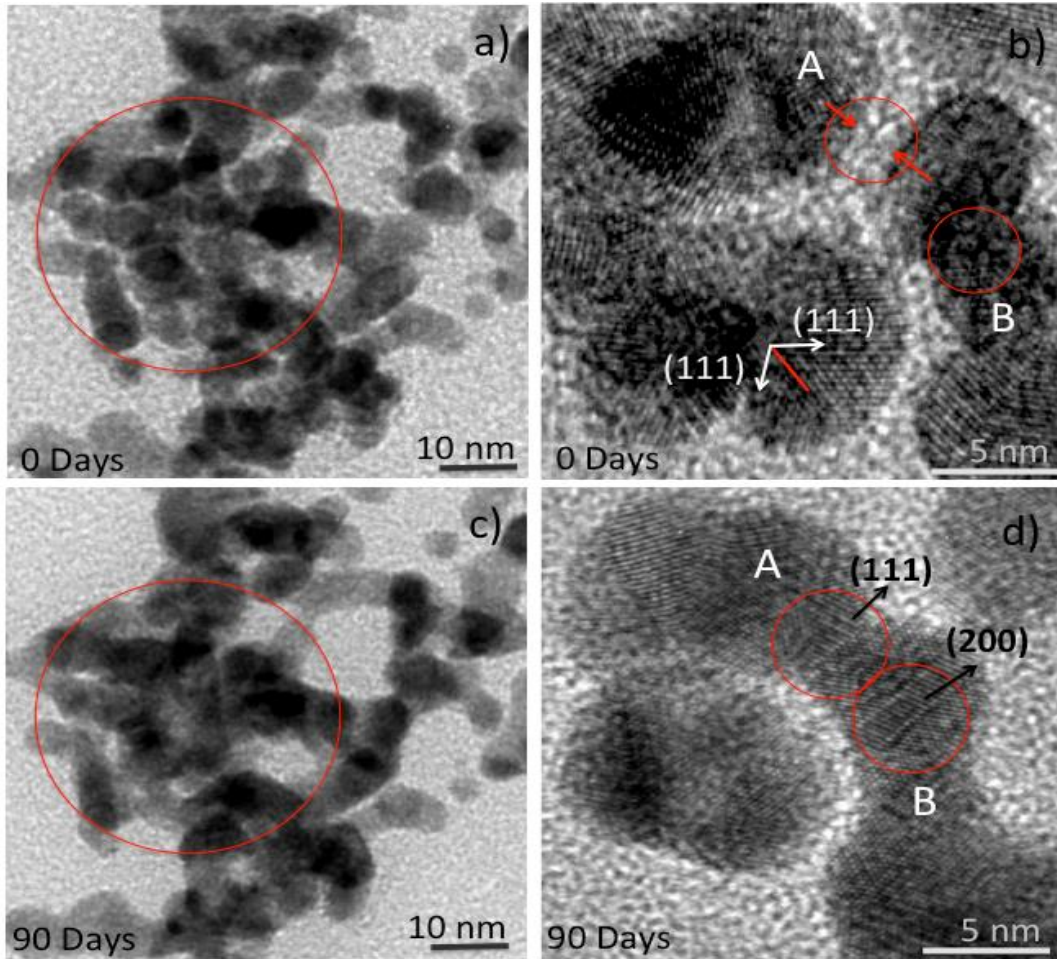


Figure 21 TEM image of gold black feature before (a,b) & after (c,d) aging of 90 days

3.3.2 Electrical Property

Figure 22 presents the effect on sheet resistance of room-temperature aging for two separately-prepared batches of films. In batch 1, the sheet resistance on three different samples was measured twice after ninety days, and the value was found to be $55 \pm 37 \%$ of that for the as-deposited films. Seven samples measured from batch 2 after sixty days showed a sheet resistance value that was reduced to $43 \pm 18 \%$ of the as deposited value.

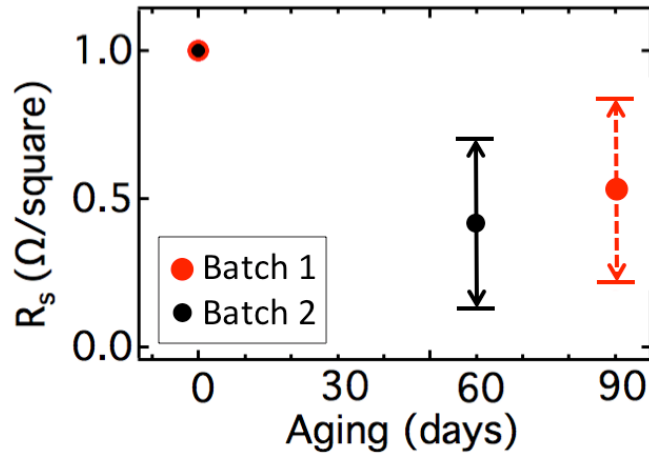


Figure 22 Sheet resistance aging in ninety days at room temperature. Extended arrows and dot at the center suggest the scale of standard deviation and mean value respectively.

Figure 23 presents cross-section SEM images of the same region of a gold-black film before and after aging for 90 days at room temperature. The thickness on day one was $19.53 \mu\text{m}$ and $21.24 \mu\text{m}$ after ninety days. Considering the misalignment by 5 degree in SEM imaging, maximum possible error can be only $\pm 40 \text{ nm}$. In fact comparing the relative position of characteristic morphological features in the fore- and back-grounds of the images, we can observe that misalignment is negligible. We attribute the difference in the thickness to ‘expanding’ of the structure due to possible presence of water vapors at atmospheric pressure. Over all we can conclude that, aging 90 days at room temperature caused no observable decrease in the film thickness, an observation that was repeated for numerous samples.

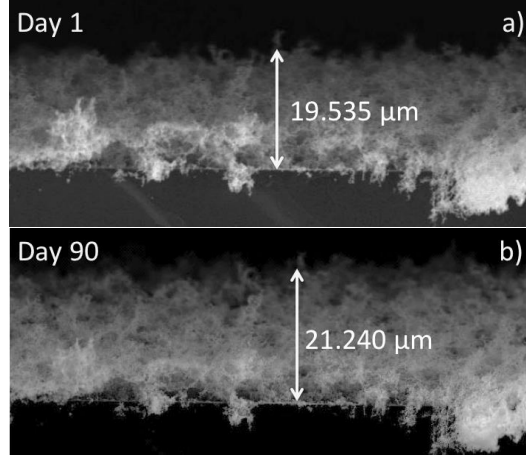


Figure 23 SEM Cross-section view of exact same spot before (a) and after (b) aging.

Figure 24 (a) & (b) presents the sheet resistance data vs. time for a set of isothermal annealing conditions for type 2 and 3 coatings, respectively. The different samples were held at different constant temperatures in the range 55 – 100 °C on a hot plate for up to two hours. The sheet resistance shows a rapid initial drop followed by a tendency to stabilize at a constant value. Resistance of type 3 coatings dropped more and stabilized sooner compared to type 2 coatings. Curves for type 1 coatings were similar to those for type 2. Once the nano-crystal reaches a certain size, it ceases to grow further at a particular temperature. Isothermal grain growth is explained by an electrical relaxation model of the form [82].

$$R_s(t) - R_{s\infty} = (R_{s0} - R_{s\infty}) \exp\left(-\left(\frac{t}{\tau}\right)^z\right) \quad (3.8)$$

Sheet resistance terms R_0 and R_∞ are related to grain size at times $t = 0$ and ∞ , respectively. Here, instead of resistivity, sheet resistance is utilized on the assumption of small variations in thickness with aging. Figure below clearly shows matching between experimentally measured normalized sheet resistance and theoretical values.

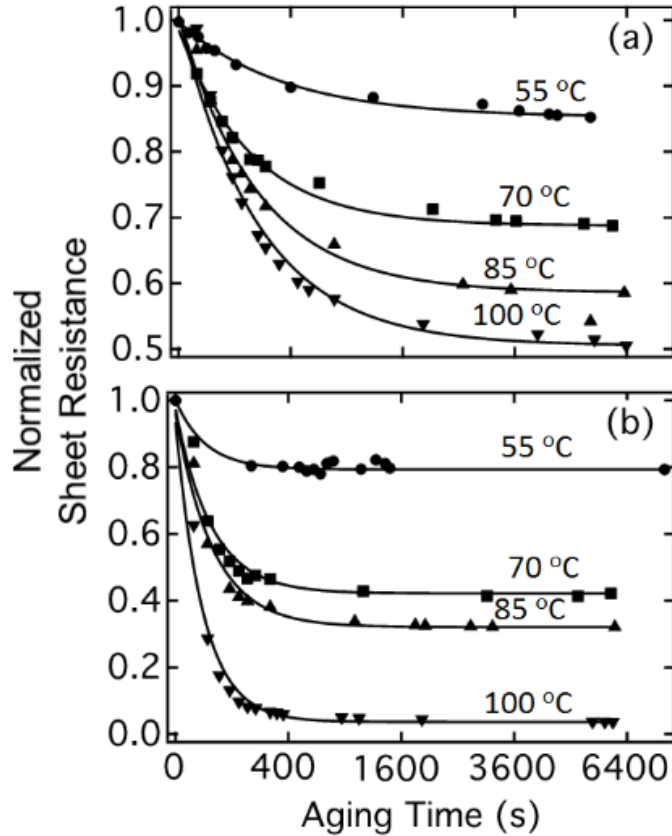


Figure 24 Sheet Resistance plotted against time at different temperatures for coating Type2 (a) & Type 3 (b) from Table 1. The dots are experimental data and lines are fitted with Eq (3.9)

Although, in Figure above thickness is considered to be unchanged during the aging process, actual SEM measurements showed increment in thickness by 9.7% and 0.9% after a couple of hours at 55 and 70 °C respectively. While thickness dropped by 11% after aging at 100 °C, which suggests that at high temperatures aging also causes undesired macroscopic changes. Importantly, swelling of the structure is still observed at low temperatures.

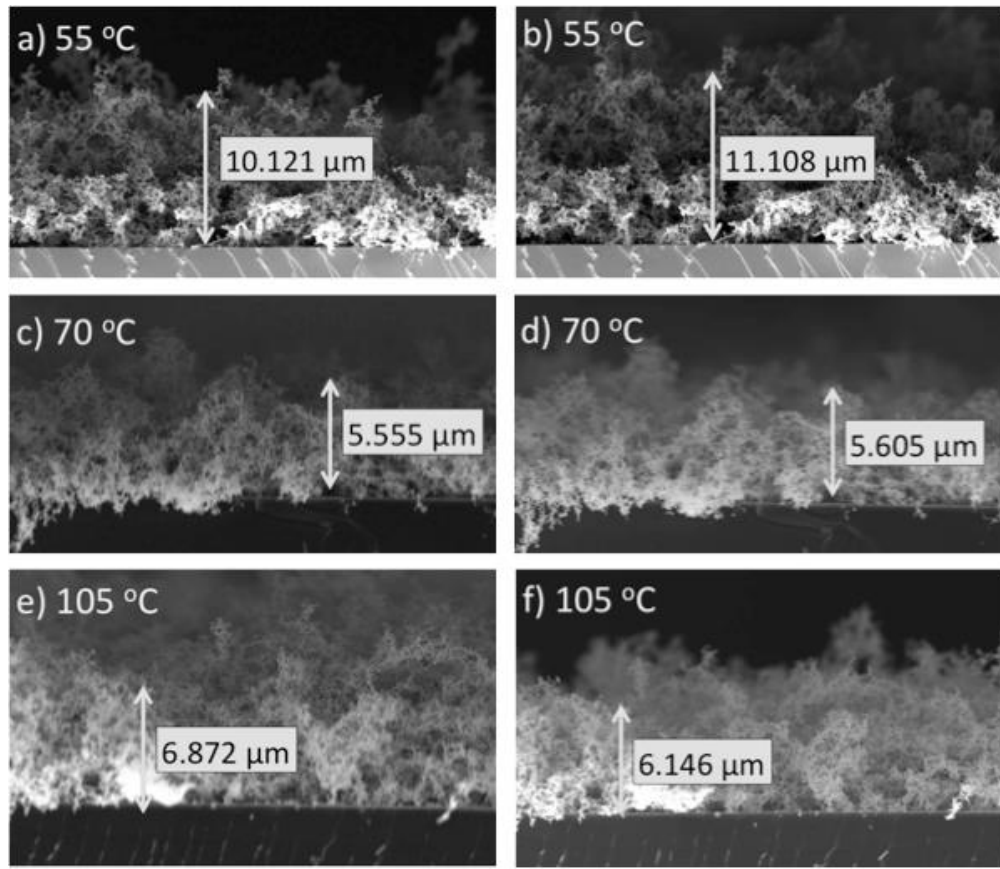


Figure 25 SEM Cross-section view of exact same spot before (a,c,d) and after (b,d,f) aging at respective temperatures for two hours

Figure 26 shows the relaxation time τ extracted from fitting the equation (2) on isothermal sheet resistance data. Note that τ is the time required for sheet resistance to drop to $1/e$ from its initial value. Interestingly, relaxation times fluctuate a lot for coatings with lower initial resistance, but high initial resistance coatings consistently show extremely small relaxation times. The small relaxation times for Type 3 coatings suggest rapid aging during the first minutes following deposition.

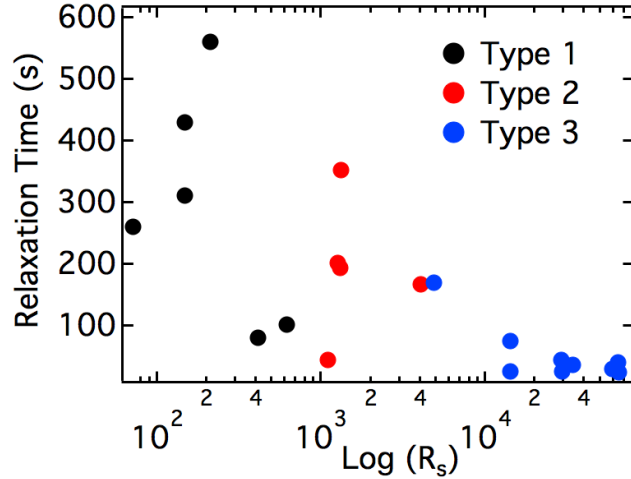


Figure 26. Relaxation time is plotted against initial sheet resistance of porous gold coatings.

3.3.3 Optical Property

The reflectance R was measured in the range 22 to 125 μm wavelength on the porous gold coatings deposited on a gold substrate for optical aging experiments. Scattering is neglected since structural variations are much smaller than IR wavelengths, so that absorbance $A = 1 - R$. Figure 27 shows that after coating aged in laboratory for ninety days at room temperature, R decreased strongly across the spectrum. Reflectance of a *conducting porous* layer can be reproduced using following simplified dielectric function [23].

$$\varepsilon(\omega) = 1 + i \frac{\sigma}{\omega \varepsilon_0} \quad (3.9)$$

Eq. (3.9) is Bergman Formalism in conductivity form, applicable in only far-IR, since conductivity is complex and frequency dependent at shorter wavelengths [38]. Gold black layer reproduced using Eq (3.9) on gold substrate with 100 S/m conductivity and 19.53 μm thickness (measured using SEM in Figure 23 (a)) match reasonably well with the experiment for the coating before aging. Reflectance after 90 days of interval match very well with the reproduced gold black layer with conductivity 115 (S/m) and 21 μm

thickness. Increased thickness with aging is also observed in SEM image in Figure 23 (b). The overall conclusion is that aging tended to increase absorptance after ninety days for the samples studied at room temperature. Calculation also suggest that reflectance can be drastically reduced further at 300 (S/m) conductivity at 21 μm thickness (not shown here). However, also according to (3.9), more than 300 (S/m) conductivity will results in un-desired increase in reflectance (not shown here).

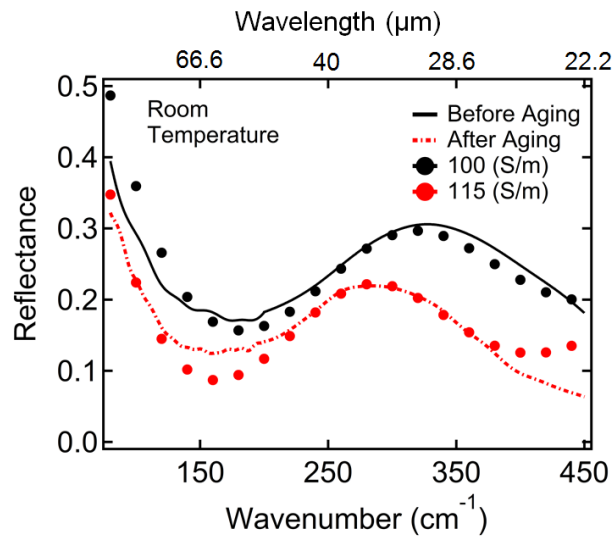


Figure 27. Reflectance spectra measured before (solid black) and after (dashed red) aging for 90 days of period. Calculated reflectance spectra (dots) at different conductivities using Eq. (3.9).

Drop in the reflectance was also observed at elevated temperatures as shown in Figure 28. Both coatings at 55 and 70 °C, showed significant drop in reflectance in Far-IR after a couple of hours of aging. In fact at 55 °C, average reflectance across entire spectrum dropped to 0.40 from 0.56 of initial value. Partial collapse and too much heating at 100 °C may have caused collapsing of the structure and too much rise of the conductivity, hence the not much reduction in reflectance is visible.

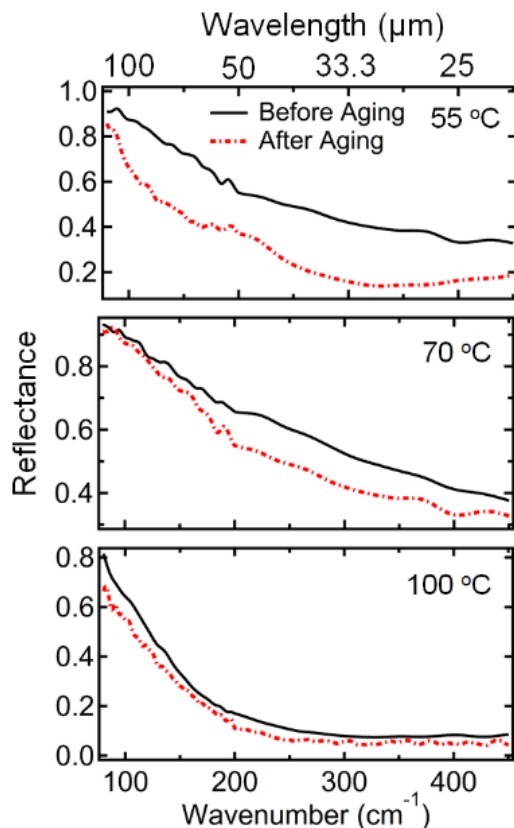


Figure 28 Reflectance spectra measured at two hours of interval at different elevated temperatures.

3.4 Discussion & Conclusion

The reason behind such high density of defects in gold black might be the fabrication process itself. During the evaporation, the gold particles collide with N_2 gas molecules and loose energy, and they collide back with one another. After a number of collisions they lose energy and are not able to further coalesce seamlessly to form a single crystal grain. The structure ends up being over-lapping of nano-chains consisting of large number of grain boundaries and lattice mismatch. In fact in FCC structures, lattice mismatch and mistacking of atoms during grain nucleation is a common reason for formation of twin defects [87]. These twin defects are also formed due to the difference

of binding energy between the local structure around a twin boundary and other parts of the grain.

Advena et al. have shown that these coatings collapsed by 50 % with aging of 7 days, became less porous and more conductive [24]. In contrast, we found no evidence of collapse. Hence, the observed drop in sheet resistance is attributed to coalescing of particles and defect annealing at the nano-scale, rather than micro-scale collapse as previously suggested. Ingham et al. also have shown that as the closely spaced nano particles are heated, the defects are annealed out first. This is followed by (or manifests concurrently) aggregation of particles [85]. As the aggregation is completed, grain growth (process of removal of defects such as twinning) still continues for long period until particles eventually merge into a single spherical grain. However, merging in to single crystallite is the final stage, and it requires high temperatures. Importantly, pinning mechanism is also present in nano-crystalline material. Considering this, *partial* process of coalescing of grains occurred in gold black, which removed defects and deformations to *some extent* at room temperature. This process is substantial enough to cause significant drop in sheet resistance with aging, which was found to be independent of thickness.

In type 1 & 2, are comparatively closely packed morphologies, may have resulted in more dominant aggregation process. During the aggregation, new interface defects continue to be generated due to formation of neck [84]. Although, pre-existing defects may reduce in density, new defects are born, which continue to provide potential barrier to free electron movements. This could have led to high relaxation times in these coatings. On the contrary in type 3 coatings with an order of magnitude higher porosity,

the nano particles are more separated. The defects are annealed out within grain itself due less probability of further aggregation of grains. This led to an early stabilization of grain size, which was reflected as short relaxation times.

The aging also changes the optical properties of gold-black. Theoretically we showed that with conductivity, absorptance in porous gold coatings also increased. However, after certain limit of conductivity, reflectance at the interface is so large that radiations bounced back from the interface without penetrating in the layer at all. Therefore, there is an optimized value of conductivity to maintain high absorptance. This can be achieved with annealing just above room temperature. Aging may not be a drawback as far as the performance of the detector is concerned. In fact the detector performance can be boosted by a few percent prior to the operation with optimized heating. One has to be careful though, the detector sensitivity can be affected by a heat shock, as it can initiate the next cycle of grain growth or damage coating altogether. Maintaining constant temperature of the detector is extremely important.

3.5 Appendix: Polymer Infusion

Process of increasing conductivity with the aging can be avoided if aggregation of gold black nano-chains is prohibited. We attempted to achieve this with also infusing ethyl cyanoacrylate polymer chains in the gold black ‘spider web’. This process has been described with greater detail in reference [88] . In our previous work, cyanoacrylate infusion also showed improvement in mechanical stability of gold black without degrading the optical properties [89]. As shown in fumed ethyl cyanoacrylate does not form a continuous coating on top surface of gold black. It goes inside the gold black

‘spider web’ and immediately polymerizes in the presence of a weak base such as water vapor in the atmosphere. Instead of collapsing the porous gold black structure, it compresses it from all the direction.

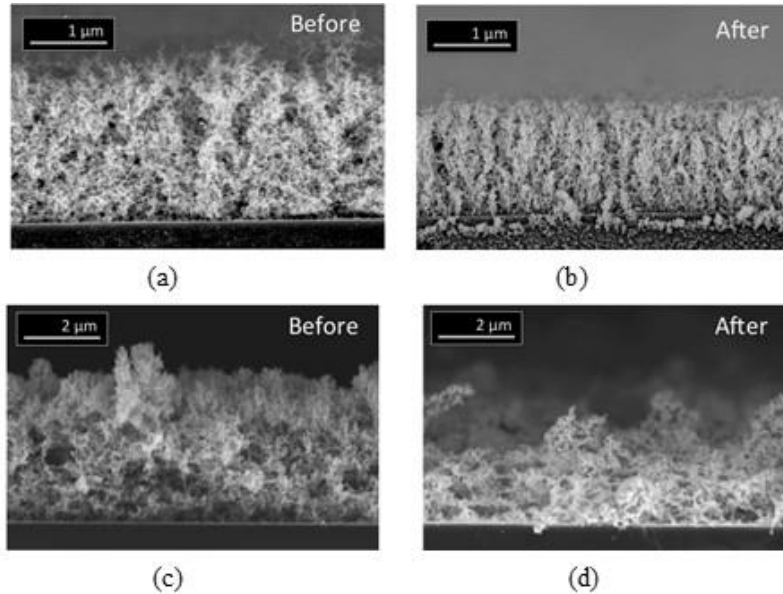


Figure 29 Gold black film cross section before (a) and after (b) 2 minutes of fuming. Similarly, (c) & (d) shows cross section before and after 20 minutes of fuming respectively.

The film undergoes by 30% of compression after 2 minutes of fuming as shown in (a, b). After 20 minutes of fuming structure undergoes compression by a factor of about 3 as shown in (c,d).

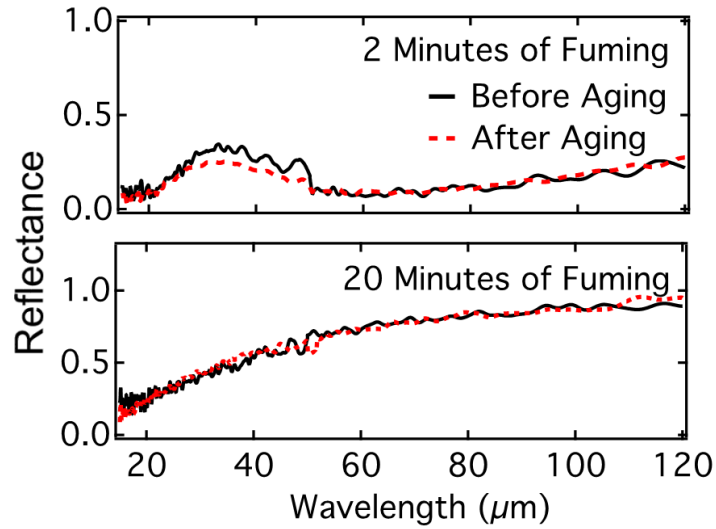


Figure 30 Spectral aging in fumed samples for 90 days at room temperature. The spectral aging in Figure 30 shows seamless overlap for fumed samples at the interval of 90 days. It could be due the polymer chains wrapping around the gold black nano chains, and almost acting as a ‘dispersant’. Polymer infusion could act as a barrier to the aggregation of grains from separate nano chains. However, larger pool of data is required to substantially conclude aging resistance in fumed samples.

CHAPTER FOUR: STENCIL LITHOGRAPHY OF GOLD BLACK

4.1 Background

In thermal IR sensors (e.g. bolometers), absorptive coatings convert IR incident power into heat. Many different absorber materials have been investigated, including thin metals, SiN films [14], and metamaterials [90]. Gold black is an absorber that has been used for many decades for IR bolometers [91], particularly for dedicated single-use applications such as space missions [68]. Application of gold black is limited due to mechanical fragility that makes patterning on sub-mm scale a challenge. The deposition process necessarily blankets large areas, so that it has usually been applied only to single element detectors [92]. In array detectors, only the sensing element should be coated to avoid thermal and electrical bridging between pixels. Although sub-mm scale patterning by conventional metal lift-off using photoresist and solvents has been reported, no post patterning data regarding structure or absorption was given [93]. Our experience has been that the slightest contact with solvents collapses the film and destroys its intended properties [19]. Despite the shortcomings, the low density (~0.02% of bulk) and correspondingly low heat capacity of gold black make it attractive for fast imaging-array applications [94], if patterning and stability limitations can be overcome.

We are reporting stencil lithography for patterning of gold black in this chapter. Typically in this method, the patterns are transferred through the shadow mask openings to the substrate or device in a single step, preferably in a non-contact mode. This attribute makes stencil lithography applicable for full wafer scale fabrication [95] even on non-conventional substrates such as, freestanding bolometer membranes [68] and polymer

surfaces [96]. Although stenciling has been widely popular for fabrication of milli- and micro-meter scale electronic circuits, recent advancements have shown that patterning of even nano scale structures with high-throughput and repeatability can be achieved [97, 98]. This method provides low cost substitute for optical and electron-beam lithography, however the blurriness around the edge (edge effect) is still a major shortcoming. The edge effect depends on source-mask, mask-substrate distances and width of the mask openings [98].

Fabrication of gold black patterns with sub-mm mask-substrate distances is discussed in this chapter. Differences in morphology were observed in comparison to blanket depositions. The patterns produced with stencil lithography were denser and more conductive than the blanket deposition. Absorption remained excellent out to at least 11 μm wavelength. Infrared imaging microscopy revealed a gradient of absorption near the pattern edges that is broader than would be inferred from the optical image. The infrared image showed sharper edges in the long-wave IR than in the mid-IR.

4.2 Patterning with Stencil Shadow Mask

The stencil shadow mask was held at sub-millimeter distances from the substrate with layers of cellophane tape (“ScotchTM”) as spacers. Such tape has poor thermal conductivity, so that the mask is radiantly heated during the deposition while the substrate remains cold. This achieves preferential deposition on the substrate through the stencil windows. Nevertheless, gold black eventually accumulates and clogs the mask apertures, so that cleaning in acetone after each use is required.

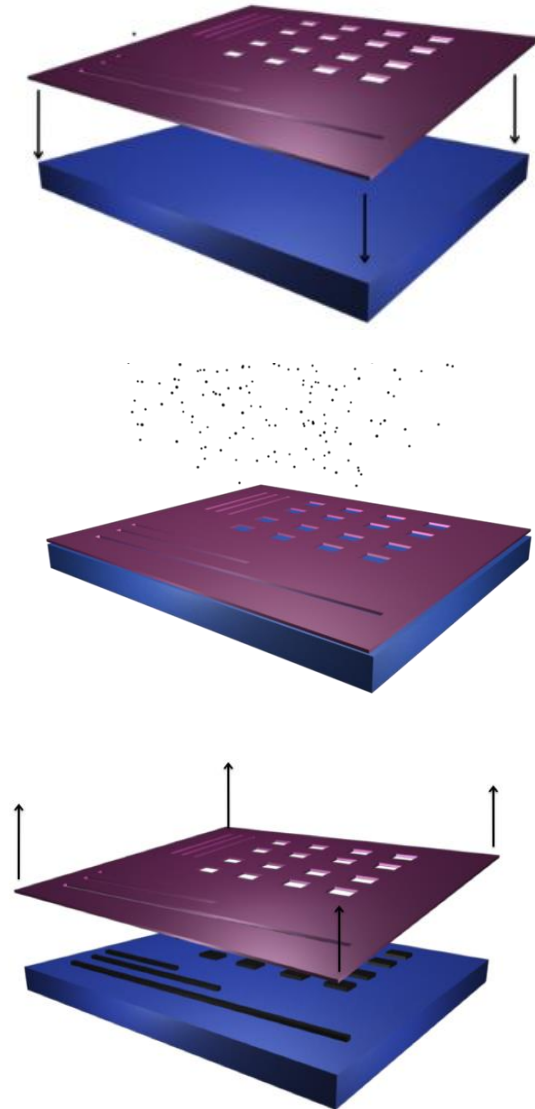


Figure 31 Schematic diagram of stencil lithography method. Alignment of shadow mask (top) is followed by deposition of gold black (middle). Then the mask is lifted leaving the gold black pattern (bottom).

For conductivity measurements, coatings were deposited between two gold electrodes of $22.5\ \mu\text{m}$ width and similar separation. A Ziess Ultra 55 scanning Electron Microscope (SEM) imaged cross sections to determine thickness, which was measured at the center of the pattern. Conductivity was obtained by dividing the slope of the I-V curve by this thickness. These were 2-point-probe measurements, so that contact resistance is present, though metal-metal contact resistance should be small.

4.3 Sub-Micron Spatial Imaging

Using a conventional FTIR Spectrometers with single pixel detector and global source, it is extremely difficult to scan the absorbance profile across the sub-mm scale gold black patterns. For e.g. in order to scan ten profile data points across the pattern with $80 \times 80 \mu\text{m}^2$ area, the aperture size (a) must be $8 \mu\text{m}$ for collecting 10 data points across each direction. Such smaller aperture provides extremely low incident power, resulting in extremely low Signal to Noise Ratio (SNR). In order to improve SNR, user is prompted to increase the aperture size, which results in low resolution of absorbance profile. Other way to improve SNR is to utilize high acquisition times (\sim hours). These trade-offs make the approach of using single pixel detector with thermal source extremely impractical for spectral characterization of sub-mm scale features. Also in single element detector approach, diffraction limited imaging is possible only if $\lambda \leq a$. For $\lambda > a$, diffraction limited imaging is not realized which results in deterioration of incident power for longer wavelengths [99].

Resolution of an optical system is defined as $d = 0.61 \lambda/\text{NA}$, where d is the minimum distance between the resolvable features and NA is Numerical Aperture. Low value of d is desired, which can be realized with higher Numerical Aperture. However, with single element detector, recorded spectrum is integration of spectra from different features. For e.g., if the pattern size is smaller than the illumination area than actual spectrum consist of signals from both the pattern and reference substrate. The localized spectral signatures are lost. In order to keep the spectral purity and generate IR mapping of different features, Focal Plane Array (FPA) of detectors must be used. In this case, the resolution of the image depends on size of the pixel. It is desired to have smaller pixel size for

higher resolution, however over sampling can result in loss of signal. This can be compensated by replacing globar with much brighter source, such as synchrotron radiations.

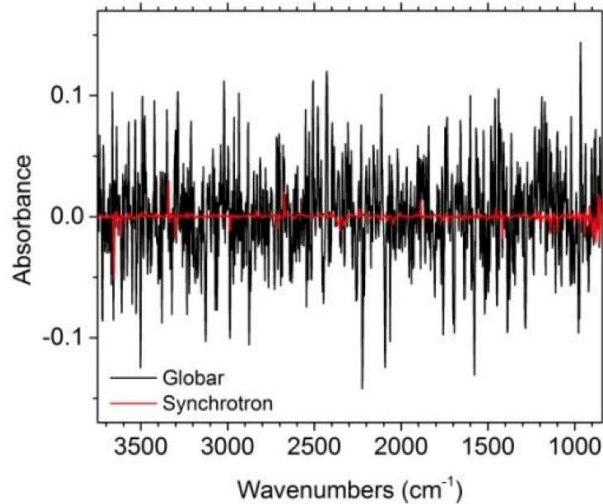


Figure 32 Signal comparison of globar and synchrotron source. Image re-printed with permission from Mehmet Yesiltas' PhD Dissertation [100].

For IR imaging micro-spectroscopy with high spatial resolution, we used the Infrared Environmental Imaging (IRENI) beam line at the Synchrotron Radiation Center, University of Wisconsin, Madison [101]. A Bruker Vertex FT-IR spectrometer with Hyperion 3000 IR microscope used multiple combined beams of the synchrotron source to provide 1000 times brightness than from a globar. A Focal Plane Array (FPA) detector allowed spectral imaging with better than 1-micron spatial sampling. The spectral resolution was 4 cm^{-1} and the spectral range was $900\text{-}3700\text{ cm}^{-1}$. For reflectance measurements, the microscope was equipped with 20X, 0.65 numerical aperture (NA) Schwarzschild objective. IRidys (Infrared Imaging & Data Analysis) program, which runs on commercial software package IGOR PRO, was used to extract spectra from different pixels [102].

Figure 33 shows the schematic of the experimental setup, which includes synchrotron source and FPA. Extremely bright synchrotron radiations are emitted from the bending magnet. The emitted radiations are then collimated in to 3×4 bundles of beam using mirror sets M1-M4, which ends up providing 1000 times more brightness than conventional globar source. In the reflectance mode, the overlapping 12 beams illuminate the $12 \times 11 \mu\text{m}^2$ area on FPA with 128×128 pixels. Image with field of view larger than illumination area is acquired by stitching multiple images together.

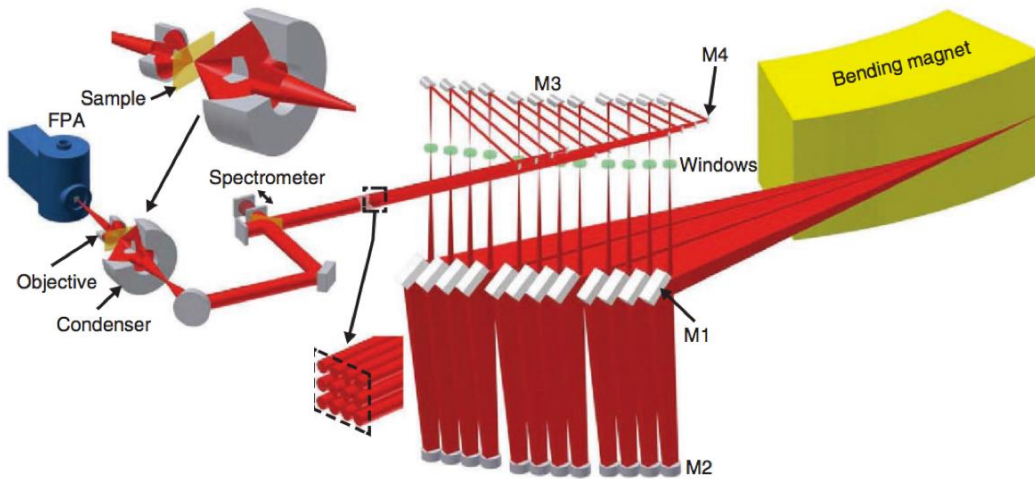


Figure 33. FTIR imaging with a multibeam synchrotron source. Reprinted with permission from Macmillan Publishers Ltd: Nature Communications [101].

We use silicon substrates that have been coated by evaporation with an optically thick layer of gold on a 10 nm thick Cr sticking layer, so that absorptance may be determined from measurement of a simple reflectance spectrum ($T = 0, A = 1 - R$).

4.4 Results & Discussion

When the height of the shadow mask is optimum, well-defined and reproducible patterns are obtained. Figure 34 presents optical microscope images of two different patterns

fabricated using circular and square shadow masks, respectively, at sub-mm mask heights above the substrate surface. All deposition parameters were similar for both patterns, except that the pattern in Figure 34 (b) is produced with nearly twice the mask-substrate separation as that in Figure 34(a). Significant differences appear in thickness, morphology, and edge definition. This coating appears thinner and its edges are fuzzier. In other words, the closer the shadow mask is to the substrate, the sharper are the edges and the thicker is the resulting pattern. The thickness of the pattern in Figure 34(a) exceeds $\sim 10\ \mu\text{m}$, which gives high far-IR absorption. However, such thick coatings are more prone to mechanical damage. The upper structure of the thick coating is blown off immediately when exposed to a stream of nitrogen gas coming out of a 4-mm internal-diameter nozzle at 70 liters/min flow rate from a distance of approximately 1 cm. The sub-structure of the coating adheres well to the Si substrate. Patterns of $\sim 5\ \mu\text{m}$ thickness, such as shown in Figure 34(b), survived the nitrogen-jet test.

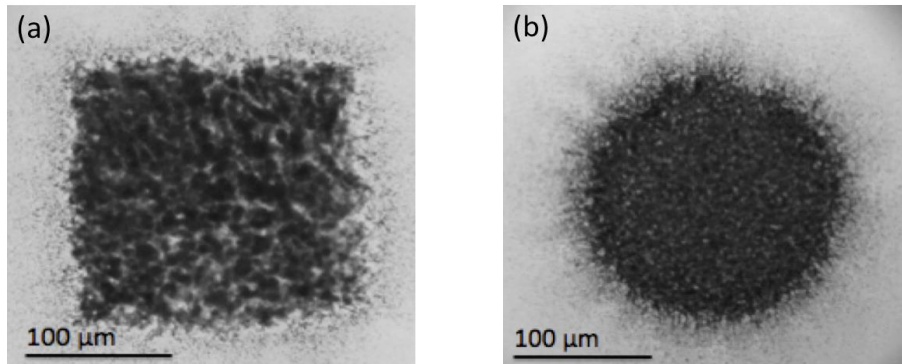


Figure 34. Optical microscope images of gold black patterns produced with shadow mask. The mask-substrate separation was twice larger for the circular pattern.

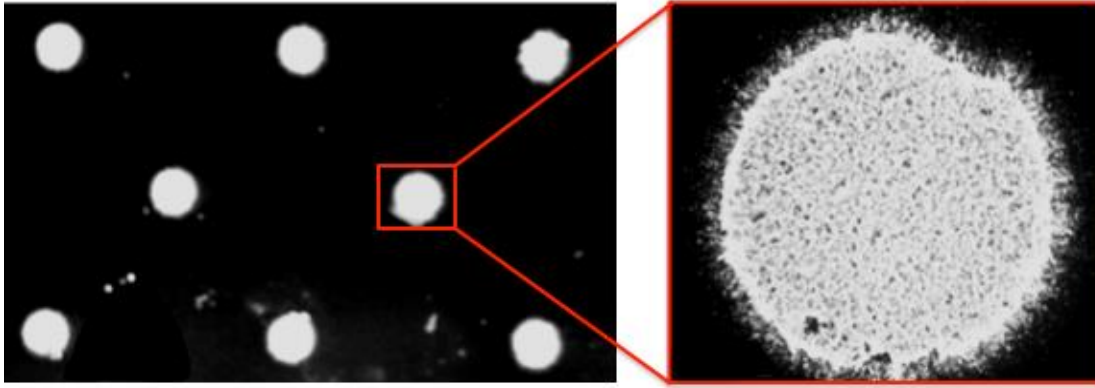


Figure 35. SEM image of thin circular gold black patterns similar to shown in Figure 27 (b). The magnified image clearly show presence of edge effect.

Figure 36 shows that typical cross-section profile of a pattern follows normal distribution. With similar deposition parameters, the thickness of the blanket deposition is found to be $\sim 3.6 \mu\text{m}$. However, the mean value of the pattern thickness produced with 0.3 mm mask distance is $\sim 1.5 \mu\text{m}$.

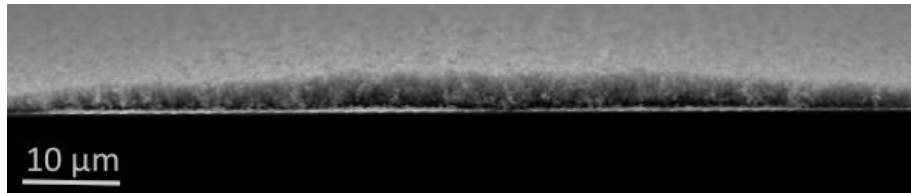


Figure 36. SEM cross-section image of pattern produced with 0.3 mm of mask-substrate height.

Figure 37 (a) presents SEM images of coatings made by blanket deposition without a mask. The average feature size exceeds that produced when a shadow mask is used (Figure 37 (b)), and these blanket depositions appear less dense. In each case, the substrate was cooled to -13 C . However, the mask shades the substrate from radiant heating, which allows the substrate to be colder than without the mask, so that cryo-pumping enhances the accumulation. Moreover, the relative warmth of the mask aperture may focus and enhance the gold-black flux through the apertures. That the patterned films are thinner but denser we attribute to the exclusion by the mask of long chains of gold black particles that link together before reaching the mask. The smaller chains that

make it through the aperture are able to pack more closely together. When thermally conducting spacers are used, the temperature differential between mask and substrate decreases, and the patterns produced are sparse and discontinuous, while deposits on the mask itself are heavy. Similarly, we expect from these experiments that the thermal conductivity and infrared absorptivity of the mask material will affect coating morphology. Additionally, we note that smaller mask openings produce pattern edges that are not as abrupt.

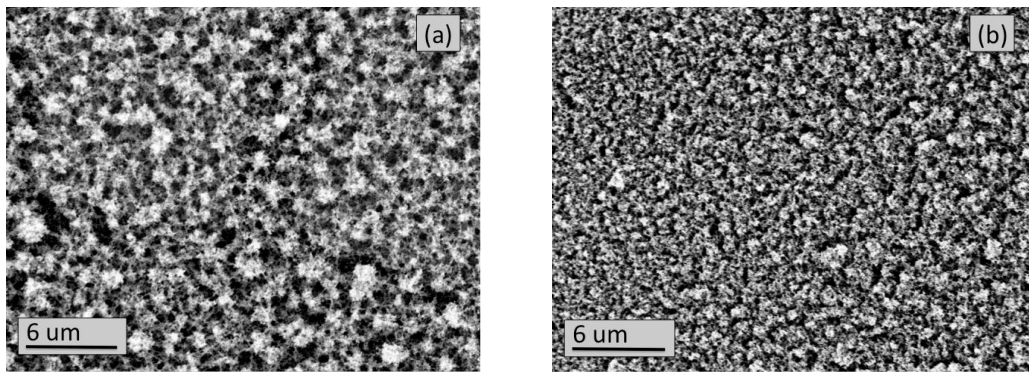


Figure 37. SEM image of gold black produced (a) without and (b) with shadow mask at height of 0.3 mm.

We utilized two-probe method to calculate conductivity of the coatings. The conductivity values were found to be $\sim 10^{-4}$ - 10^{-6} times lower compared to bulk gold. This shows that goldblack shows ohmic behavior, and its conductivity is closer to semi-metallic and semiconducting materials. Although considering the contact resistance present in two-probe method, actual values of conductivities might be slightly higher. *Nevertheless, the patterned gold black showed twice conductivity (14967 S/m) compared to the blanket deposition (7335 S/m), which is in agreement with the tighter packing observed in Figure 36 (b). Larger mask-substrate separations give lower conductivity due to reduced gold-black flux passing through the mask aperture.*

Coatings with higher conductivity are expected to have higher absorption coefficient [23]. Therefore, the higher conductivity of the patterned coatings allows them to be thinner, and hence more robust. However, it is important to note that if the density becomes too high, the film may begin to behave more close a bulk metal, for which reflection increases with conductivity. Thin patterns are particularly interesting due to their robustness. Mask height can be optimized to achieve morphology with desired density and conductivity, with the goal of keeping patterns thinner and yet more absorbing.

The spatial distribution of reflectance near the edge of a stripe pattern (Figure 38(a)) is presented in Figure 38(b). The coating thickness is comparable to that in Figure 34 (b) (Thin pattern). The dimensions of the gold black pattern are $85 \mu\text{m} \times 13 \mu\text{m}$, as determined from the optical microscope image Figure 38 (a). The color scale (online) gives the spectrally integrated reflectance over the wavenumber range $900 - 3700 \text{ cm}^{-1}$ (11.1 to 2.7 μm wavelength). The optical image shows blurred edges, which are transition regions of intermediate reflectance that are colored green in the IR image. Strongly absorbing regions of less than 5% reflectance are red, while the ~90% reflecting gold substrate surface is blue. The width of the mask aperture is $80 \mu\text{m}$, but the region of maximum absorption extends over width of only $52 \mu\text{m}$. In other words, the transition region on each side is $14 \mu\text{m}$ wide, which is not apparent in the visible-band optical image.

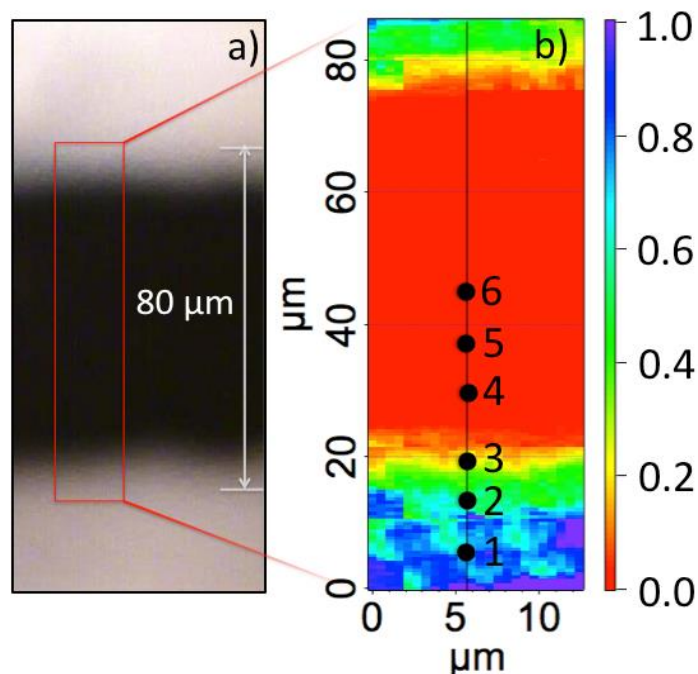


Figure 38. (a) Optical microscope image of gold black pattern. (b) Color online. Spectrally-integrated IR reflectance microscope image of the same sample. Numbered dots indicate where spectra are sampled. The color scale indicates reflectance, which is integrated over the range 970 – 3700 cm^{-1} .

Figure 39 presents reflectance spectra extracted from the six different pixels labeled in Figure 38 (b). Pixel 1 is located on the bare gold substrate and shows the expected high reflectance from the gold surface. The decrease toward higher wavenumbers can be attributed to scattering by sparse gold black strands at the very edges of the deposition. Pixel 2 and 3 are from the transition zone of intermediate reflectance and show increasing absorption. Artifacts due to atmospheric water vapor and carbon dioxide are evident in spectra from pixel 1 and 2. Spectra from pixels 4 to 6 are well within the main deposition and show strong absorptance across the spectrum. Reflectance at pixel 5 is less than 1%. At pixel 6, signal is null, resulting in flat reflectance coincident with the horizontal axis. Although such thin coatings may lack high absorptance in the far-IR [23], they do retain high absorptance out to at least 11 μm wavelength, while they are more robust than thicker coatings.

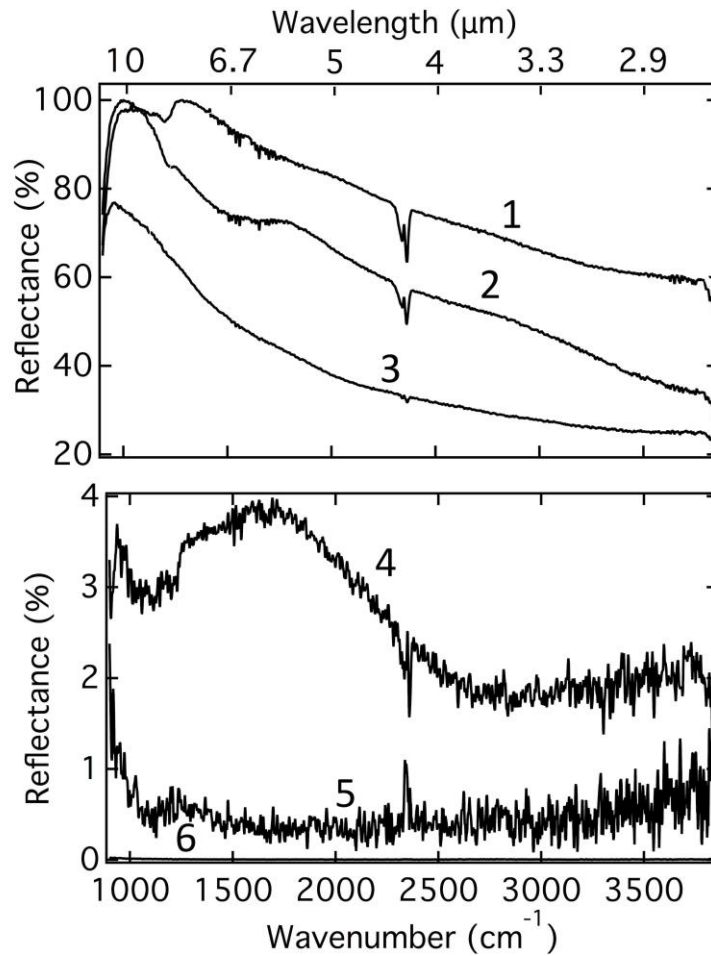


Figure 39. Reflectance spectra extracted from six different pixels numbered as in the infrared image Figure 38.

Figure 40 presents the infrared image at two different wavelengths for the same pattern in Figure 38 (a). At 2.7 μm the edges appear fuzzy with a broad transition region (yellow-green). The edges are sharper at 11.1 μm , with transition regions only $\sim 4 \mu\text{m}$ wide. This is because at longer wavelengths there is less absorption and/or scattering by the sparse particle distributions at the edges of the pattern. The mask distance from the device can be optimized to attain effective absorbing area (red), similar to that of pixel size. *Any lateral spreading between the pixels should cause negligible thermal crosstalk between pixels at long-wave-IR than at mid-IR wavelengths.* Central region in both the images

appear ‘equally’ red, which describes feature size of gold black is smaller than wavelength of 2.7 μm . It is behaving as an homogeneous medium with no scattering.

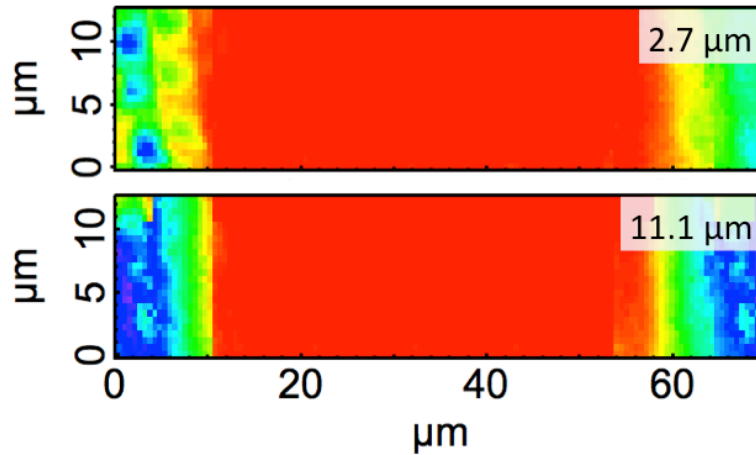


Figure 40. Infrared image of gold-black pattern at indicated wavelengths.

The width of the low-reflectance region (red) at 2.7 μm and 11.1 μm is 52 μm and 48 μm , respectively. This indicates that although the pattern edges appear indistinct at short wavelengths, they are sharper in LWIR. On the other hand, the corners of square patterns were less distinct in the LWIR, so that the patterns appeared more circular (not shown here). The 5 μm thickness appears adequate to achieve high absorptance in the long-wave IR.

4.5 Conclusion

Scanning Electron Microscopy revealed that the morphology of a gold-black pattern produced with a shadow mask is more closely packed than for blanket depositions. I-V measurements showed higher conductivity for those mask-defined patterns. The substrate-mask separation can be optimized to attain desired density and conductivity.

Results presented here suggest the possibility of preparing gold black patterns with lower thickness than for blanket depositions with similarly high absorptance in the LWIR. This may be advantageous since thinner depositions are more robust mechanically.

Synchrotron-based IR spectral imaging with sub-micron spatial resolution revealed absorbing areas significantly smaller than indicated by the mask openings and apparent optical dimensions of the patterns. The edges of the patterns are sharper at LWIR than at shorter wavelengths.

CHAPTER FIVE: PHOTOLITHOGRAPHY OF GOLD BLACK

5.1 Background

In the previous chapter, stencil lithography showed some success at patterning gold black, but stencil mask alignment was to be tedious, the masks had to be cleaned between use, and the edges of the resulting patterns were blurry. The smallest feature size achieved in our case was $\sim 80 \mu\text{m}$. In order to reduce feature size further, shadow mask height must be lowered [103]. In fact the best resolution is achieved when the mask is in contact mode with the substrate. This is not desired condition in current MEMS based micro-bolometers due to high chances of damage to the pixels. The other approach presented by Nelms et al. used laser ablation to remove undesired coating deposited between the pixels, but this expensive & slow process is unsuited to mass production[103].

The approach presented in this chapter describes method to prepare pattern of gold black using conventional photolithography. The smallest feature size achieved with this method is less than $\sim 10 \mu\text{m}$. In usual metal lift-off, a pattern is prepared by spinning photo-resist, exposing this layer to UV through a shadow mask, and developing with solvents to open patterned windows down to the substrate. Then metal is deposited over the entire wafer, which is finally submerged in solvent to remove the remaining photoresist and the metal on top of it. The metal stuck to the substrate remains. Lift off can be performed only if the metal adheres strongly to the substrate and if the metal is not attacked by the solvent. None of these conditions are satisfied by usual gold black, which is immediately washed off in the final lift-off step from all areas of the substrate.

This chapter describes the preparation of mechanically-robust, sub-millimeter scale, gold black patterns having nearly 100% absorption out to mid-infrared wavelengths. The approach is by standard photolithography and metal lift-off, which is made possible by mechanically stabilizing the gold black with an evaporated oxide coating.

5.2 Patterning with Photolithography

Figure 41 presents a schematic of the deposition process. Negative photoresist NR1500 PY was spin-coated to thickness 1 micron on silicon substrate. A mask pattern was transferred to the resist using an OAI 200 contact mask aligner. RD6 developer was used to remove the unexposed parts, leaving behind bare silicon substrate, which was further cleaned by an oxygen plasma de-scum.

The gold black was deposited at 400 mTorr N₂ pressure (close to Type 1 - Table 1). Gold wire in the amount 85 mg and of 99.9% purity was placed in a molybdenum boat. The current applied to the boat was 65 A for all depositions. At low pressures coatings are thinner and less porous, which provides more robustness compared to coatings produced at 3 Torr (Type 3 - Table 1). Subsequently, high-pressure coatings exhibited extremely low yield during the lift-off.

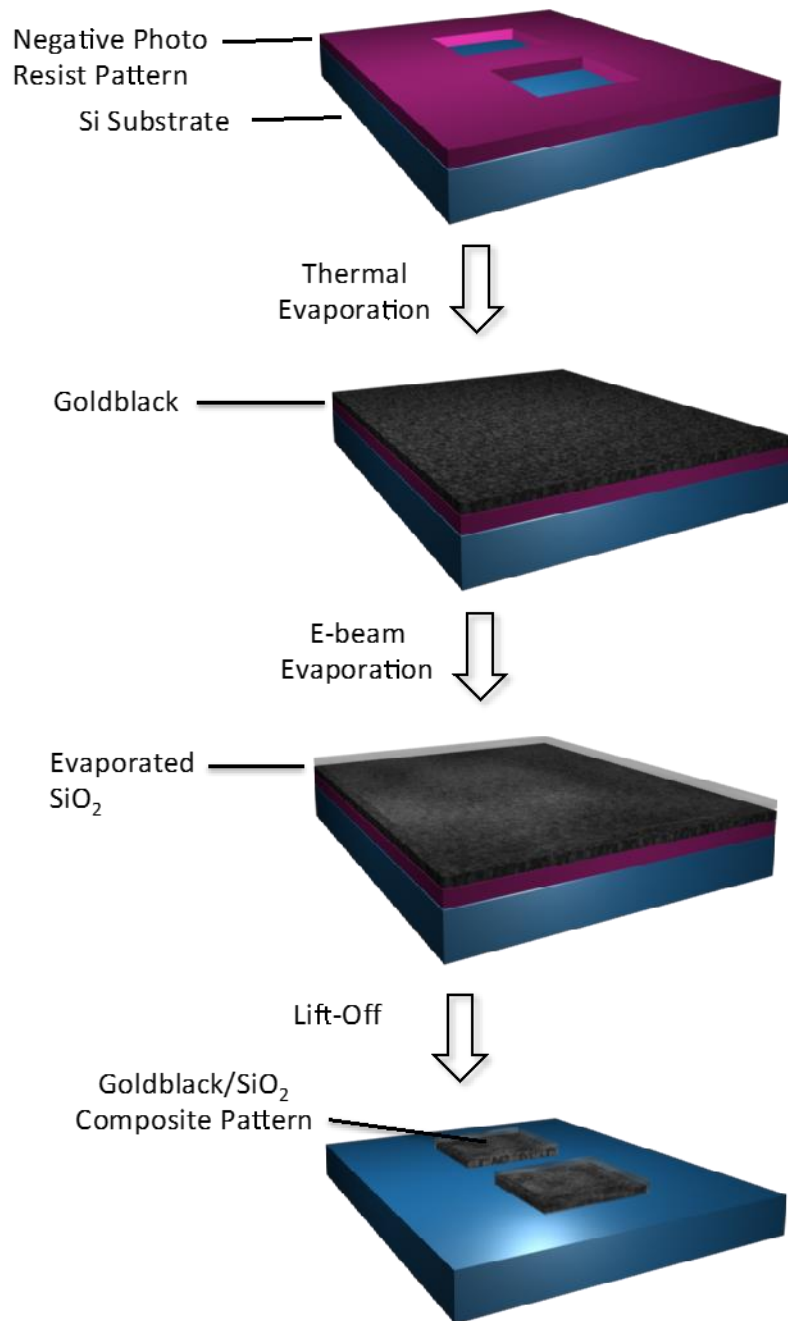
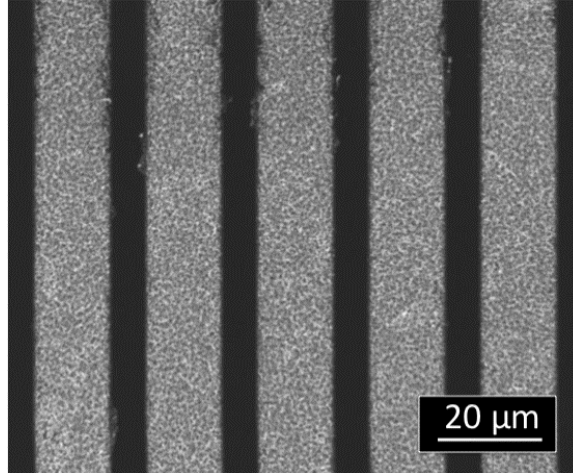


Figure 41 Schematic of processing sequence patterned gold black/SiO₂ composites
 The instability and fragility of gold black make it incompatible with PECVD oxide deposition due to the high temperatures involved. Instead, we deposited SiO₂ on the gold black sample by electron beam evaporation. The source was fused silica pellets of 99.99% purity placed in a 7 cc carbon crucible. The chamber was evacuated to 2×10^{-6}

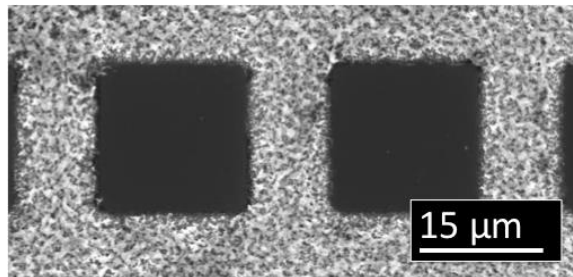
mTorr and a wide, high-frequency e-beam sweep pattern maintained a deposition rate of 2-3 nm/s. The thickness of the film and rate of deposition were continuously measured by a quartz crystal monitor (Inficon XTC). The sample was placed normal to the target boat at the optimized distance of 30 cm to keep the temperature below 60 °C. A thermocouple monitored the temperature of the substrate holder during the process. The SiO₂ film undergoes compressive stress after venting the chamber. The stress reverses to tensile direction logarithmically with time until it reaches a stable state [104]. Therefore, the substrate was kept at atmospheric pressure for more than 10 hours to allow it to reach mechanical equilibrium before absorption measurements. The oxide over-coated gold black kept in the acetone solvent for 10 seconds for lift-off.

5.3 Results & Discussion

Figure 42 presents an SEM image of a gold black-SiO₂ micro pattern (bright) on silicon substrate (dark). The thickness of the SiO₂ protection layer was optimized at 150 nm. We prepared several different patterns tens of times repeatedly. These exhibited high resistance to mechanical damage. The smallest feature size achieved close to 6 μm.



(a)



(c)

Figure 42 SEM images of photo-lithographically produced goldblack patterns over-coated with 150 nm SiO_2 on Si substrate. (a) Gratings with close to 20 micron width (b) Square lattice with sub-10 micron features.

Figure 43 presents the top view SEM images of gold black coatings before (left) and after (right) 150 nm of SiO_2 is deposited. The oxide covers and reduces the roughness of the gold black surface leaving open only the largest of the pores.

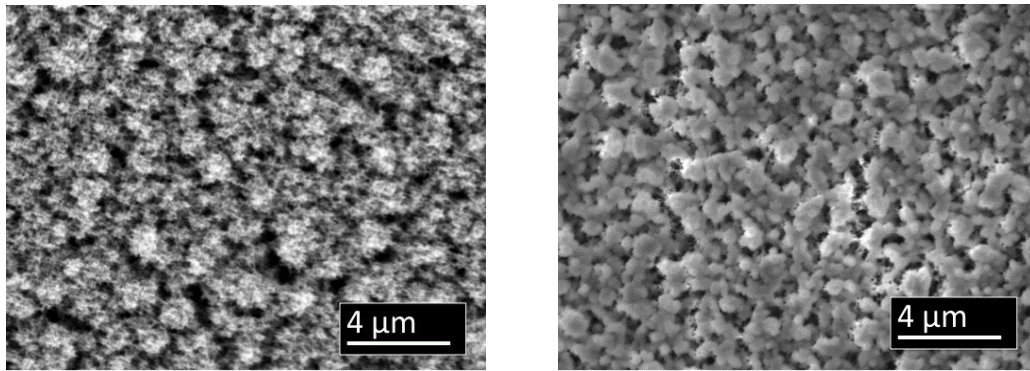


Figure 43 SEM top-view images of gold black coating before (left) and after (right) SiO₂ deposition.

Figure 44 presents SEM cross-sectional side views of the same region on the same sample, where location is confirmed by features that appear on the substrate. These images indicate that the gold black retains its original 3.5 μm thickness after the oxide over-coating. Figure 44 also gives the sheet resistance values for this sample, showing little change with oxide deposition. If the oxide were to compress the film, interconnectedness would increase, lowering the resistance and potentially changing the IR absorption. *Therefore, we can conclude that the SiO₂ settles lightly on the gold black without compressing it or otherwise altering the structure.*

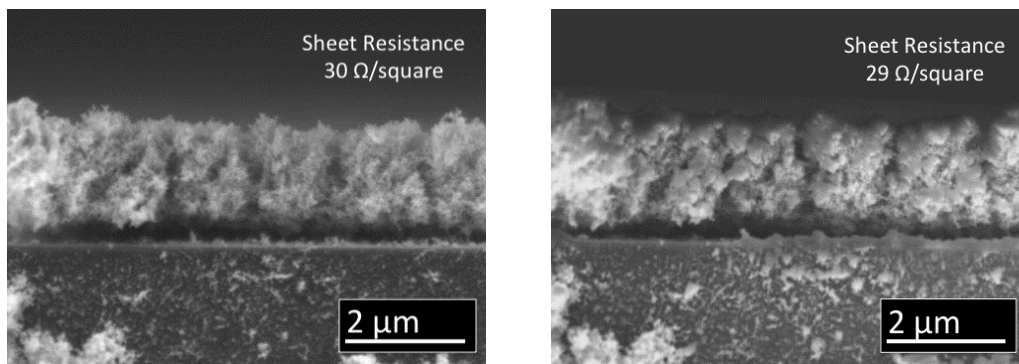


Figure 44 Cross-sectional side view SEM images of gold black coating before (left) and after (right) SiO₂ deposition.

Figure 45 (a) & (b) present cross sectional SEM images of the same region on the same *unprotected* gold black sample before and after immersion in acetone for 10 seconds.

The average thickness of gold black coating was $4.79\ \mu\text{m}$ before wetting, which drastically collapsed the unprotected film to less than $500\ \text{nm}$. Some portion of the coating completely came off from the substrate. Figure 45 (c) & (d) present cross sectional SEM images of the same region on the same oxide-*protected* gold black sample. In contrast to the unprotected case, 10 sec immersion *caused only a partial collapse*, from 8.79 to $2.44\ \mu\text{m}$.

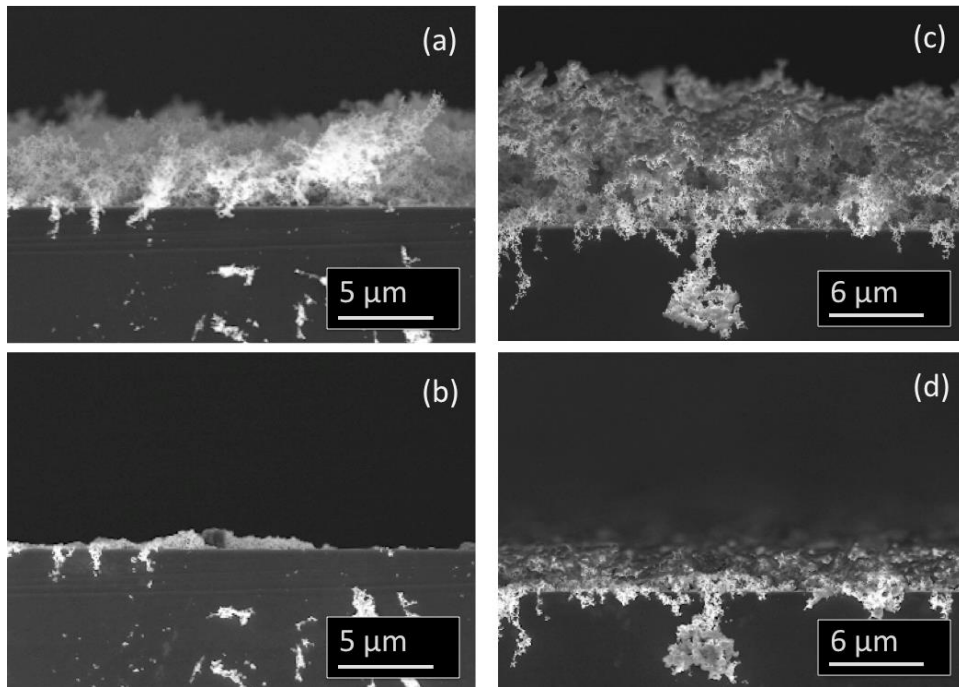


Figure 45 Cross-sectional SEM images of unprotected gold black before (a) and after (b) wetting in Acetone. Oxide over-coated gold black before (c) and after (d) wetting in acetone.

Just 50 nm of oxide enables lift-off patterning, but 150 nm is necessary to preserve significant absorption in the 3-5 μm wavelength atmospheric window. To eliminate the pores, $500\ \text{nm}$ of oxide is needed, but then the lift-off is not clean. Such films also crack after venting the chamber, presumably due to compressive stress. Ultrasonic agitation cannot be used to expedite lift-off because it damages the films.

Figure 46 shows the SEM top-view image of similar oxide over-coated coating as shown in Figure 43 (right), *but after the lift-off in acetone solvent*. Obviously, the porosity of gold black is reduced significantly after the collapse in acetone. Comparing this image with Figure 43 (right), *we can observe the increased the roughness of the top oxide surface*. Akimov *et al.* have demonstrated that due to negligible absorption in dielectric particles, they display higher scattering cross-section compared to metal nano particles [105]. Large dielectric particles (\sim micron) can also efficiently scatter wavelengths in infrared spectrum.

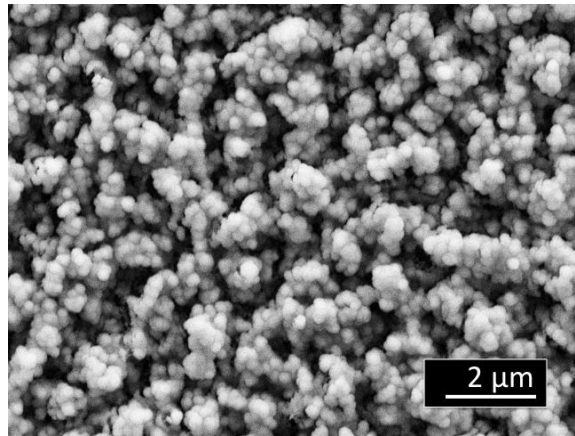


Figure 46 SEM top-view image of oxide over-coated gold black coating after lift-off treatment in acetone solvent for 10 seconds.

The absorptance of oxide-over coated gold black can be calculated by $A = 1 - R - T$, on the assumption of negligible scattering. It is important to test if the assumption is true, even after collapsing of the structure. Therefore, diffused reflectance (scattering) is measured at different angles using a hemi-spherical mirror for signal collection in detector. From Figure 47, it is evident that scattering at different angles, ranging from 7 to 60 degree is negligible (less than 1%) in mid-LWIR spectrum. With 150-200 nm of oxide over-coating, collapsed gold black still appear black with naked eyes, therefore scattering in IR was not expected.

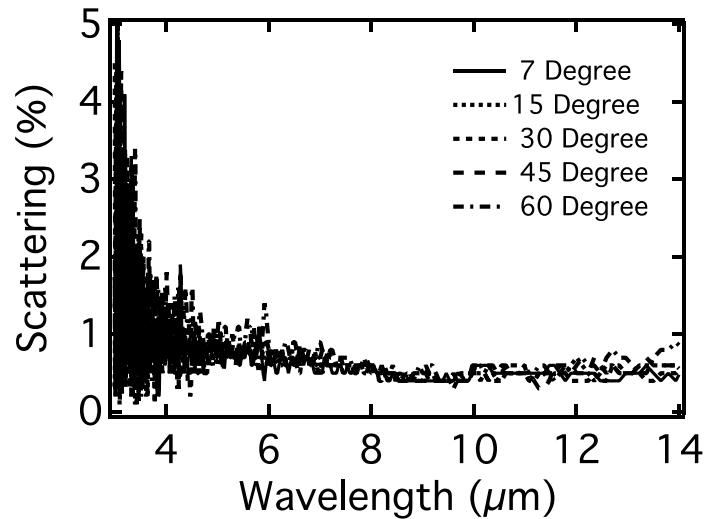


Figure 47 Angle dependent scattering from similar coating shown in Figure 46

Figure 48 (top) presents the measured absorbance spectra of gold black in different conditions in a following sequence; pure gold black is evaporated on a double-sided polished silicon substrate. SiO_2 is evaporated as a protection layer on top of gold black, which is followed by acetone treatment causing the collapse of the structure in the final stage.

As expected, pure gold black is nearly perfect absorber in 2-12 μm wavelength range. Interestingly, after evaporating SiO_2 protection layer on top, absorbance remains unaffected. However, immersion in acetone for 10 seconds, as occurs during lift-off, decreases the long wave absorbance. Moreover, this treatment caused a decrease in sheet resistance from 30 to 8 Ω/square . *The transmittance was found to be null from collapsed structure.* The reduced long-wave absorbance (Fig. 5) is attributed to only increasing reflectance at higher optical density. *Immersion of unprotected gold black for even 1 second would completely destroy it. Though oxide gives considerable protection, acetone apparently can still pass through the largest pores, causing some morphological change.*

Figure 48 (bottom) presents the calculated absorptance spectra of similar three-layer structure in different previously mentioned conditions. Absorptance of reproduced 13 μm thick gold black layer using Bergman Formalism (CHAPTER TWO: OPTICAL PROPERTIES) is calculated on Si substrate ($n = 3.41$, $k = 0$). As expected, reproduced 'pure' gold black layer on Si substrate gives similar high absorptance to that of experiment. Gold black-SiO₂ composite is reproduced by adding 150 nm of SiO₂ layer, calculated using dielectric function model proposed by W.Theiss in SCOUT program.

Interestingly, when 150 nm of bulk SiO₂ layer is added on top of reproduced gold black, we observe a dip in the absorptance at $\sim 9.3 \mu\text{m}$ wavelength (not shown here). *The dip in the absorptance was not observed in experiment, since SiO₂ protection layer on top of gold black is not a bulk film but an effective medium of air (or vacuum) and SiO₂ particles as observed in Figure 43 (right). Therefore, rest of SiO₂ particles must have penetrated inside the porous gold black forming gold black-SiO₂ composite.* Hence, treating SiO₂ as a Bruggeman medium with 25% volume fraction reproduces Goldblack-SiO₂ composite behaving very close to the experiments. After acetone treatment the calculated spectrum of collapsed gold black-SiO₂ composite show sharp absorption band at $\sim 9.6 \mu\text{m}$ wavelength, compared to that of observed in the experiment at $\sim 9.4 \mu\text{m}$ wavelength. The shift in the absorption peak and the broadening in experimental spectra may be due to SiO₂ deposition conditions as well as low-percolation strength in comparison with bulk SiO₂.

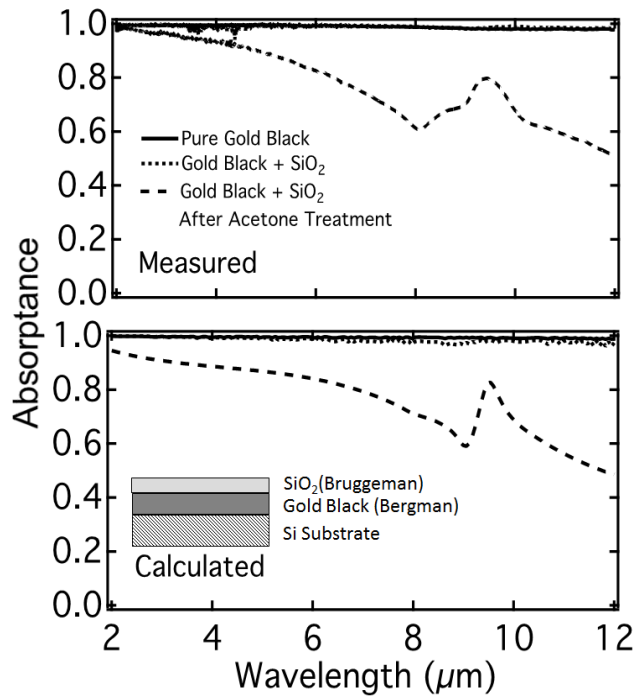


Figure 48 Absorbance spectra for gold black with 150 nm of SiO₂ over-coating (left) vis-NIR (right) mid- to long-wave IR.

Table 3 shows the fitting parameters for reproducing oxide over-coated gold black. Based on the experimental results with other coatings, the initial thickness of gold black is fitted as 13 μm with 2.5 % volume fraction. After the collapse, thickness and volume fraction of gold black are fitted as 3 μm and 10% respectively. Table 3 also suggests that only ~ 25% of e-beam evaporated SiO₂ rests on the top surface initially. However, after the collapse this volume fraction jumps to ~ 75 %. *Although, SiO₂ particles are also inside the gold-air matrix, calculated result suggests that we can get away with only considering two-layer stacking to reproduce the absorbance with reasonable accuracy.* The fitted permittivities of SiO₂ and gold black in different conditions are also plotted in Figure 49. Permittivities of gold black show more bulk like behavior after the collapse (see Figure 3).

Table 3 Fitting parameters for calculating absorptance spectra of oxide over coated gold black in Figure 48. Here, d is the thickness, f is the volume fraction, g_o is the percolation strength and α is the loss factor in Bergman Formalism.

Fitting Parameters	Pure gold black <i>before</i> collapse (Bergman-1)	SiO ₂ <i>before</i> collapse (Bruggeman-1)	Pure gold black <i>after</i> collapse (Bergman-2)	SiO ₂ <i>after</i> collapse (Bruggeman-2)
d (μm)	13	0.150	3	0.150
f (%)	2.5	25	10	75
g_o	0.05	NA	0.02	NA
α	27	NA	1	NA

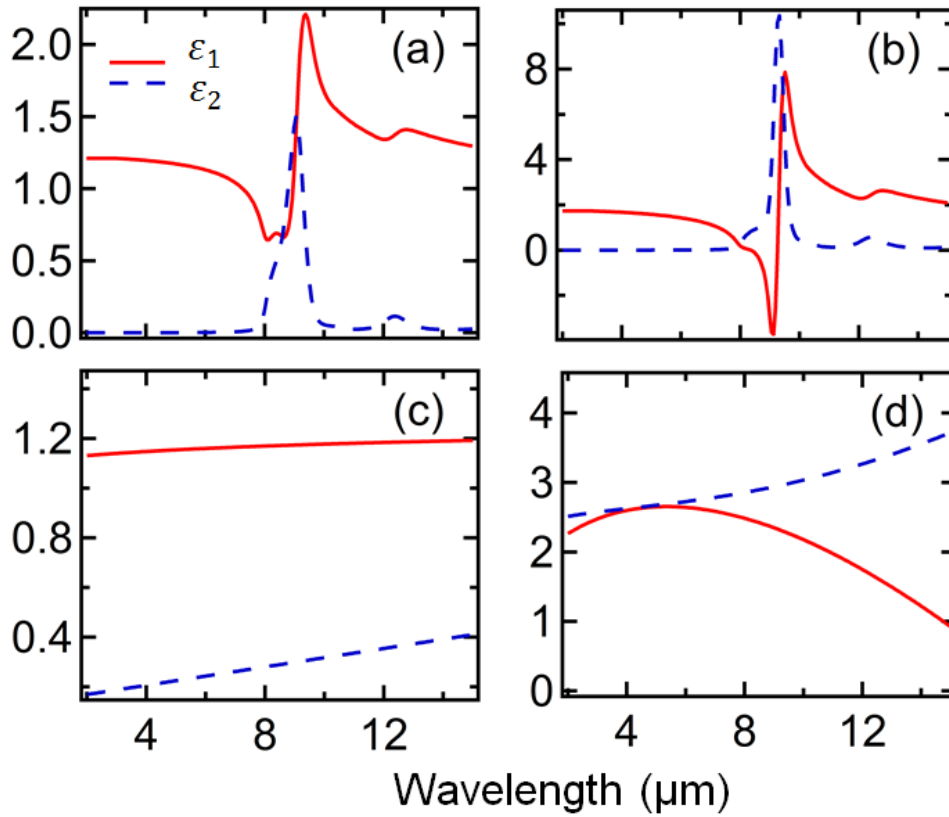


Figure 49 Calculated real (ϵ_1) and imaginary permittivity (ϵ_2) of SiO₂ (a,b) & gold black (c,d) before and after collapsing of the structure respectively. SiO₂ and gold black (ϵ_1 , ϵ_2) value are generated using Bruggeman and Bergman Formalism to fit the experimentally deposited gold black-SiO₂ composite. Bulk layer of SiO₂ is reproduced using dielectric function model proposed by W.Theiss in SCOUT Program.

Table 3 shows slightly decreased percolation strength (g_o) after the collapse of the structure. This is counter-intuitive since network must be more closely packed in a smaller space after the collapse. In this case, low percolation strength is counterweighed

by the low loss factor (α), i.e. if one tries to treat the collapsed condition similar to the pure gold black with high loss factor and low percolation strength, the calculated absorptance spectrum does not match the experiment. Therefore after the collapse, rather than considering a low density medium with high percolation, Bergman Formalism ‘forces’ one to look at the collapsed medium differently as a bulk medium with very high density of pores. This indicates electrons are able to transport more freely without much interruption due to reduced surface scattering. The increased conductivity is reflected in spectral density of the collapsed gold black with much higher peak at $N \approx 0$. *Calculated absorptance of goldblack-SiO₂ composite can be useful for modeling the optical response of cavity utilizing this coating.* This is elaborated in Chapter Six.

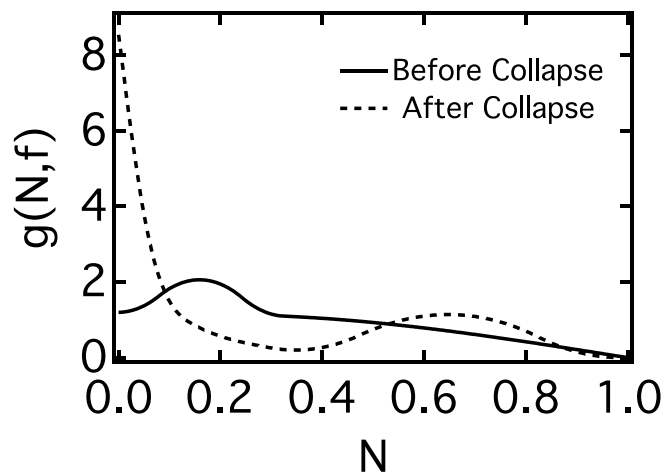


Figure 50 Bergman spectral densities of gold black from Table 3 are calculated using interpretation in [55].

Figure 51 (left) presents an optical microscope image of the region studied by the synchrotron-based IR micro-spectroscopy (the method explained in ‘4.3 Sub-Micron Spatial Imaging’). The dark region is oxide-protected gold black and the bright region is bare gold substrate. The square in Figure 51 (left) indicates the region of the IR image plotted in Figure 51 (right), which is an integrated infrared image in reflectance mode with the scan area of $\sim 38 \times 43 \mu\text{m}^2$. This infrared image (right) is a mosaic of 4×3 tiles,

each having $\sim 12 \times 11 \mu\text{m}^2$ area. These tiles are collected one by one, and combined together by the software “OPUS”. There is a small but insignificant bias artifact in the color scale for 2 of the consecutive tiles. The color scale gives the reflectance values, such that the gold black region appears red (high absorptance) and gold substrate appears blue (high reflectance).

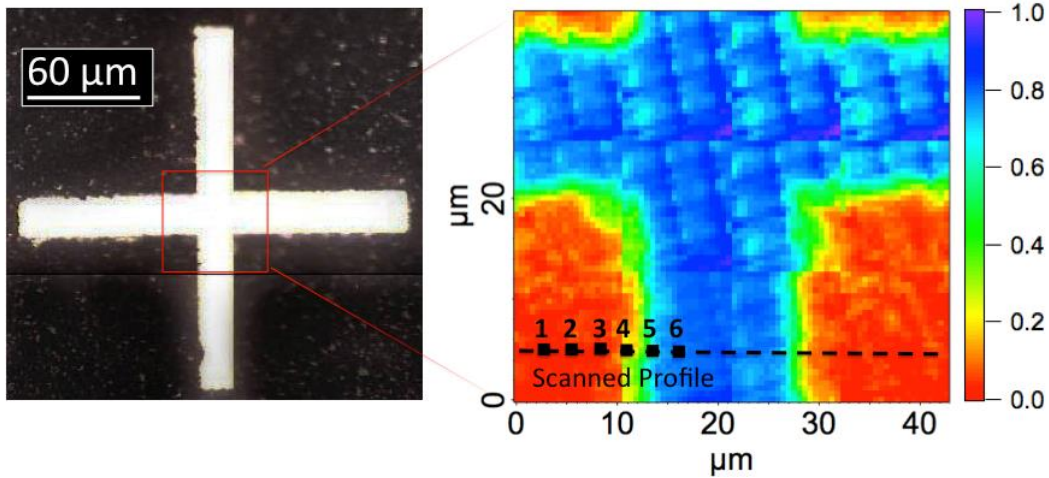


Figure 51 (left) Optical image of photo lithographically patterned gold black with 150 nm of SiO_2 thick protection layer (dark) on gold substrate (bright). (Right) Integrated infrared reflectance of gold black pattern (900 to 3700 cm^{-1}). The infrared image is a mosaic formed by stitching 4×3 hyper-spectral tiles

Figure 52 presents reflectance spectra extracted from the six different pixels indicated in Figure 51 (right). *The spectra for pixels 1, 2 and 3 are located on the gold black and show less than 10% average reflectance from 3 to 5 μm wavelength. The reflectance dip at 9.4 μm wavelength is due to the SiO_2 absorption band, which brings down reflectance to the average value of less than $\sim 30\%$ in 8 to 11 μm wavelength. This suggests, the average absorptance achieved with gold black patterns in 8 to 11 μm wavelength is slightly more $\sim 70\%$, which is much lower than unity absorptance gold black blanket coatings are capable of achieving. Interestingly, this absorption is much higher than other absorber layers such as a micron thick SiN_x and thin film metals exhibited [94].*

Pixels 4 and 5, which lay in the intermediate reflectance region show higher overall reflectance and a weaker oxide band, showing that the oxide thickness tapered off in this region. Pixel 6 is located on the bare gold-coated substrate and shows the expected 100% reflectance from the gold surface.

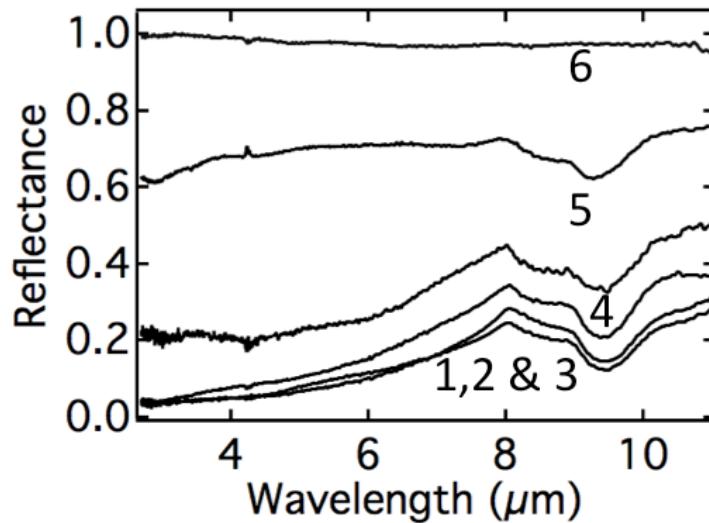


Figure 52 Reflectance spectra extracted from six different pixels shown in Figure 51 (right). The cross pattern in Figure 51 consist of two perpendicular bars of visible width 20 μm . The reflectance across the line in Figure 51 (right) is plotted in the graph Figure 53. The FWHM of this curve is smaller at 15.7 μm than the visible width. This indicates an edge effect, possibly due to greater access for the solvent to the gold-black at the edges of the oxide protection layer. The gradient region of intermediate reflectance in Figure 51 (right) is represented by green region and it extends over $\sim 2\text{-}3 \mu\text{m}$ distance. This result suggests that the smallest pattern that can retain 100% absorption at its center will be $\sim 10 \mu\text{m}$.

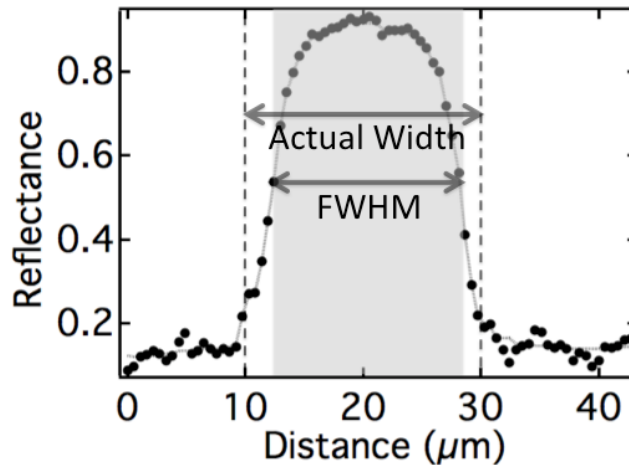


Figure 53. Reflectance line profile across a nominally 20 micron wide oxide-protected gold-black pattern showing decreased absorption at its edges. The dots represent the actual data points and the grey line is obtained from smoothing the data using Savitzky-Golay algorithm as a guide to the eye to calculate FWHM.

Uniform optical response is highly desirable for MEMS devices to qualify up to industrial standards [92]. Figure 54 (c) represents the data on spatial uniformity in reflectance with in the oxide-coated gold-black region and away from its edge. Reflectance values are plotted at 3, 5 and 8 and 9.4 μm wavelengths over 42 μm distance along the scanned profile on the sample. The average reflectance of the gold black pattern at 3 and 5 μm wavelength is 3.3% and 6.6% with negligible standard deviation of 1.4% and 2.2% respectively. The objective lens (20X, 0.65 NA) of the microscope allows to image roughly $12 \times 11 \mu\text{m}^2$ area in a single scan. Total 12 images are stitched together to provide information for desired wide field of view. The juncture between the images also add artifacts at the juncture causing spike in the data. The actual standard deviation must be even lower. We can comfortably conclude that reflectance is fairly uniform in 3 to 5 μm wavelength range with $< 2\%$ of average fluctuation.

The reflectance at 9.4 μm wavelength is lower compare to 8 μm , due to SiO_2 absorption band. In fact, only SiO_2 with 150 nm thickness does not absorb 90%. In this case absorption from SiO_2 coupling with gold black-leads to much higher absorptance. This

can be beneficial for detectors operating in 8-14 μm wavelength window. The infrared image at 9.4 μm shown in Figure 54 (c) subset is mapping of SiO_2 on gold black and it can be seen that oxide is also tapered off during lift off (just like gold black) which appears yellow followed by green color towards the edge.

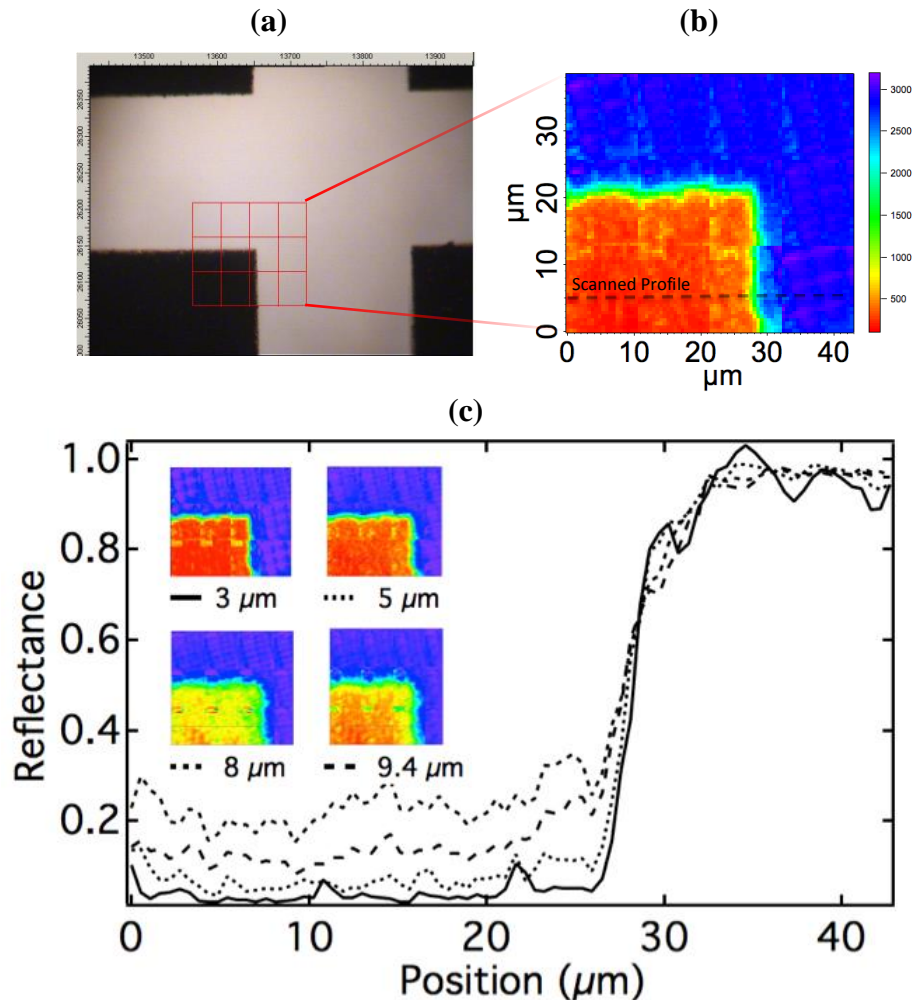


Figure 54 (a) optical image of gold black pattern and (b) Integrated infrared image ($900\text{-}3700\text{ cm}^{-1}$) of the region shown in the optical image. (c) Scanned reflectance profile and infrared mapping (inset) at 3,5,8 & 9.4 μm wavelengths

5.4 Conclusion

Patterning of oxide-hardened gold black with standard photolithography and metal lift-off is reported in this chapter. The minimum pattern length-scale achieved was less than 10 μm , which is significantly smaller than what we could achieve with stencil

lithography. In contrast to stenciling, photo-lithographically prepared patterns exhibited sharp edges with only 2-3 μm of lateral spreading. The patterns retain more than 90% absorption in the mid-IR (3-5 μm) and $\sim 70\%$ absorptance in LWIR (8-11 μm).

Although, stencil lithography offers much higher absorptance, photolithography is far more promising due to capability of achieving smaller length scales with sharp edges and compatibility with roll-to-roll fabrication.

CHAPTER SIX: DETECTOR WITH GOLD BLACK COATED PIXELS

6.1 Background

The *preliminary results* on effects of gold black coating on the performance on set of resistive bolometer pixels are presented in this chapter. Arrays of linear bolometers were obtained from Orlando FL based Plasmonics, Inc., which were designed to function as a profile sensor with a certain modulus bias [106]. The measurements of SNR for number of gold black-coated bolometer pixels are reported in this chapter.

Root Mean Square solution of heat flow equation in the form of ΔT provides the temperature change of VO_x-Au membrane with certain incident power (p_i) from the black body source. ΔT is also directly correlated with absorptance (A) on the membrane;

$$\Delta T = \frac{kAp_i}{G\sqrt{1 + \omega^2\tau^2}} \quad (6.1)$$

Here, ω is the chopping frequency, τ is the thermal time constant and. It represents the lag between the voltage signal to appear on the reading device after the pixel is exposed to the radiations, and defined as the ratio of heat capacity (C) and conductance (G).

Conductance through the arm is defined as the following;

$$G = \frac{2g_{NiCr}tw}{l} \quad (6.2)$$

The change in temperature reflects in output voltage signal through Temperature Coefficient of Resistance (α) of the VO_x-Au membrane. Output signal can be enhanced with biasing voltage, but large biasing will also cause Joule heating. For this particular

device, Smith et al. showed negligible Joule heating effect on output signal for biasing up to ~ 1 V [107];

$$dV_{out} = \frac{V_B \alpha A p_i}{4G \sqrt{1 + \omega^2 \tau^2}} \quad (6.2)$$

Voltage responsivity is defined as ratio of output voltage signal to the incident power.

$$R_V = \frac{dV_{out}}{p_i} \quad (6.3)$$

There are also three major noise sources that can hamper the device performance. The Johnson noise, photon noise, and phonon noise. Using high chopping frequency (85 Hz) allowed us to minimize 1/f noise.

Johnson noise occurs due to thermal fluctuations of charge carriers inside the VO_x-Au membrane at a particular temperature. This noise exists, regardless of any external voltage applied, i.e. if voltage is measured across the pixel (resistor), the value of voltage is not static null. In fact it fluctuates above and below zero with very minute amplitude (\sim nV or μ V). This may be neglected in daily life applications, but when output signal is in μ V range (which is the case here), quantifying this noise is very important. Johnson noise is proportional to the resistance and frequency bandwidth at a specific temperature;

$$\delta V_J = \sqrt{4K_B TRB} \quad (6.4)$$

K_B is the Boltzmann constant and B is frequency bandwidth.

Photon noise is limits the detector performance because of quasi-random influx of photons generated from the black body source. Photon fluctuations are very well explained in fundamental thermodynamics through mean square fluctuation in number of

particles in a particular mode of Bose-Einstein gas [108]. In our case, the detector is vacuum-sealed. There is no heat loss from through convection. The mean square deviation from the mean of the radiant power from the source in optical frequency interval $\nu d\nu$ is given by;

$$\overline{\delta P^2}_{Source} = \frac{A_{det} B}{c^2} \int_{\nu_1}^{\nu_2} \int_0^{2\pi} \int_0^{2\pi} 2h\nu^4 \frac{\exp(h\nu / K_B T_{source})}{(\exp(h\nu / K_B T_{source}) - 1)^2} \varepsilon(\nu, \theta, \varphi) \sin \theta d\theta d\varphi d\nu \quad (6.5)$$

Mean square power fluctuations are dependent on optical frequency range of the detector. Here, A_{det} is the area of the detector, T_{source} is the temperature of source. Here, we assume the emission to be hemispherical from the origin. There will also be contribution to the random fluctuations in the power emitted by the pixel at temperature T_{det} . In this case, emissivity $\varepsilon(\nu, \theta, \Phi)$ will be equivalent to absorptance $A(\nu, \theta, \Phi)$ of the pixel. By this argument, the total root mean square power in the frequency bandwidth B is square root of summation over both of these mean square fluctuations;

$$\left(\overline{\delta P^2}_{photon} \right)^{1/2} = \sqrt{\overline{\delta P^2}_{source} + \overline{\delta P^2}_{detector}} \quad (6.6)$$

The total photon noise in volts is calculated as following;

$$\delta V_{photon} = \frac{\sqrt{\overline{\delta P^2}_{photon}}}{A} R_V \quad (6.7)$$

Phonon noise is mainly due to conduction of heat from the membrane to the substrate through the NiCr arms. In Volts unit, it is defined as;

$$\delta V_{phonon} = 2T_{det} \sqrt{GK_B B} \times R_V \quad (6.8)$$

Noise Equivalent Power (NEP) is equivalent to the amount of power incident on the pixel area for which the signal output matches the root mean square of the noise output.

NEP in terms of noise and responsivity can also be expressed as;

$$NEP_{total} = \frac{\sqrt{\delta V^2_j + \delta V^2_{ph} + \delta V^2_{phonon}}}{R_V} \quad (6.9)$$

The detectivity (D^*) of the system in a specified bandwidth can be calculated from NEP.

$$D^* = \frac{\sqrt{A_{det}} \sqrt{B}}{NEP_{Total}} \quad (6.10)$$

Here, A_{det} is the detector area. Detectivity is the main parameter to characterize the IR sensors. Since the detectivity is heavily dependent more on geometry of device rather than absorptance mechanism. We shall discuss only output signal and noise as characterization parameters.

6.2 Design & Processing

The bolometer array is designed and fabricated by Smith et al. and fabrication details are available in reference [106]. The basic schematic of the bolometer design is shown in Figure 55. The bolometer membrane (temperature sensing material) is a VO_x -Au thin film. Vanadium oxide material is particularly exciting for temperature sensing due to high Temperature Coefficient of Resistance (TCR) around 2 - 3%/°K [109]. Crystalline VO_2 and V_2O_5 films have shown higher TCR (~ 4%/°K) but they are difficult to fabricate. Hence, the amorphous poly-crystalline vanadium oxide (VO_x) is co-sputtered with gold in presence of oxygen. High resistivity of poly-crystalline VO_x film is overcome by including optimized amount of gold particles in the VO_x matrix. Improved conductivity helps in lowering the Johnson noise without degrading high TCR. VO_x -Au film is sandwiched between two SiO_2 thin films for protection. Importantly, SiO_2 coating on top of the VO_x membrane provides the necessary electrical insulation from conductive gold black and also protects the membrane during the dry etch. The structure is built on

polyimide sacrificial layer of $\sim 2.5 \mu\text{m}$ thickness. Nichrome (80/20 Nickel Chrome) structural legs (via) provide thermal insulation from the substrate and but also the required electrical connectivity between the $\text{VO}_x\text{-Au}$ film and Read out Integrated Circuit (ROIC). Figure 56 shows the front SEM (a) and optical (b) images of pixels coated with gold black-SiO₂ composite.

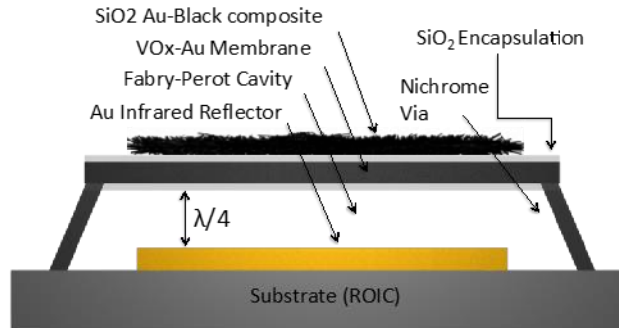


Figure 55 Cross-sectional design of gold black coated resistive bolometer pixel with optical resonant cavity. Re-drawn from information based on reference [106].

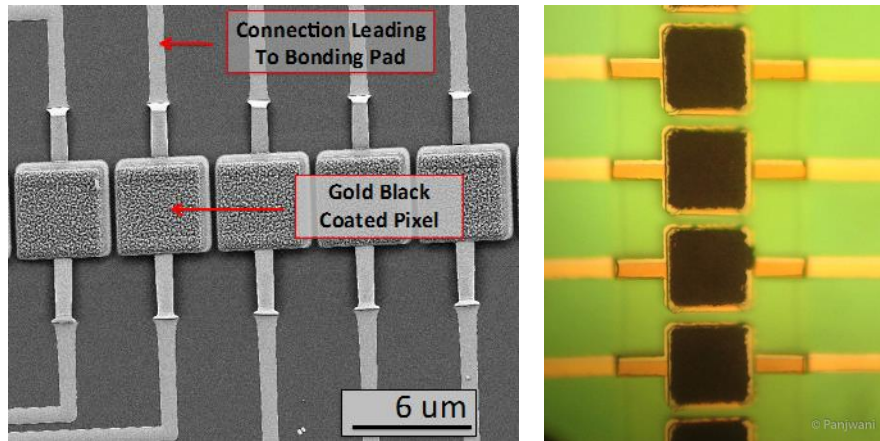


Figure 56 SEM (a) & optical (b) images of linear array of gold black coated bolometer pixels .

The polyimide sacrificial layer is dry-etched in Oxygen plasma ($\sim 600 \text{ mTorr}$) *after* patterning of gold black on the membrane. Heat during plasma etch process can easily cause the collapse in the gold black, to avoid that local temperature must be low during the etching process. Our experience with gold black during aging effect studies suggest that up to $100 \text{ }^\circ\text{C}$ there is minimum damage afflicted to structural & absorptance

properties of the coating. Activated grain growth at elevated temperatures, can result in more conductive gold black layer after the completion of dry-etch. Aging effect studies suggest that improved conductivity should improve the conductivity further after dry etch is performed.

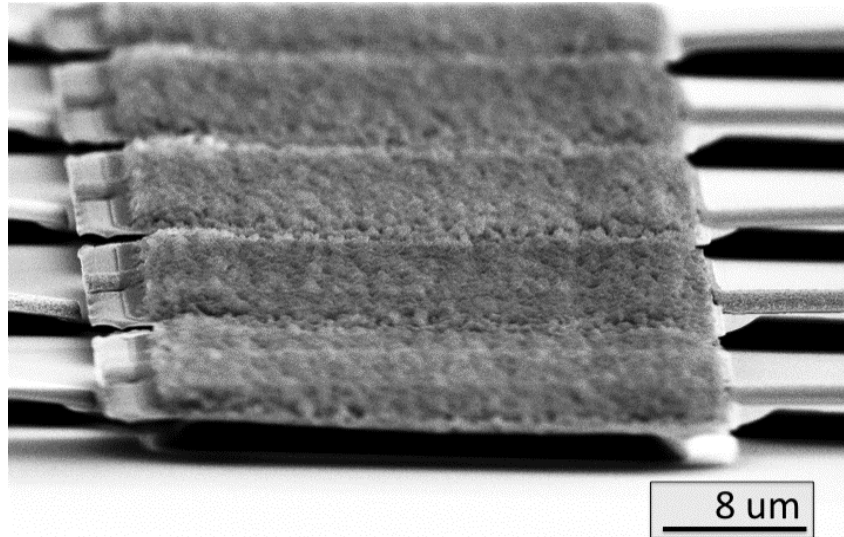


Figure 57 SEM image of gold black coated free standing pixels after ashing in plasma.

The Sacrificial layer was etched in a low concentration and non-directional oxygen plasma for a couple of hours. Oxide hardened *gold black survives the etching process successfully and maintains the absorptance properties*. The complete removal of polyamide sacrificial layer vacates the cavity of $2.5 \mu\text{m}$. This cavity followed by the gold reflector thin film at the bottom provides the resonant absorption at $\sim 10 \mu\text{m}$ wavelength.

6.3 Initial Results

Table 4 shows the measured output signal and noise. Performance parameters are measured for the 5 reference and 6 gold black-coated devices. The devices are enclosed at 20 mTorr pressure and placed at 24 cm distance from the black body source, which is heated at 573 K. The signal from the black body source is chopped at 85 Hz frequencies.

70 nW incident power (P_i) on the individual pixel is evaluated using Plank's law of irradiance from the black body. The frequency bandwidth was 1 Hz (or integration time of 1 s) using operational amplifier.

Table 4 Measured output signal and noise of pixels with/without goldblack-SiO₂.

Performance Parameters	Without Gold Black-SiO₂ (0.6-40 μm) Measured	With Gold Black-SiO₂ (0.6-40 μm) Measured
Signal (μV)	38	54.1
Responsivity (V/W)	543	773
Noise (μV)	0.41	0.61

The output signal saw 42% improvement for the pixels with gold black coating. *This is the first ever proof that gold black-SiO₂ composite enhances the responsivity of the detector.* The output voltage is directly related to change in the local temperature (ΔT) of the bolometer membrane (VO_x-Au), which is related to absorptance on the membrane. There is also a marginal increase in the noise.

6.4 Calculations & Discussion

Heat capacity of the reference device is given by following formula;

$$C_{ref} = 2c_{SiO_2}\rho_{SiO_2}t_{SiO_2}A + c_{VO_x-Au}\rho_{VO_x-Au}t_{VO_x-Au}A \quad (6.11)$$

Here, C , ρ , t , A are material specific heat, density, thickness and area of the thin films respectively. Equation above represents the total heat capacity of the SiO₂/VO_x-Au/ SiO₂ stacks utilized for fabricating reference membrane. The heat capacity of the gold black devices are calculated by further adding 2 μm thick gold black layer (Bergman) and 200 nm of SiO₂ (Bruggeman) layer on top of reference device. The densities of respective layers are calculated using porosity values from Table 3.

$$C_{goldblack} = C_{ref} + c_{SiO_2} \rho_{SiO_2} t_{SiO_2} A + c_{goldblack} \rho_{goldblack} t_{goldblack} A \quad (6.12)$$

According to above equations, *thermal time constant for gold black device is 498 μs compared to 184 μs for reference device.* For gold black layer, value of *c* and *ρ* was chosen as 0.1291 (J/gK) and 1.5444 (g/cm³) respectively.

Figure 58 shows the calculated reflectance of the reference and gold black devices. The transfer matrix method [41] in SCOUT program is utilized for calculation of reflectance from multiple stacks arranged in the following order from top to bottom; SiO₂/ VO_x-Au /SiO₂/ 2.5 μm of cavity/ gold reflector. Each stack is defined by a set of refractive index (n) and extinction coefficient (k) for 2-14 μm wavelengths in the transfer matrix. (n,k) values for VO_x-Au membrane were measured using ellipsometry at US Air force Research Lab at Dayton. For reference device, 2.5-μm size cavity produces destructive interference close to vibrational modes of SiO₂. The coupling between inherent absorption of SiO₂ and destructive interference of the cavity results in merely ~ 11% reflectance at ~ 9.2 μm. However, the average reflectance in 8-14 μm is still very high at 73%. In 3-5 μm range the reference device is 87% of reflecting.

In order to include gold black-SiO₂ composite, transfer matrix is calculated for the following order of the stacks; Bruggeman medium of 200 nm of SiO₂ / Bergman medium of 1-2 μm of collapsed gold black/ SiO₂/ VO_x-Au active membrane/SiO₂/ 2.5 μm of cavity/ gold reflector.

Fitting parameters for collapsed gold black and SiO₂ are shown (In chapter 3).

Interestingly, when 2 μm of collapsed gold black is included on top layer, the reflectance

is correlated to calculated absorptance ($1-R-T$, where $T = 0$) in Figure 47 (bottom). The calculated average reflectance in 3-5 μm and 8-14 μm is 8% and 41%, respectively.

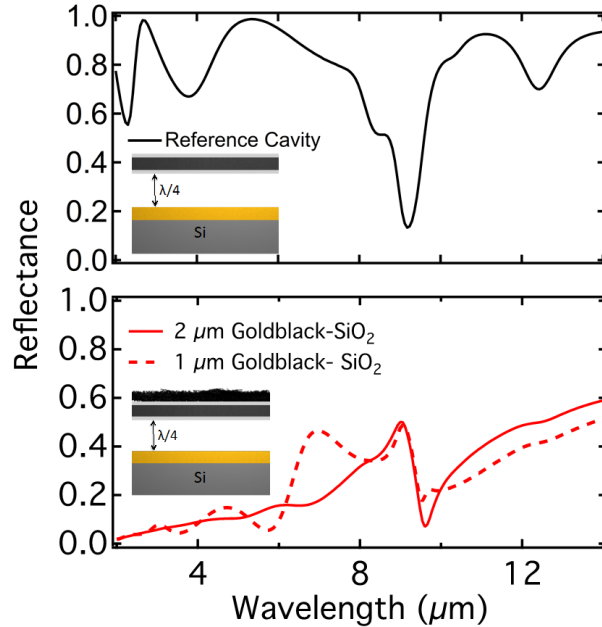


Figure 58 Calculated reflectance of the reference pixel (top) and gold black-SiO₂ coated pixel (bottom).

Transmission through the gold black-SiO₂ composite is null, which leaves cavity non-functional as far as the absorptance mechanism in gold black-coated devices is concerned. This is a fundamental difference between the reference and goldblack-SiO₂ coated devices. However, cavity is still extremely important for thermal isolation of the pixel from the substrate. Some degree of transmission through 1 μm thick collapsed gold black allows cavity to play a role in absorptance mechanism, which results in almost similar average reflectance as seen in Figure 58 (bottom). Due to lower heat capacity in thinner gold black-SiO₂ composite, lower thermal time constant can be achieved. Calculations using equation (6.2), (6.11) & (6.22) suggest, that much thinner 1- μm thick goldblack-SiO₂ composite can be utilized to reduce the thermal time constant of the gold black devices to 400 μs .

We also take the opportunity to utilize the spectral selectivity observed in simulated absorptance to comment on the increased noise in gold black-coated devices (Table 4). Both Johnson (6.4) and phonon noise (6.8) are independent of the absorptance mechanism. However, mean square power fluctuations (6.5), related to photon noise *do* depend on spectral selectivity and absorptance. Figure 59 clearly show higher noise equivalent power for gold black-coated devices. According to Eq (6.7) however, the total photon noise is still remains in \sim nV range, which is negligible compared to Johnson noise (\sim μ V).

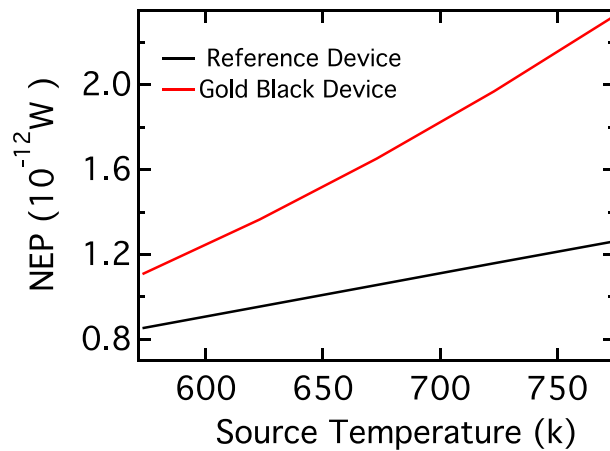


Figure 59 Noise equivalent power of reference and gold black-coated devices plotted against the source temperature. Mean square power fluctuations are calculated using equation

For calculations in Figure above, we treated reference devices as perfectly spectrally selective system in our calculation, $A \approx 27\%$ for $8 \mu\text{m} < \lambda < 14 \mu\text{m}$ and $A \approx 13\%$ for $5 \mu\text{m} > \lambda > 3 \mu\text{m}$ and λ . For gold black devices, $A \approx 74\%$ for $2 \mu\text{m} < \lambda < 14 \mu\text{m}$ and $A \approx 0\%$ for $\lambda > 14 \mu\text{m}$ and $\lambda < 2 \mu\text{m}$. However, in gold black devices, absorptance (A) may not have null value for $\lambda > 14 \mu\text{m}$ and $\lambda < 2 \mu\text{m}$. In fact it is known that gold black is absorbs shorter radiations much more efficiently, including visible wavelengths. Stray lights from the visible spectrum can also result in higher noise in gold black samples. These parameters are explained in ‘6.3 Initial Results’.

6.5 Future Work

Recently a lot research has been conducted in developing detectors, which can function in multiple bands [110-112]. These detectors generally utilize multiple arrays, with each one sensitive in a specific wavelength range. Broadband quantum detectors such as HgCdTe (Sofradir) and InAs/GaInSb (AIM) are already well developed with dual band capabilities, but they suffer from bulkiness and expensive cost due to cooling mechanism required. Dual/multi-spectral imaging in un-cooled detector is still difficult to achieve since the cavity result in sharp absorptance at a narrow range of wavelengths. Absorber layers such as SiN_x [14] and meta-materials [113] thin films also suffer from narrow range absorptance. Wide band absorptance can make *Gold black-SiO₂ coated device to produce integrated image from NIR-LWIR. Proper filter changing mechanism can also enable exclusive multi-spectral imaging in 3-5 μm and 8-14 μm band.* Table 5 shows the calculated output signal and noise of reference and gold black device. The calculations are based on similar parameters as utilized for actual experiments. These calculations clearly suggest, that gold black devices promise both high SNR and multi-spectral operation capability.

Table 5 Calculated output signal and noise in 3-5 μm and 8-14 μm wavelength range for reference and goldblack-SiO₂ coated devices. Absorptance for reference devices: 13% in 3-5 μm and 27% 8-14 μm. Absorptance for gold-black devices: 92% in 3-5 μm and 74 % in 8-14 μm.

Performance Parameters	Without Gold Black-SiO₂ (3-5 μm)	With Gold Black-SiO₂ (3-5 μm)	Without Gold Black-SiO₂ (8-14 μm)	With Gold Black-SiO₂ (8-14 μm)
Output Signal (μV)	3.8	26	9.3	20
Responsivity (V/W)	239	1.62×10^3	480	1.04×10^3
NEP (W)	3.8×10^{-10}	7.47×10^{-11}	2.5×10^{-10}	2.5×10^{-10}
SNR	42	216	77	166

More experiments need to be performed to increase the statistical pool to find out the source of additional noise in gold black devices. Future devices will also include much thinner gold black coatings for low thermal time constants. The detailed analysis are under consideration for publication.

APPENDIX A: PUBLICATIONS

Journal:

1. Deep Panjwani, Mehmet Yesiltas, Simranjit Singh, Enrique Del Barco, Robert E. Peale, Carol Hirschmugl, and Julia Sedlmair, "Stencil lithography of gold-black IR absorption coatings", *Infrared Physics & Technology*, 66:1-5 (2014).
2. Deep Panjwani, Mehmet Yesiltas, Janardan Nath, Doug E. Maukonen, Imen Rezadad, Evan M. Smith, Robert E. Peale, Carol J. Hirschmugl, Julia Sedlmair, Ralf Wehlitz, Miriam Unger, and Glenn Boreman, "Patterning of oxide-hardened gold black by photolithography and metal lift-off", *Infrared Physics & Technology*, 62:94-99, (2013).
3. Deep Panjwani, Aniruddha Dutta, Janardan Nath, Helge Heinrich, and Robert E. Peale, "Aging induced grain growth in nano-crystalline porous gold coatings" (Under Preparation)
4. Evan Smith, Deep Panjwani and Robert E Peale "Un-cooled VO_x-Au bolometer with gold black coating" (Under Preparation)

Conference:

1. Smith, Evan M., et al. "Linear bolometer array using a high TCR VO_x-Au film." SPIE Defense+ Security. International Society for Optics and Photonics, 2014.
2. Rezaie, Farnood K., et al. "Junction less thin-film ferroelectric oxides for photovoltaic energy production." SPIE Sensing Technology+ Applications. International Society for Optics and Photonics, 2014.
3. Nath, Janardan, et al. "Chalcogenide glass thin-film optics for infrared applications." SPIE Defense+ Security. International Society for Optics and Photonics, 2014.
4. Panjwani, Deep, et al. "Patterning and hardening of gold black infrared absorber by shadow mask deposition with ethyl cyanoacrylate." SPIE Defense, Security, and Sensing. International Society for Optics and Photonics, 2013.

APPENDIX B: COPYRIGHT PERMISSION LETTER

License Number	3613121043685
License date	Apr 20, 2015
Licensed content publisher	Nature Publishing Group
Licensed content publication	Nature Methods
Licensed content title	High-resolution Fourier-transform infrared chemical imaging with multiple synchrotron beams
Licensed content author	Michael J Nasse, Michael J Walsh, Eric C Mattson, Ruben Reininger, André Kajdacsy-Balla, Virgilia Macias
Licensed content date	Mar 20, 2011
Type of Use	reuse in a dissertation / thesis
Volume number	8
Issue number	5
Requestor type	academic/educational
Format	electronic
Portion	figures/tables/illustrations
Number of figures/tables/illustrations	1
High-res required	no
Figures	FTIR imaging with a multibeam synchrotron source. Reprinted with permission from Macmillan Publishers Ltd: Nature Communications [101].
Author of this NPG article	no
Your reference number	None
Title of your thesis / dissertation	CHARACTERIZATION OF GOLD BLACK AND ITS APPLICATION IN UN-COOLED INFRARED DETECTORS
Expected completion date	May 2015
Estimated size (number of pages)	140
Total	0.00 USD

Permission Letter for Figure 33

REFERENCES

1. Barr, E.S., *The Infrared Pioneers—II. Macedonio Melloni*. Infrared Physics, 1962. **2**(2): p. 67-74.
2. Barr, E.S., *The infrared pioneers—III. Samuel Pierpont Langley*. Infrared Physics, 1963. **3**(4): p. 195-206.
3. Biberman, L.M., *Electro-Optical Imaging: system performance and modeling*. Vol. 28. 2000: SPIE Press Bellingham, WA.
4. Rogalski, A., *History of infrared detectors*. Opto-Electronics Review, 2012. **20**(3): p. 279-308.
5. Kruse, P.W., et al., *Long wavelength photoeffects in mercury selenide, mercury telluride, and mercury telluride-cadmium telluride*. Infrared Physics, 1962. **2**(1): p. 53-60.
6. R.A. Wood, J.C., R.E. Higashi, T. Ohnstein, J. Holmen, *Advances in uncooled silicon monolithic IR 2D arrays*. Proc. IRIS DSG, 1988.
7. R.A. Wood, R.A.C., R.E. Higashi, N.A. Foss., *Progress in silicon monolithic uncooled IR focal plane arrays*. Proc. IRIS DSG, 1989.
8. R.A. Wood, B.E.C., N.A. Foss, C.J. Han, R.E. Higashi, R. Lubke., *Monolithic silicon uncooled focal plane development for high density array development program (HIDAD)*. 1990.
9. Kohin, M. and N.R. Butler. *Performance limits of uncooled VOx microbolometer focal plane arrays*. in *Defense and Security*. 2004. International Society for Optics and Photonics.
10. Murphy, D.F., et al. *Performance improvements for VOx microbolometer FPAs*. in *Defense and Security*. 2004. International Society for Optics and Photonics.
11. Mottin, E., et al. *Uncooled amorphous silicon technology enhancement for 25- μ m pixel pitch achievement*. in *International Symposium on Optical Science and Technology*. 2003. International Society for Optics and Photonics.
12. Bauer, S., et al., *Thin metal films as absorbers for infrared sensors*. Sensors and Actuators A: Physical, 1993. **37–38**(0): p. 497-501.
13. Lienhard, D., F. Heepmann, and B. Ploss, *Thin nickel films as absorbers in pyroelectric sensor arrays*. Microelectronic Engineering, 1995. **29**(1–4): p. 101-104.

14. Jutzi, F., et al., *Far-infrared sensor with LPCVD-deposited low-stress Si-rich nitride absorber membrane—Part 1. Optical absorptivity*. Sensors and Actuators A: Physical, 2009. **152**(2): p. 119-125.
15. Pfund, A.H., *BISMUTH BLACK AND ITS APPLICATIONS*. Review of Scientific Instruments, 1930. **1**(7): p. 397-399.
16. Pfund, A.H., *The Optical Properties of Metallic and Crystalline Powders*. Journal of the Optical Society of America, 1933. **23**(10): p. 375-377.
17. O'Neill, P., C. Doland, and A. Ignatiev, *Structural composition and optical properties of solar blacks: gold black*. Appl Opt, 1977. **16**(11): p. 2822-6.
18. Harris, L., R.T. McGinnies, and B.M. Siegel, *The Preparation and Optical Properties of Gold Blacks*. Journal of the Optical Society of America, 1948. **38**(7): p. 582-588.
19. Harris, L. and J.K. Beasley, *The Infrared Properties of Gold Smoke Deposits*. Journal of the Optical Society of America, 1952. **42**(2): p. 134-140.
20. Harris, L. and A.L. Loeb, *Conductance and Relaxation Time of Electrons in Gold Blacks from Transmission and Reflection Measurements in the Far Infrared*. Journal of the Optical Society of America, 1953. **43**(11): p. 1114-1118.
21. Harris, L., *The Transmittance and Reflectance of Gold Black Deposits in the 15- to 100-Micron Region*. Journal of the Optical Society of America, 1961. **51**(1): p. 80-82.
22. Becker, W., et al., *Black gold deposits as absorbers for far infrared radiation*. physica status solidi (b), 1996. **194**(1): p. 241-255.
23. Becker, W., R. Fettig, and W. Ruppel, *Optical and electrical properties of black gold layers in the far infrared*. Infrared Physics & Technology, 1999. **40**(6): p. 431-445.
24. Advena, D.J., V.T. Bly, and J.T. Cox, *Deposition and characterization of far-infrared absorbing gold black films*. Applied Optics, 1993. **32**(7): p. 1136-1144.
25. Niklaus, F., C. Vieider, and H. Jakobsen. *MEMS-based uncooled infrared bolometer arrays: a review*. 2007.
26. Ashcroft, N.W.M., N. D., *Solid State Physics*, ed. Brooks/Cole. 1976, New York.
27. Liz-Marzán, L.M., *Nanometals: Formation and color*. Materials Today, 2004. **7**(2): p. 26-31.

28. Kuwata, H., et al., *Resonant light scattering from metal nanoparticles: Practical analysis beyond Rayleigh approximation*. Applied Physics Letters, 2003. **83**(22): p. 4625-4627.
29. Catchpole, K.R. and A. Polman, *Plasmonic solar cells*. Optics Express, 2008. **16**(26): p. 21793-21800.
30. Atwater, H.A. and A. Polman, *Plasmonics for improved photovoltaic devices*. Nat Mater, 2010. **9**(10): p. 865-865.
31. Zhang, L., et al., *Wrinkled Nanoporous Gold Films with Ultrahigh Surface-Enhanced Raman Scattering Enhancement*. ACS Nano, 2011. **5**(6): p. 4407-4413.
32. Scholl, J.A., A.L. Koh, and J.A. Dionne, *Quantum plasmon resonances of individual metallic nanoparticles*. Nature, 2012. **483**(7390): p. 421-427.
33. Garnett, J.C.M., *Colours in Metal Glasses and in Metallic Films*. Philosophical Transactions of the Royal Society of London. Series A, Containing Papers of a Mathematical or Physical Character, 1904. **203**(359-371): p. 385-420.
34. Bruggeman, D.A.G., *Berechnung verschiedener physikalischer Konstanten von heterogenen Substanzen. II. Dielektrizitätskonstanten und Leitfähigkeiten von Vielkristallen der nichtregulären Systeme*. Annalen der Physik, 1936. **417**(7): p. 645-672.
35. Lifshitz, L.D.L.a.E.M., *Electrodynamics of Continuous Media*. Vol. 8. 1960: Pergamon Press Ltd. 45-47.
36. Looyenga, H., *Dielectric constants of heterogeneous mixtures*. Physica, 1965. **31**(3): p. 401-406.
37. Bergman, D.J., *The dielectric constant of a composite material—A problem in classical physics*. Physics Reports, 1978. **43**(9): p. 377-407.
38. Griffiths, D.J., *Introduction to Electrodynamics*, ed. K.D. Alison Reeves. 1999, Upper Saddle river, New Jersey 07458: Prentice-Hall, Inc.
39. Zeng, X., et al., *Effective-medium theory for weakly nonlinear composites*. Physical Review B, 1988. **38**(15): p. 10970.
40. Sancho-Parramon, J., et al. *Effective medium models for metal-dielectric composites: an analysis based on the spectral density theory*. in *Optical Systems Design 2005*. 2005. International Society for Optics and Photonics.
41. Born, M. and E. Wolf, *Principles of optics, 1975*. Imprint, Oxford Pergamon Press, New York.

42. Heinrich, H., *High-Resolution Transmission Electron Microscopy for Nanocharacterization*, in *Functional Nanostructures*, S. Seal, Editor. 2008, Springer New York. p. 414-503.
43. Yu, Q., et al., *Control and characterization of individual grains and grain boundaries in graphene grown by chemical vapour deposition*. *Nature materials*, 2011. **10**(6): p. 443-449.
44. Schroder, D.K. *Semiconductor Material and Device Characterization*. 1998: John Wiley & Sons, New York.
45. Panjwani, D., *Joule heating of gold black*. 2014: <https://www.youtube.com/watch?v=djrXPoULO4U&feature=youtu.be>.
46. Shekhar, S., et al., *Correlated breakdown of carbon nanotubes in an ultra-high density aligned array*. arXiv preprint arXiv:1101.4040, 2011.
47. Harris, L., D. Jeffries, and B.M. Siegel, *An Electron Microscope Study of Gold Smoke Deposits*. *Journal of Applied Physics*, 1948. **19**(8): p. 791-794.
48. Hopkins, P.E., et al., *Thermal Conductivity in Nanoporous Gold Films during Electron-Phonon Nonequilibrium*. *Journal of Nanomaterials*, 2008. **2008**.
49. Wang, J., et al., *Effect of thermal coarsening on the thermal conductivity of nanoporous gold*. *Journal of Materials Science*, 2012. **47**(12): p. 5013-5018.
50. Rosnagel, S.M. and T.S. Kuan, *Alteration of Cu conductivity in the size effect regime*. *Journal of Vacuum Science & Technology B*, 2004. **22**(1): p. 240-247.
51. Wu, W., et al., *Influence of surface and grain-boundary scattering on the resistivity of copper in reduced dimensions*. *Applied Physics Letters*, 2004. **84**(15): p. 2838-2840.
52. Sun, T., et al., *Dominant role of grain boundary scattering in the resistivity of nanometric Cu films*. *Physical Review B*, 2009. **79**(4): p. 041402.
53. Jongenburger, P., *The extra-resistivity due to vacancies in copper, silver and gold*. *Applied Scientific Research, Section B*, 1954. **3**(1): p. 237-248.
54. Korevaar, B.M., *The influence of lattice defects on the electrical resistivity of a gold-copper alloy (7 at. % Cu)*. *Acta Metallurgica*, 1958. **6**(9): p. 572-579.
55. Theiß, W., S. Henkel, and M. Arntzen, *Connecting microscopic and macroscopic properties of porous media: choosing appropriate effective medium concepts*. *Thin Solid Films*, 1995. **255**(1): p. 177-180.

56. Theiß, W., *Optical properties of porous silicon*. Surface Science Reports, 1997. **29**(3): p. 91-192.
57. Eickhoff, T., et al., *Determination of the effective dielectric function of silver powders produced by inert gas evaporation*. Zeitschrift für Physik B Condensed Matter, 1992. **88**(1): p. 17-23.
58. Theiß, W., *The use of effective medium theories in optical spectroscopy*, in *Advances in Solid State Physics 33*. 1993, Springer. p. 149-176.
59. Zhang, D., E. Cherkayev, and M.P. Lamoureux, *Stieltjes representation of the 3D Bruggeman effective medium and Padé approximation*. Applied Mathematics and Computation, 2011. **217**(17): p. 7092-7107.
60. Spanier, J.E. and I.P. Herman, *Use of hybrid phenomenological and statistical effective-medium theories of dielectric functions to model the infrared reflectance of porous SiC films*. Physical Review B, 2000. **61**(15): p. 10437.
61. Eickhoff, T., P. Grosse, and W. Theiss, *Diffuse reflectance spectroscopy of powders*. Vibrational spectroscopy, 1990. **1**(2): p. 229-233.
62. Evenschor, M., P. Grosse, and W. Theiss, *Optics of two-phase composites*. Vibrational spectroscopy, 1990. **1**(2): p. 173-177.
63. Sturm, J., P. Grosse, and W. Theiss, *Effective dielectric functions of alkali halide composites and their spectral representation*. Zeitschrift für Physik B Condensed Matter, 1991. **83**(3): p. 361-365.
64. T.Eickhoff, P.G., S.Henkel, W.Theiss, *Determination of the effective dielectric function of silver powders produced by inert gas evaporation* Z.Phys.B. - Condensed Matter, 1992(88): p. 17-23.
65. Sturm, J., et al., *Far infrared optical properties of metal-insulator composites*. Zeitschrift für Physik D Atoms, Molecules and Clusters, 1993. **26**(1): p. 195-197.
66. Gorges, E., et al., *A parameterization of the effective dielectric function of a two-phase composite medium*. Zeitschrift für Physik B Condensed Matter, 1994. **94**(3): p. 223-226.
67. Sturm, J., *Doctoral Thesis*. 1993, RWTH Aachen (Germany).
68. Nelms, N., et al. *Focal plane array for the GERB instrument*. 2004.
69. Ristau, R., et al., *Electron microscopy studies of the thermal stability of gold nanoparticle arrays*. Gold Bulletin, 2009. **42**(2): p. 133-143.

70. C. J. Clukay, C.N.G., D. J. Freppon, A. Bhattacharya, S.M. Kuebler, H.Heinrch, *Nanoscale characterization of gold nanoparticles created by in situ reduction at a polymeric surface*. Journal of Microscopy, 2013. **251**(1): p. 27-34.
71. Dutta, A., et al., *Nanoscale characterization of gold nanoparticles created by in situ reduction at a polymeric surface*. Journal of Microscopy, 2013. **251**(1): p. 27-34.
72. Dutta, A. and H. Heinrich, *Interfacial Atomic Number Contrast in Thick Samples*. Microscopy and Microanalysis, 2014. **20**(SupplementS3): p. 136-137.
73. Liu, H.B., et al., *Melting behavior of nanometer sized gold isomers*. Surface Science, 2001. **491**(1-2): p. 88-98.
74. Yacamán, M.J., et al., *Structure shape and stability of nanometric sized particles*. Journal of Vacuum Science & Technology B, 2001. **19**(4): p. 1091-1103.
75. Wakuda, D., K.-S. Kim, and K. Suganuma, *Room temperature sintering of Ag nanoparticles by drying solvent*. Scripta Materialia, 2008. **59**(6): p. 649-652.
76. Magdassi, S., et al., *Triggering the Sintering of Silver Nanoparticles at Room Temperature*. ACS Nano, 2010. **4**(4): p. 1943-1948.
77. Thompson, C.V. and H.I. Smith, *Surface-energy-driven secondary grain growth in ultrathin (100 nm) films of silicon*. Applied Physics Letters, 1984. **44**(6): p. 603-605.
78. Atkinson, H., *Overview no. 65: theories of normal grain growth in pure single phase systems*. Acta Metallurgica, 1988. **36**(3): p. 469-491.
79. Ederth, J., et al., *In situ electrical transport during isothermal annealing of nanocrystalline gold films*. Journal of applied physics, 2002. **91**(3): p. 1529-1535.
80. Chen, Z., C. Shek, and J. Lai, *An analysis of the grain growth kinetics in Mn₂O₃ nanocrystals*. Applied Physics A, 2005. **80**(4): p. 703-707.
81. Burke, J., *Some factors affecting the rate of grain growth in metals*. AIME TRANS, 1949. **180**: p. 73-91.
82. Mazurin, O.V., *Relaxation phenomena in glass*. Journal of Non-Crystalline Solids, 1977. **25**(1): p. 129-160.
83. Ederth, J., et al., *In situ electrical transport during isothermal annealing of nanocrystalline gold films*. Journal of Applied Physics, 2002. **91**(3): p. 1529-1535.

84. Lim, T.H., et al., *Real-Time TEM and Kinetic Monte Carlo Studies of the Coalescence of Decahedral Gold Nanoparticles*. ACS Nano, 2009. **3**(11): p. 3809-3813.
85. Ingham, B., et al., *How Nanoparticles Coalesce: An in Situ Study of Au Nanoparticle Aggregation and Grain Growth*. Chemistry of Materials, 2011. **23**(14): p. 3312-3317.
86. Yuk, J.M., et al., *In situ atomic imaging of coalescence of Au nanoparticles on graphene: rotation and grain boundary migration*. Chemical Communications, 2013. **49**(98): p. 11479-11481.
87. Schell, N., et al., *The nanostructure evolution during and after magnetron deposition of Au films*. Thin Solid Films, 2003. **441**(1–2): p. 96-103.
88. Cleary, J.W., et al., *Effects of Polymer Infusion and Characteristic Length Scale on Gold-Black Long-Wave and Far-Infrared Absorbance*. Journal of Materials Science and Engineering, 2011. **5**(2): p. 171-176.
89. Panjwani, D., et al. *Patterning and hardening of gold black infrared absorber by shadow mask deposition with ethyl cyanoacrylate*. in *SPIE Defense, Security, and Sensing*. 2013. International Society for Optics and Photonics.
90. Janardan Nath, D.M., Evan Smith, Pedro Figueiredo, Guy Zummo, Deep Panjwani, Robert E. Peale, Glenn Boreman, Justin W Cleary, Kurt Eyink, *Thin-film, wide-angle, design-tunable, selective absorber from near UV to far infrared*. SPIE, 2013: p. 87041.
91. Wang, B., et al., *Vanadium oxide microbolometer with gold black absorbing layer*. Optical Engineering, 2012. **51**(7): p. 074003-1-074003-6.
92. John Lehman, E.T., George Eppeldauer and Chris Pannell, *Gold-black coatings for freestanding pyroelectric detectors*. Measurement Science and Technology, 2003. **14**(7): p. 916.
93. Hirota, M., et al., *120° × 90° element thermoelectric infrared focal plane array with precisely patterned Au-black absorber*. Sensors and Actuators A: Physical, 2007. **135**(1): p. 146-151.
94. Li, B., *Design and simulation of an uncooled double-cantilever microbolometer with the potential for ~mK NETD*. Sensors and Actuators A: Physical, 2004. **112**(2–3): p. 351-359.
95. Savu, V., et al., *Dynamic stencil lithography on full wafer scale*. Journal of Vacuum Science & Technology B, 2008. **26**(6): p. 2054-2058.
96. Nao Takano, L.M.D., Marc A F van den Boogaart, Janko Auerswald, Helmut F Knapp, Olivier Dubochet, Thomas Hessler and Jürgen Brugger, *Fabrication of*

- metallic patterns by microstencil lithography on polymer surfaces suitable as microelectrodes in integrated microfluidic systems.* Journal of Micromechanics and Microengineering, 2006. **16**(8).
97. Vazquez-Mena, O., et al., *Metallic Nanowires by Full Wafer Stencil Lithography.* Nano Letters, 2008. **8**(11): p. 3675-3682.
 98. Aksu, S., et al., *High-Throughput Nanofabrication of Infrared Plasmonic Nanoantenna Arrays for Vibrational Nanospectroscopy.* Nano Letters, 2010. **10**(7): p. 2511-2518.
 99. Carr, G.L., *Resolution limits for infrared microspectroscopy explored with synchrotron radiation.* Review of Scientific Instruments, 2001. **72**(3): p. 1613-1619.
 100. Yesiltas, M., *Synchrotron based infrared microscopy of carbonaceous chondrites, in Physics Department.* 2014, University of Central Florida: Orlando USA.
 101. Nasse, M.J., et al., *High-resolution Fourier-transform infrared chemical imaging with multiple synchrotron beams.* Nat Meth, 2011. **8**(5): p. 413-416.
 102. Nasse, M.J., et al., *Opportunities for multiple-beam synchrotron-based mid-infrared imaging at IRENI.* Vibrational Spectroscopy, 2012. **60**(0): p. 10-15.
 103. Nelms, N., et al., *Laser micromachining of goldblack coatings.* Applied Optics, 2006. **45**(27): p. 6977-6981.
 104. Fang, M., D. Hu, and J. Shao, *Evolution of stress in evaporated silicon dioxide thin films.* Chinese Optics Letters, 2010. **8**(1): p. 119-122.
 105. Akimov, Y.A., et al., *Nanoparticle-enhanced thin film solar cells: Metallic or dielectric nanoparticles?* Applied Physics Letters, 2010. **96**(7): p. -.
 106. Smith, E.M., et al. *Linear bolometer array using a high TCR VOx-Au film.* in *SPIE Defense+ Security.* 2014. International Society for Optics and Photonics.
 107. Smith, E.M., et al. *Linear bolometer array using a high TCR VOx-Au film.* 2014.
 108. Fox, M., *Quantum Optics: An Introduction: An Introduction.* Vol. 6. 2006: Oxford University Press.
 109. Chen, C., et al., *Micromachined uncooled IR bolometer linear array using VO2 thin films.* International Journal of Infrared and Millimeter Waves, 2001. **22**(1): p. 53-58.
 110. Rogalski, A. *New material systems for third generation infrared detectors.* in *Correlation Optics 2009.* 2009. International Society for Optics and Photonics.

111. Gunapala, S.D., et al., *Demonstration of megapixel dual-band QWIP focal plane array*. Quantum Electronics, IEEE Journal of, 2010. **46**(2): p. 285-293.
112. Rehm, R., et al. *Type-II superlattices: the Fraunhofer perspective*. in *SPIE Defense, Security, and Sensing*. 2010. International Society for Optics and Photonics.
113. Nath, J., et al., *Optical Salisbury screen with design-tunable resonant absorption bands*. Journal of Applied Physics, 2014. **115**(19): p. -.